MAGNETIC HARDENING

IN THE TRANSITION METAL NANOPARTICLES AND NANOWIRES

by

MEIYING XING

Presented to the Faculty of the Graduate School of

The University of Texas at Arlington in Partial Fulfillment

of the Requirements

for the Degree of

DOCTOR OF PHILOSOPHY

THE UNIVERSITY OF TEXAS AT ARLINGTON

August 2020

ACKNOWLEDGEMENTS

I would like to express my deepest gratitude to my advisor Dr. J. Ping Liu for providing invaluable guidance for my research and for constantly supporting me over the past four years. I especially want to thank him for introducing me to scientific research and providing me with challenges. His expertise in nanostructured magnetism, along with his vision of nanotechnology, has been a source of inspiration for me to pursue further research in this exciting field. The present research could not have been completed without his expert guidance, constant supervision, and ongoing encouragement. I would also like to thank Prof. Ali R. Koymen, Prof. Joseph Ngai, Prof. Alex Weiss and Prof. Qiming Zhang for serving on my dissertation supervisory committee. I am grateful to them for their support of my research and for their careful and critical proof reading of my dissertation. I appreciate creative discussions with my past and present colleagues Dr. Jeotikanta Mohapatra, Julian Beatty, Jacob Elkins, Dr. Kinjal Gandha, Dr. Fanhao Zeng. I want specifically to give my deepest thanks to Dr. Jeotikanta Mohapatra who gave me plenty of instructions, inspiration, and help in the experiment design, data analysis, and academic writing. I would also like to thank our collaborator, Dr. Sanjay Mishra from the University of Memphis for their help in providing support from their Mössbauer spectroscopy facility. I am thankful to Dr. Jiechao Jiang from the Characterization Center for Materials and Biology at UTA for the technical support and the help with operating TEM and SEM. I appreciate Dr. Weixing Xia for their help in electron holography measurements.

Most of all, I want to thank my husband Charles Crawford III and my parents, who more than anyone have provided inspiration and love. This work is dedicated to them.

July 31, 2020

ABSTRACT

MAGNETIC HARDENING
IN THE TRANSITION METAL NANOPARTICLES AND NANOWIRES

Meiying Xing, Ph.D.
The University of Texas at Arlington

Supervising Professor: J. Ping Liu

Permanent magnets are important materials widely used in advanced technologies including electric vehicles, windmills, memory devices, magnetic levitation transportation, and biomedical apparatus. Rare-earth-based compounds with excellent magnetic performance are dominant in the permanent magnet market. However, researchers have also worked on rare-earth-free permanent magnets ascribed to the rare-earth crisis. For fundamental and application points of view, in this thesis, we investigated magnetic hardening in 3*d* transition metal nanostructures by controlling the morphology and composition. Nanoscale Co particles with single hcp crystalline structure were synthesized. As a result, the optimum coercivity of 2.7 kOe is obtained in the Co nanoparticles, owing to the size effect and the coherent rotation mechanism in magnetization reversal. The magnetic hardening is achieved in nickel carbide and iron carbide by introducing carbon atoms into the interstitial positions and the size control of the nanoparticles. To take advantage of magnetocrystalline anisotropy and shape anisotropy to enhance the coercivity, Co nanowires (NWs) with varied diameter and aspect ratio, and iron carbide nanorods were successfully synthesized. The record high coercivity of 13.0 kOe and energy product of 60 MGOe were achieved in the Co NWs attributed to the geometrical effect. The magnetization reversal mode is

investigated by measuring the angular dependence of coercivity and comparing with the analytical results of the Stoner-Wohlfarth model.

To produce bulk nanostructured magnets for application purpose, we fabricated Co NW assemblies by compressing the nanowires together. Energy product of 20 MGOe of the assemblies has been achieved. The proximity effect on the magnetic hardening of consolidated Co NW assemblies was studied.

In addition, surface oxidized Co nanoparticles and nanowires have provided us a unique opportunity to study microstructural effects on the exchange bias in the Co/CoO core-shell nanostructures. Study of temperature dependence of the exchange bias field, the coercive field and the training effect in the Co/CoO core-shell nanostructures reveals the importance of the interplay of the different magnetic anisotropy at the interface. Moreover, the exchange bias induced by the Verwey transition is observed in Fe_5C_2/Fe_3O_4 core-shell systems. The corresponding exchange anisotropy results in a prominent enhancement of H_C at low temperatures.

Table of Contents

List of Figures

List of Tables

Chapter 1 Fundamentals of Nanostructured Magnetic Materials

1.1 Basic Concepts of Magnetism

1.1.1 Origin of Magnetic Moments

Macroscopic magnetism is a collective reflection of the atomic magnetic moments. Atomic magnetic moments are mainly determined by electron magnetic moments including orbital magnetic moment $\vec{\mu}_l$ and spin moment $\vec{\mu}_s$ shown in Figure 1.1.[1]

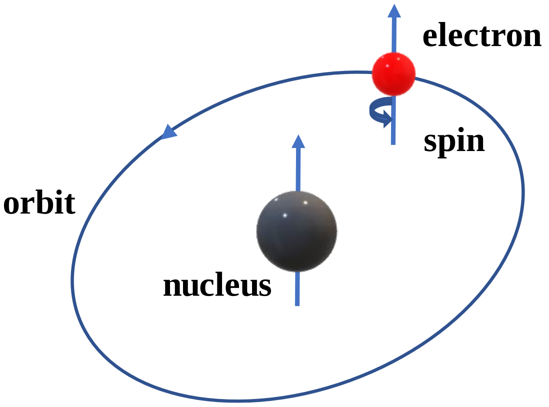

Figure 1.1 The orbit of a spinning electron about the nucleus of an atom.

$$|\vec{\mu}_l| = -\frac{e}{2m_e}|\vec{L}| = \sqrt{l(l+1)}\frac{e\hbar}{2m_e} = \sqrt{l(l+1)}\mu_B \qquad 1.1$$

$$|\vec{\mu}_l^z| = |m_l|\mu_B \qquad 1.2$$

where $\vec{L}$ is orbital angular momentum, $\mu_B = \frac{e\hbar}{2m_e}$ Bohr magneton, l the orbital angular momentum quantum number and m_l the integer value comprised between $-l$ and l.

$$\left|\vec{\mu}_s\right| = -\frac{e}{m_e}\left|\vec{S}\right| = \sqrt{s(s+1)}\,\frac{e\hbar}{m_e} = 2\sqrt{s(s+1)}\,\mu_B \qquad 1.3$$

$$\left|\vec{\mu}_s^z\right| = \left|m_s\right| 2\mu_B = \mu_B \qquad 1.4$$

where $s = 1/2$ is the spin quantum number, $m_s = 1/2$ for spin up and $m_s = -1/2$ for spin down.

1.1.2 Types of Magnetism

Magnetization is a respond of a substance to an applied magnetic field $\vec{H}$. The induced magnetic moment $\vec{M}$ (magnetic moment per unit volume) in the substance is related to $\vec{H}$ by the relationship

$$\vec{M} = \chi\vec{H} \qquad 1.5$$

where χ is the volumetric magnetic susceptibility of substance and a constant.

For **diamagnetic materials**, χ is negative. Diamagnetism exists in all substances. The characteristic of a diamagnetic material is that all the electrons are paired. As a result, the moment induced by the interaction of paired electrons with the magnetic field is opposite to that of the applied magnetic field shown in Figure 1.2. Superconductors, copper, water, and wood are typical examples of diamagnetic materials.

For **paramagnetic materials**, χ is positive ($10^{-5} < \chi < 10^{-3}$) shown in Figure 1.2, which linearly increases with $\frac{1}{T}$. The characteristic of a paramagnetic material is the existence of the unpaired electrons which is free to align its magnetic moment in any direction. Although the material has unpaired electrons, due to the random orientation of the magnetic moment, the net magnetization is zero. However, if there is an applied magnetic field, these spins will align them to the field direction.

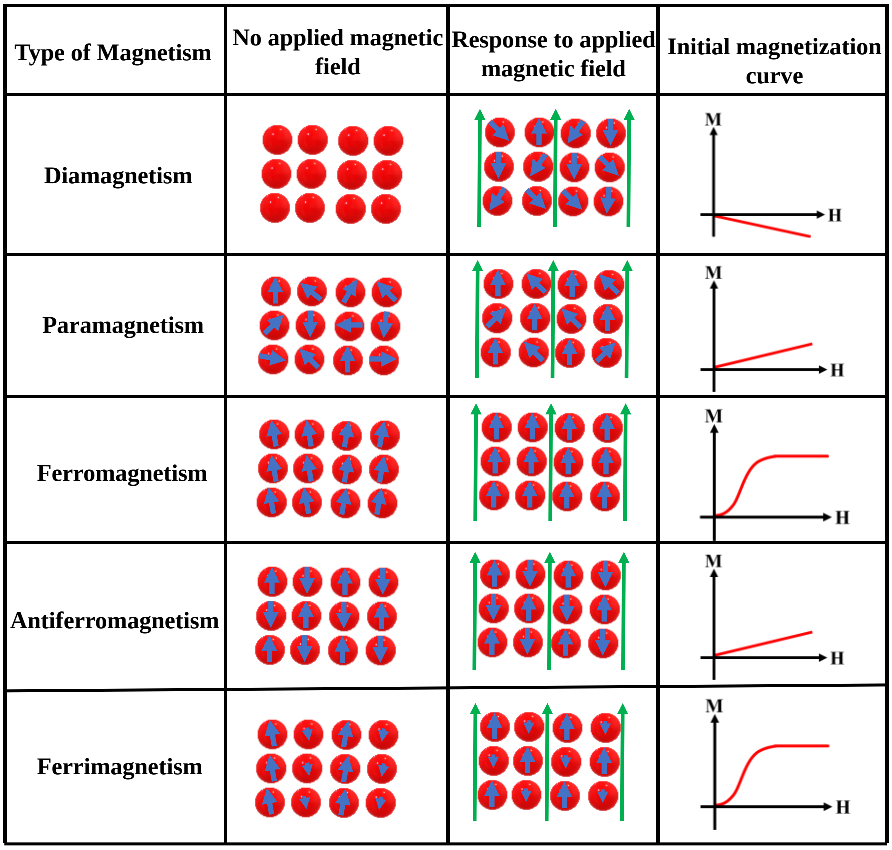

Figure 1.2 Different types of magnetism in materials. Green Arrows indicate the direction of the applied field. Blue arrows in the red circles signify the direction of the electron spin.

The characteristic of a ferromagnetic material is governed by magnetic ordering: spin-spin coupling (exchange coupling). The quantum mechanical origin of exchange coupling is derived from the electrostatic coupling between electron orbits, which necessarily satisfies the Pauli Exclusion Principle. The spin–spin coupling can be expressed in terms of Heisenberg Hamiltonian as[2]

$$H_{ex} = -\sum_{i<j}^{N} J_{ij} S_i \cdot S_j \qquad 1.6$$

where S_i and S_j are atomic spins at different neighboring sites. J_{ij} is the exchange coefficient, which is strongly related to the overlapping of the two atomic orbitals.

In **ferromagnetic materials**, J is positive and spins favor parallel ($\uparrow\uparrow$) alignment of atomic moments as shown in Figure 1.2. When the thermal energy ($\sim k_B T$) overcomes the exchange energy ($\sim JS^2$), the ferromagnetic spin ordering disappears, and the corresponding temperature is known as the Curie temperature (T_C).

Some materials are with more than one magnetic sublattice such as **antiferromagnetic materials** and **ferrimagnetic materials**. In the **antiferromagnetic material**, it has two equal but oppositely directed sublattices leading to zero net magnetization as shown in Figure 1.2. Due to the thermal agitation breaking the exchange interaction, each sublattice magnetization disappears above the Néel point (T_N) and thus the material becomes paramagnetic. Two unequal and oppositely directed magnetic lattices constitute a **ferrimagnet** (see Figure 1.2).

1.1.2 Soft and Hard Magnetic Materials

Ferromagnetic materials show a “history dependent” nature of magnetization: a hysteresis loop shown in Figure 1.3a. Hysteresis loop is paramount to understand and characterize the intrinsic and extrinsic magnetic properties of ferromagnetic materials such as saturation magnetization ($\boldsymbol{M_S}$), remanence ($\boldsymbol{M_R}$) and coercivity ($\boldsymbol{H_C}$) shown in the loop. $\boldsymbol{M_S}$ is the maximum magnetization value which will not increase with the improved applied $\boldsymbol{H}$. $\boldsymbol{M_R}$ is the magnetization value when the applied magnetic field decreases to 0. $\boldsymbol{H_C}$ is the coercivity field where the $\boldsymbol{M}$ changes the sign.

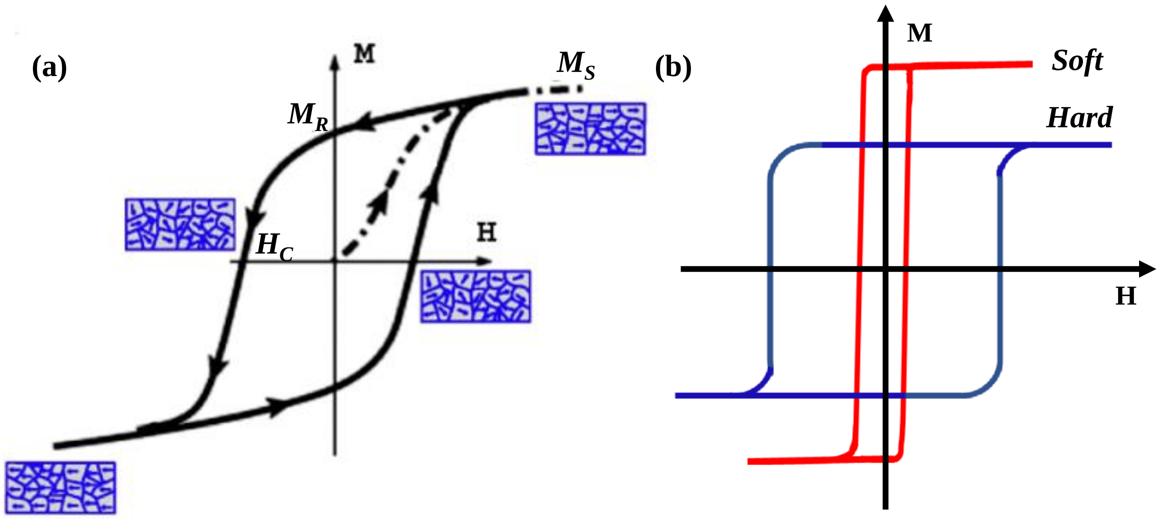

Figure 1.3 (a) A hysteresis loop of a ferromagnetic material. (b) Typical *M-H* curves for the soft and hard magnetic materials.

Two categories of widely used ferromagnets are distinguished by their hysteresis loops. Soft ferromagnets have high $\boldsymbol{M_S}$ with low coercivity as shown in Figure 1.3b. Bcc iron is a good example of soft magnetic materials. Hard magnetic materials have broad square loops with $H_C > \frac{1}{2} M_S$ (see Figure 1.3b). Hard magnetic materials produce high magnetic flux combining with high stability against demagnetization. A typical example is $SmCo_5$. The figure of merit hard magnetic quality is determined by the maximum energy product $(BH)_{max}$, which is represented by the area of the largest rectangle in the second quadrant of B-H loop, as depicted in Figure 1.4.

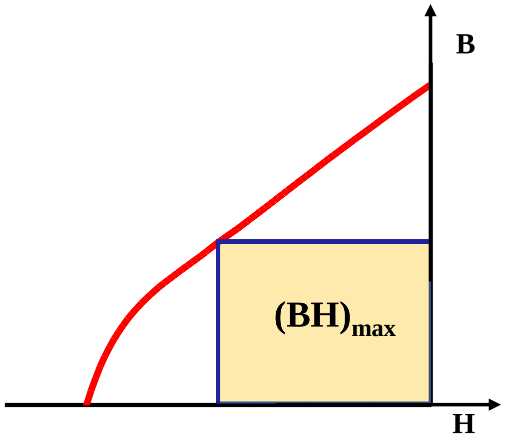

Figure 1.4 The 2nd quadrant of hysteresis loop, where the red line is B-H curve and square box is the (BH)$_{max}$.

1.2 Magnetic Anisotropy and Coercivity Mechanisms

1.2.1 Magnetic Anisotropy

The exchange interaction between atomic spins in equation 1.6 is purely isotropic. However, the isotropic symmetry is always broken because the electron orbitals interact with the potential energy of the hosting crystal lattice. As a result, the spins are orientated along some preferred crystallographic axes and the associated energy is known as magnetocrystalline anisotropy energy. The favorable spin orientated direction is called easy axis. Magnetic anisotropy is directional dependent on the magnetic properties. The magnetic anisotropy mainly arises from different sources: magnetocrystalline anisotropy, shape anisotropy, surface anisotropy and exchange anisotropy.[3] Here, we only focus on two sources of magnetic anisotropy: magetocrystalline anisotropy (MCA) and shape anisotropy.

1.2.1.1 Magnetocrystalline Anisotropy

The origin of magnetocrystalline anisotropy is that the spin of electron interacts with the crystal structure via spin-orbit coupling. Electron moments have different energies in different crystallographic directions. The magnetization process is different when the applied field along the different crystallographic directions. Magnetocrystalline anisotropy is an intrinsic property. The magnetization curves of single crystals of the three 3*d* ferromagnetic elements show a different approach to saturation when magnetized in different directions shown in Figure 1.5.

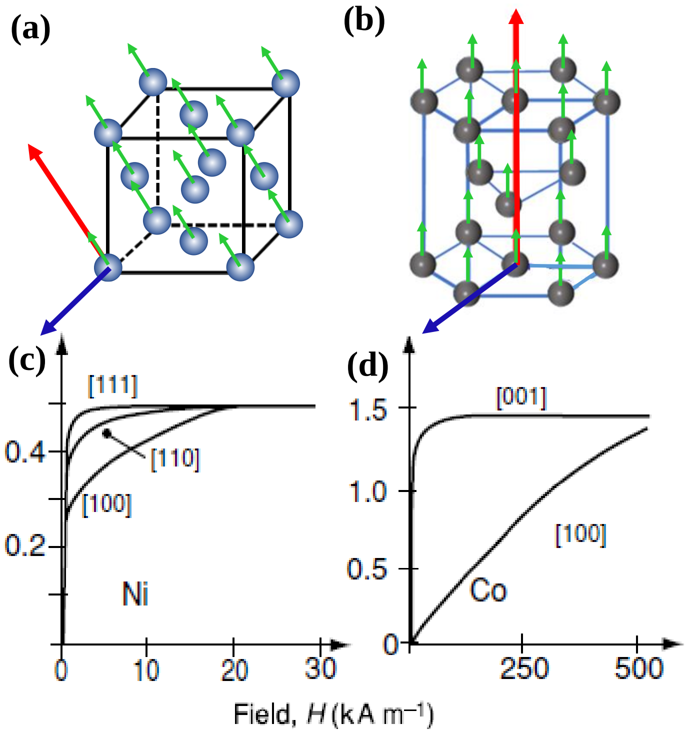

Figure 1.5 (a) and (b) Magnetization of single crystal fcc-Ni and hcp-Co. Red, blue and green arrows represent the easy axis of magnetization, hard axis of magnetization and direction of net atomic spin, respectively. (c) and (d) Magnetization of single crystals of fcc-Ni and hcp-Co.[4]

For cubic crystal, the anisotropy energy is expressed as

$$E_{MC} = K_0 + K_1(\alpha_1^2\alpha_2^2 + \alpha_2^2\alpha_3^2 + \alpha_3^2\alpha_1^2) + K_2\alpha_1^2\alpha_2^2\alpha_3^2 + \ldots \qquad 1.7$$

where K_0, K_1 and K_2 are anisotropy constants, α_1, α_2 and α_3 cosine values responding to the angles between the magnetization direction and the three crystal axes, $\alpha_1 = \sin\theta\cos\varphi, \alpha_2 = \sin\theta\sin\varphi, \alpha_3 = \cos\theta$. K_0 is independent of angle and can be ignored.

For a hexagonal close-packed crystal, the related magnetocrystalline anisotropy is expressed as

$$E_{MC} = K_0 + K_1 \sin^2\theta + K_2 \sin^4\theta \tag{1.8}$$

where, θ is the angle between $\vec{M}$ and $z-axis$. If $K_1 > 0$, the energy is the lowest when $\theta = 0$. The $c-axis$ is the easy axis. If $K_1 < 0$, the easy axis is on the base plane.

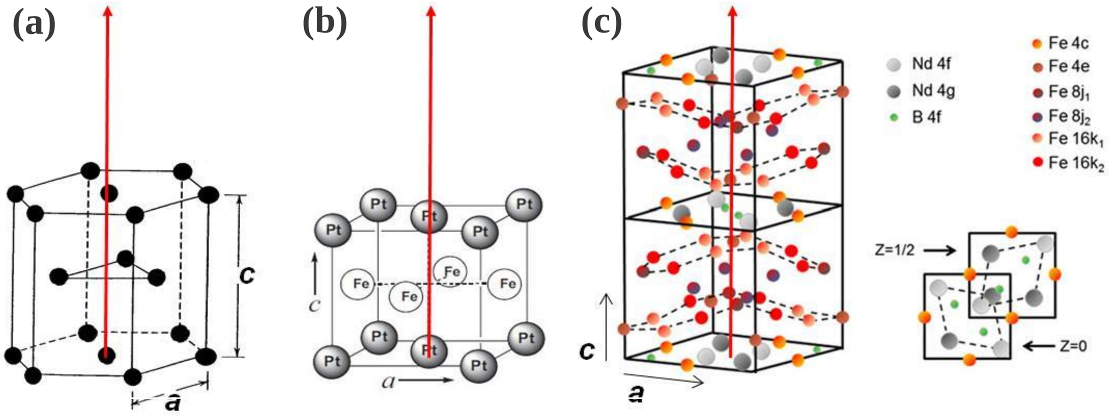

hcp Co **$L1_0$ FePt** **Tetragonal $Nd_2Fe_{14}B$**

Figure 1.6 Atomic cell of (a) hcp-cobalt, (b) tetragonal (*$L1_0$*) FePt and (c) tetragonal $Nd_2Fe_{14}B$. The red arrows denote the magnetization easy axis along the crystallographic c-axis.[5, 6]

The magnitude of the magnetocrystalline anisotropy is based on the symmetry of crystal lattice. The lower symmetry, the higher possibility of possessing magnetocrystalline anisotropy. Thus, the crystal structure with low symmetry such as the hexagonal (hcp-Co, $SmCo_5$), orthorhombic

($HfCo_7$, Co_3C, Co_2C), tetragonal ($Nd_2Fe_{14}B$, MnAl, *L1*$_0$ FePt) or rhombohedral (Zr_2Co_{11}) crystal lattices have a single magnetization easy axis and generally along the c-axis which is shown in Figure 1.6. $SmCo_5$ displays an extraordinarily high MCA of K_1 = 17.0 MJ/m^3.[7] In addition to the lattice symmetry, the strength of the spin-orbit coupling is the other important factor to develop high magnetocrystalline anisotropy. Based on this fact, Co and rare-earth elements such as Nd and Sm are introduced to generate the strong spin-orbit coupling. $Nd_2Fe_{14}B$ exhibits a very high magnetocrystalline anisotropy with K_1 = 4.9×10^6 MJ/m^3.[7]

If only the magnetocrystalline anisotropy is considered, the anisotropy field (H_a) for the uniaxial crystal is calculated in the following way.[3]

$$E = E_{MC} + E_Z = [K_1 \sin^2\theta - \mu_0 M_S H \cos(\frac{\pi}{2} - \theta)]V \qquad 1.9$$

where the last term is the Zeeman energy which corresponds to the interaction of the externally applied field H and the magnetization M_S. Minimizing E, $\frac{\partial E}{\partial \theta} = 0$ and setting $\theta = \frac{\pi}{2}$,

$$\frac{\partial E}{\partial \theta} = [2K_1 \sin\theta \cos\theta - \mu_0 M_S H \cos\theta]V = 0 \qquad 1.10$$

$$H_a = \frac{2K_1}{\mu_0 M_S} \qquad 1.11$$

1.2.1.2 Shape Anisotropy

If the shape of a sample is not spherical, the demagnetizing field in different direction is varied leading the various demagnetized field energy.[8] N_x, N_y and N_z are the corresponding demagnetization factors in the x, y and z direction.

$$H_{di} = -N_{di} M_{Si} \quad i = x, y, z \qquad 1.12$$

$$E_d = -\frac{\mu_0}{2} M_S H_d = \frac{\mu_0 M_S^2}{2} (N_x \alpha_1^2 + N_y \alpha_2^2 + N_z \alpha_3^2) \qquad 1.13$$

For a long wire in z direction, $N_x = N_y = \frac{1}{2}, N_z = 0$,

$$E_d = \frac{\mu_0 M_S^2}{2} (N_x \alpha_1^2 + N_y \alpha_2^2) = \frac{\mu_0 M_S^2}{4} (1 - \alpha_3^2) = \frac{\mu_0 M_S^2}{4} \sin^2 \theta \qquad 1.14$$

where θ is the angle between $\vec{M}$ and $z - axis$. The demagnetizing energy E_d is dependent on θ. For the long wire, E_d is smallest when θ equals zero, meaning in the long axis. As a result, it is easy to get magnetized in the long wire direction.

$$K_{SH} = \frac{\mu_0 M_S^2}{4} \qquad 1.15$$

K_{SH} is shape anisotropy constant. For a thin film, $N_x = N_y = 0, N_z = 1$ in $x - y$ plane,

$$E_d = \frac{\mu_0 M_S^2}{2} \alpha_3^2 = \frac{\mu_0 M_S^2}{2} \cos^2 \theta \qquad 1.16$$

$$K_{SH} = \frac{\mu_0 M_S^2}{2} \qquad 1.17$$

When θ equals 0, meaning perpendicular to $x - y$ plane, E_d is the highest. $\theta = \frac{\pi}{2}$ means in $x - y$ plane, E_d is the smallest.

If the shape anisotropy is included in the effective anisotropy, the anisotropy field H_a for the uniaxial crystal is calculated in 1.2.2.3 Coercivity Mechanisms in Nanoparticles.

1.2.2 Coercivity Mechanisms

The core properties of hard magnetic materials, namely the large residual magnetic polarization and the noticeable coercivity, are the manifestation of the quantum properties of electrons in the macroscopic scale. They result from the strong coupling between nanoscale structural features and magnetic structures such as magnetic domain walls inside the magnetic material. Magnetic domains, domain walls and exchange length play significant roles in coercivity.

1.2.2.1 Magnetic Domains and Domain Walls

Due to the exchange coupling and spin-orbit coupling, the atom spins should order spontaneously parallel to each other in ferromagnets. However, the parallel alignment of spins over a large volume enhances the magnetostatic energy.[3]

$$E_M = \frac{1}{2}\mu_0 N_d M_S^2 \qquad 1.18$$

Hence, to minimize the magnetostatic energy, the large volume breaks into numbers of non-aligned small volumes known as domains and is separated by domain walls (see Figure 1.7).

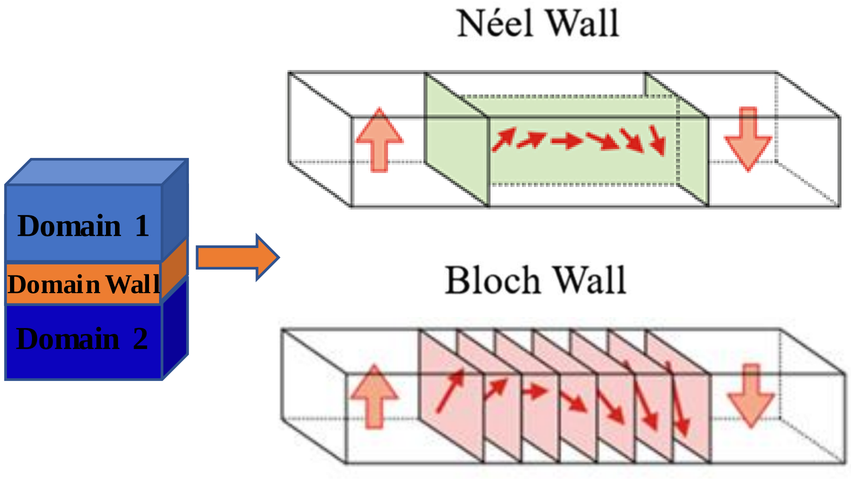

Figure 1.7 Two types of domain wall: Néel wall and Bloch wall.[9, 10] Magnetic domain wall containing atomic magnetic moments of gradually varying orientation, ensuring a smoother transition to the opposite domain magnetization.

The interface to separate the adjacent domains is **domain wall** (δ),[11] which accounts for the competition between the exchange energy and the magnetocrystalline anisotropy. Depending on the ratio of the thickness of a sample and the thickness of the domain wall, the energy associated with the free poles that arise where domain wall meets the surface will be different. This results in a change in wall structure. If the spins rotate in the plane of the sample, it is **Néel wall** (Figure 1.7). If the spins rotate in the different planes, it is **Bloch wall** (Figure 1.7).

$$\delta = \pi\sqrt{\frac{A}{K}} \qquad 1.19$$

$$A = \frac{N_V S^2 a^2 J}{2} \qquad 1.20$$

where A and K_1 are exchange stiffness constant and magnetocrystalline anisotropy constant, respectively.[12] N_V, S, a and J are the number of nearest neighbor atoms per unit volume, the magnetic moment of the atom, the distance between spins and the exchange interaction, respectively. It is paramount to obtain the information of the structure, wall width and energy of domain wall, which play significant roles in magnetization process. There is another magnetic characteristic parameter: **exchange length**[12]

$$l_{ex} = \sqrt{\frac{A}{\mu_0 M_S^2}} \qquad 1.21$$

The exchange length is the minimal length-scale over which the direction of the magnetic moments can change. It defines the threshold below which atomic exchange interaction prevails in the magneto-static fields. The exchange length is typically on the order of a few nanometers shown in Table 1.1. To make these mesoscopic length scales more clearly, they are summarized in Figure 1.8.

Table 1.1 Values of the exchange length and wall width parameters for several common hard and soft magnetic materials.[12]

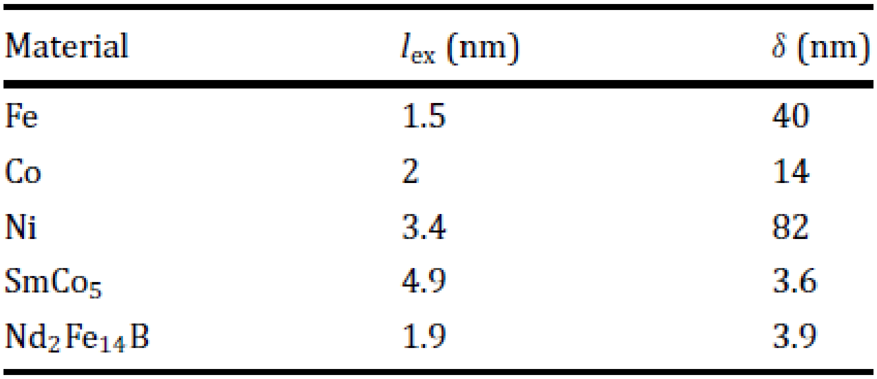

Material	l_{ex} (nm)	δ (nm)
Fe	1.5	40
Co	2	14
Ni	3.4	82
$SmCo_5$	4.9	3.6
$Nd_2Fe_{14}B$	1.9	3.9

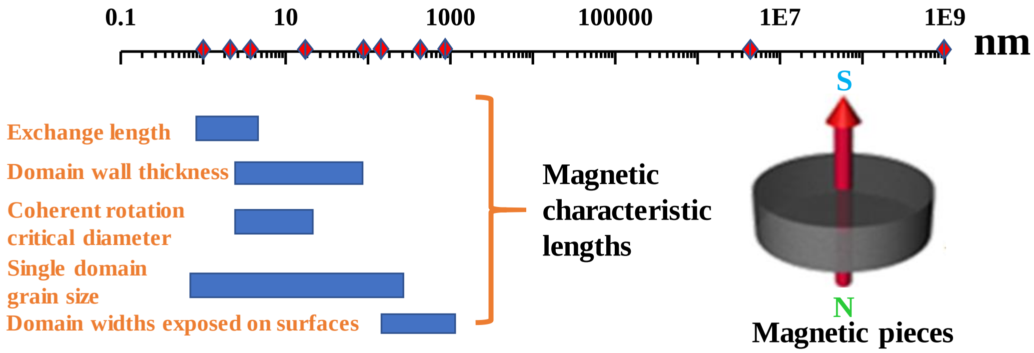

Figure 1.8 Magnetic characteristic length scales.

1.2.2.2 Nucleation and Domain Wall Pinning

The anisotropy field represents the upper limit for the coercive field H_C of the magnetically highly anisotropic materials. However, the H_C values, obtained in reality, are much smaller than H_a. The $\frac{H_C}{H_a}$ ratio is between 0.05 and 0.15. This is called Brown's paradox. For ensemble of multidomain particles, real crystals are never perfect, and their magnetic reversal occurs via two possible mechanisms. (a) **Nucleation**: Domains of reversed magnetization are difficult to nucleate, whereas the domain walls can easily move; (b) **domain wall pinning**: there are many nuclei with reversed magnetization in the crystal, but the movement of the domain walls is hindered at defects or pinning centers such as nonmagnetic precipitates and grain boundaries. In the first case the coercive field is determined by the field necessary to create a nucleus, and in the second case by the field necessary to break the domain walls loose from the pinning sites. The virgin magnetization curves are illustrated in Figure 1.9. In these two cases, H_C can be expressed in the following equation.[3]

$$H_C = \alpha H_A - N_{eff} M_S \qquad 1.22$$

where, α is the microstructural parameter. N_{eff} is the demagnetizing constant.

Permanent magnets with coercivity governed by domain nucleation can be produced only by grinding the material to fine particles with diameters of single domain size. $SmCo_5$ and Sm-Fe-N are typical hard magnetic materials in which the nucleation dominates the magnetization reversal process. For the domain wall pinning, a higher field is required to fully magnetize the material in pinning-type magnets such as Cu-substituted SmCo-series magnet and PrCu-diffusion $Nd_2Fe_{14}B$ magnet.

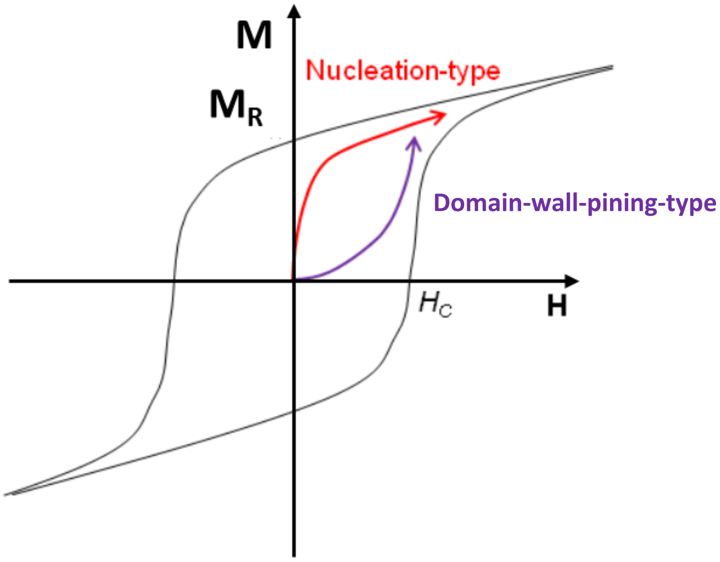

Figure 1.9 Schematic of initial magnetization curves for nucleation-type and domain-wall-type magnets.[13]

1.2.2.3 Coercivity Mechanisms in Nanoparticles

Magnetic properties of ferromagnetic nanoparticles, such as *coercivity* and *saturation magnetization*, are robustly varied with the particles size.[14] Moreover, the magnetic properties are mainly governed by three key features: (i) single domain size (D_S); (ii) coherent rotation size (D_{coh}) and (iii) superparamagnetism size (D_{SPM}).

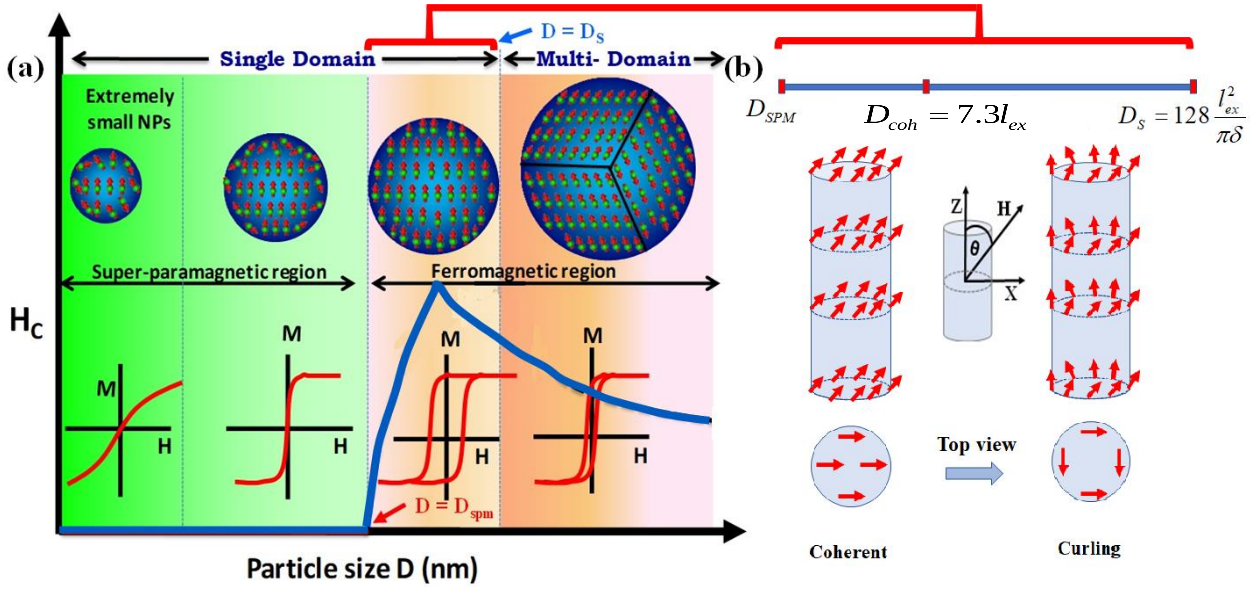

Figure 1.10 (a) Size-dependent magnetic domain structures from superparamagnetism to single domain and multidomain ferromagnetism. (b) Magnetization reversal modes in nanowires. (The red arrows represent the orientation of magnetic moments within the nanowires.)

D_S : a critical size of the particle remains with single domain and cannot be broken into domains. When the size of the particles reduces to D_S , the formation of domain walls is energetically less preferable as the energy cost of domain formation is bigger than the benefits of decreasing the magnetostatic energy. Thus, the particles remain in a single-domain structure. The size limit of D_S , D_{coh} and D_{SPM} can be estimated from the equation: [9, 12]

$$D_S = \frac{9\left(JK_1\right)^{1/2}}{\mu_0 M_S^2} = 128\frac{l_{ex}^2}{\pi\delta} \qquad 1.23$$

where μ_0 is the permeability of free space ($4\pi \times 10^{-7}$ H/m) and J is the exchange coefficient.

$$D_{coh} = 2\sqrt{24}l_{ex} \tag{1.24}$$

$$D_{SPM} = \left(\lambda \frac{27k_B T}{K_{eff}} \right)^n \tag{1.25}$$

where n = 1/2 for wires and n = 1/3 for spheres. The geometric factor λ is 4/πL (L, the length of nanowires) and 6/π for wires and spheres, respectively.

Magnetization reversal proceeds via spin rotation in single-domain particles, instead of the movement of domain walls. As a result, single-domain particles yield a larger coercive force compared to a multi-domain system since it is harder to rotate the spin than to move a domain wall. The typical H_C dependence on the particle size is schematically represented in Figure 1.11a. Above the single domain size, nucleation and pinning mechanism are common that lead to the relatively low coercivity. While below the coherent rotation size ($d < D_{coh}$), the magnetization direction of the particle gets increasingly fluctuated by the thermal energy as the anisotropy energy become similar to the thermal energy. Thus, the H_C value decreases as the diameter of the magnetic particle deviates from D_{coh}. A maximum H_C nearly two orders of magnitude larger than that of the bulk materials may be obtained in single-domain magnets with the diameter near to D_{coh}. In addition, the H_C value becomes zero when $d < D_{SPM}$. The detailed magnetization reversal mechanism in nanoparticle with $D_{SPM} < d < D_S$ will be discussed later.

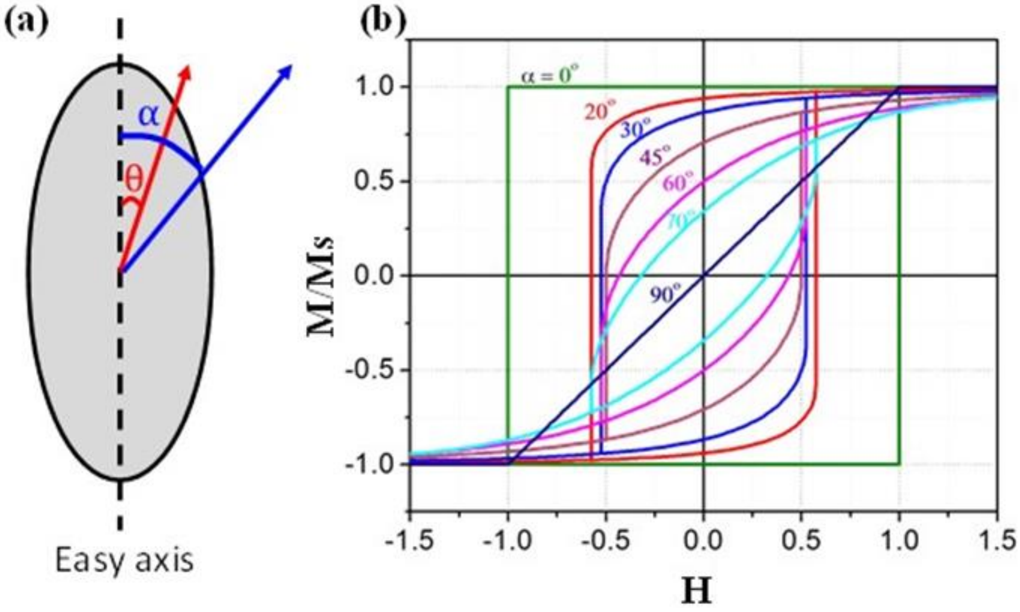

Figure 1.11 (a) Illustration of the variables used in the Stoner–Wohlfarth model. (b) Hysteresis loops for single domain particles with uniaxial anisotropy. α is the angle between the field and the easy axis.

The H_C of nanowires or nanorods with single domain size is also strongly related to the magnetization reversal. To depict the magnetization reversal of magnetic nanoparticles, the spins in the nanoparticle remain homogeneous within the particle during the reversal process: coherent rotation (see in Figure 1.11b). The energy density is given by the Stoner–Wohlfarth model[15]

$$E = E_{MC} + E_S + E_Z = \left[\left(K_1 + K_d \right) \sin^2 \theta - \mu_0 MH \cos\left(\alpha - \theta \right) \right] V \qquad 1.26$$

where α is the angle between the applied magnetic field and the easy axis of the particle and θ is the angle between the magnetization and the easy axis of the particle (Figure 1.11a).

The anisotropy field can be calculated using equation 1.26 via minimizing E, $\frac{\partial E}{\partial \theta} = 0$ and setting $\theta = \frac{\pi}{2}$,

$$\frac{\partial E}{\partial \theta} = ((2K_1 + K_{SH})\sin\theta\cos\theta - \mu_0 M_S H\cos\theta)V = 0 \qquad 1.27$$

$$H_a = \frac{2(K_1 + K_{SH})}{\mu_0 M_S} = \frac{2K_1}{\mu_0 M_S} + \frac{M_S}{2} = H_k + H_d \qquad 1.28$$

Equation 1.26, nevertheless, gives a qualitative description of the reversal of elongated nanoparticles. The hysteresis cycle as a function of the angle α between H and the easy axis can be calculated. Figure 1.11b shows that the value of the coercive field is strongly affected by the angle α. Note that when the particles are aligned along the magnetic field H the coercive field is the sum of two contributions, one from the magnetocrystalline anisotropy field H_k and the other one from the shape anisotropy field H_d. When the external magnetic field is applied perpendicular to the long axis (α = 90◦), the coercive field is zero, and the saturation field is $H_C = \frac{M_S}{2}$. Especially for intermediate situations, the coercivity drops very quickly. This is the typical case of coherent reversal of magnetization, which can yield a maximum nucleation field value. Thus, if one wants to exploit the shape anisotropy to produce materials with high coercivity, it is necessary to have a very good alignment of the wires or nanorods following the coherent reversal model.

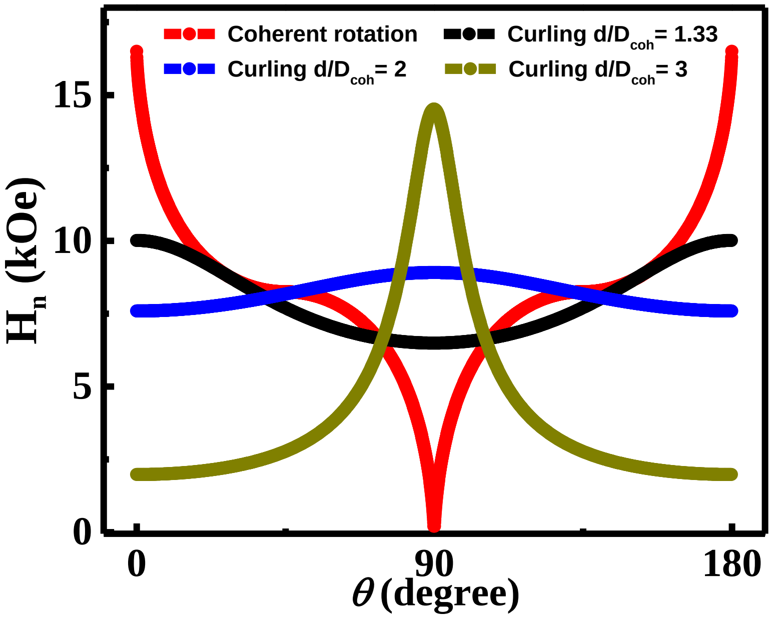

Figure 1.12 The angular dependence of the nucleation field H_n calculated via the coherent rotation model for an infinitely long cylinder is shown (red curve). Calculated angular dependence of H_n based on the curling model: dependence on reduced diameter $S = 1.33$(black curve), $S = 2$(blue curve) and $S = 3$(green curve), respectively.

In single-domain particles, the reversal process is not necessarily uniform and cannot be always coherent rotation mode. The other non-uniform magnetization reversal modes-curling leads to lower coercive fields than that in the Stoner-Wohlfarth model. In this mode, the angle between the individual magnetic moments and the cylinder axis varies from one spin to another. They are observed in structures exhibiting a radius larger than the coherence diameter D_{coh}.

In the case of a cylinder, the value of D_{coh} is $7.3 l_{ex}$. When the nanowires are with the diameter $\sim D_{coh}$ the magnetization reversal proceeds via coherent rotation (see in Figure 1.11b).

The angular dependence of the reduced coercivity according to the Stoner-Wohlfarth model for a coherent magnetization reversal for the infinite long nanowires can be established as[16]

$$H_n^C(\theta) = -\frac{2[K_1 + K_{SH}]\sqrt{1-t^2+t^4}}{M_S(1+t^2)} \qquad 1.29$$

where $t = \tan(\theta)^{1/3}$ with θ being the angle between the applied field and the long axis of the nanowire. K_1 and K_{SH} are shape anisotropy and magnetocrystalline anisotropy, respectively. In Co NWs case, $K_1 = 5.2\times10^6$ erg/cm^3 and $K_{SH} = 6.1\times10^6$ erg/cm^3, respectively. According to the Stoner-Wohlfarth model, the obtained nucleation field curve based on coherent rotation is shown in Figure 1.12 (red curve).[17]

$$H_n^C(\theta) = \begin{cases} \left|H_n^C(\theta)\right|, & 0 \le \theta \le \pi/4 \\ 2\left|H_n^C(\pi/4) - H_n^C(\theta)\right|, & \pi/4 \le \theta \le \pi/2 \end{cases} \qquad 1.30$$

For even bigger radii, between the coherent rotation diameter and the single-domain limit, the magnetization proceeds via Curling-mode rotation.

The reduced coercivity can be calculated as[16]

$$H_n^V(\theta) = \frac{M_S(2N_z - \frac{k}{S^2})(2N_x - \frac{k}{S^2})}{\sqrt{(2N_z - \frac{k}{S^2})^2 \sin\theta^2 + (2N_x - \frac{k}{S^2})^2 \cos\theta^2}} \qquad 1.31$$

where S is the reduced diameter $\frac{R}{R_C}$; $k = \frac{q}{\pi^2}$, where $q = 1.84$ for an infinite cylinder. The obtained nucleation field curve based on curling mode is shown in Figure 1.12.

1.3 Nanostructured Hard Magnetic Materials

Alnico permanent magnet has demonstrated the successful development of coercivity from shape anisotropy of elongated Fe–Co precipitates, which is driven by the microstructure evolution.[18] Moreover, recent nano-structuring technology leads the low dimensional structure control. As a result, the morphology of the nanoparticles has also been tuned to develop high coercivity via utilizing shape anisotropy (see Figure 1.13). Single crystal and single domain hcp-Co nanowires display recorded coercivity of 12.4 kOe and energy product of 44 MGOe, respectively.[19] An array of single-crystalline α-Fe nanowires with diameter of 20 nm and coercivity of 3.4 kOe is obtained via pulsed laser deposition.[20] The alternative approach to improve the magnetic anisotropy is to develop the exchange anisotropy by introducing the exchange coupling interaction in the interfacial layer of bi-magnetic core/shell nanoparticles shown in Figure 1.13.[21-23] In addition, the size effect, which is mentioned in 1.2.2.3 Coercivity Mechanisms in Nanoparticles, also plays important role in coercivity. As a result, low-dimensional magnetic systems like nanodots (0D), nanowires (1D) and nanoflakes (2D) have attracted plenty of attention from various fields due to their remarkable size and shape dependent magnetic properties.

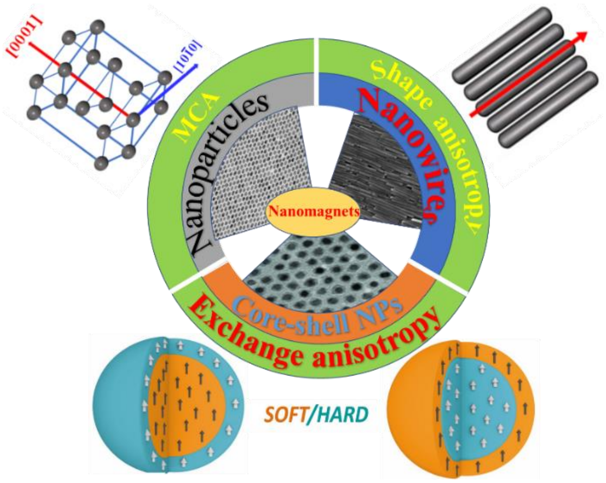

Figure 1.13 The schematic representation of the different types of nanomagnets with the enhanced effective magnetic anisotropy.

1.3.1 Nanoparticle-based Hard Magnetic Materials

As discussed before, the crystal structures such as hexagonal, orthorhombic, tetragonal or rhombohedral crystal lattices are genetic to develop high magnetocrystalline anisotropy yielding prominent coercivity. $SmCo_5$ and $Nd_2Fe_{14}B$ not only possess the low symmetry crystal lattice structure but also have Nd and Sm elements to develop the high spin-orbit coupling resulting in the prominent magnetic anisotropy. Matsushita et al. firstly prepared $SmCo_5$ nanoparticles in sizes of single nanometers by a chemical route using a polyol process.[24] However, due to the oxidation and the existence of byproducts coercivity value is very low (1.5 kOe). Later, CaO and Ca are introduced into the annealing and reduction process to do the reduction and prevent the oxidation. As a result, the coercivity of 72 kOe is obtained in the homogeneous $SmCo_5$ NPs with the average diameter of 400 nm.[25] $Nd_2Fe_{14}B$ nanoparticles are successfully synthesized by mechanochemically method.[26, 27] Chaudhary et al. obtained $Nd_2Fe_{14}B$ nanoparticles with average diameter of 18 nm displaying coercivity of 14.4 kOe. In Sm-Fe nitrides and Co carbide, Nitrogen and carbon enter the lattice interstitially, expanding the volume of the unit cell and leading to a drastic increase in the Curie temperature and dramatic changes in the magnetic anisotropy.[28-31] Although $Sm_2Fe_{17}N_3$ is easy to get oxidized, the advanced nano-structure engineering technology makes it possible to develop $Sm_2Fe_{17}N_3$ nanomagnets.[28, 29] The highest coercivity of 24.7 kOe is achieved in $Sm_2Fe_{17}N_3$ NCs with mean diameter of 500 nm.[29] Harris *et al.* demonstrated H_C of 3.4 kOe and $(BH)_{max}$ of 2.6 MGOe in Co-carbide nanoparticles.[32] In addition to rare-earth metal alloys, Sm-Fe nitrides and Co carbide, the compounds such as FePt, with the reduced symmetry of the tetragonal chemically ordered $L1_0$ hard phases have also been intensively explored in recent years.[33-41] The theoretical

$(BH)_{max}$ and H_C for the distorted tetragonal FeCo with interstitial boron are 100 MGOe and 9.3 kOe, respectively.[42] Despite a high magnetocrystalline anisotropy field, the experimental coercivity of distorted tetragonal FeCo alloys is low(< 1 kOe).[39, 43, 44] This is attributed to the imperfect crystal structure and the non-uniformity of the order parameter inside the nanocrystals resulting from the fabrication processes. $L1_0$ FePt nanoparticles (8 nm) with giant coercivity of 33 kOe are obtained via the salt-matrix annealing approach.[45] Due to the non-cubic crystal structures, Co-rich intermetallic compounds $Co_{100-x}TM_x$ (TM = Hf, Zr and $10 \leq x \leq 18$) such as $HfCo_7$, Zr_2Co_{11} have been explored intensively.[46-53] The uniaxial assemblies of $HfCo_7$ nanoparticles exhibit the H_C = 4.4 kOe, K_1 ~1.0 MJ/m^3, and magnetic polarization J_S =1.08 T at room temperature.[46] The uniaxially aligned Zr_2Co_{11} nanoparticle assemblies exhibit a high remanence ratio M_R/M_S and a high coercivity H_C (4.1 kOe).[54] Fine size control of Cobalt ferrite NCs within the single domain size leads $CoFe_2O_4$ NCs with the prominent coercivity value of 9.4 kOe.[55, 56]

1.3.2 Exchange-coupled Nanocomposite Magnets

To develop the permanent magnet with high energy product, researchers want to take advantage of high coercivity in hard magnetic materials and high magnetization in soft magnetic materials via the formation of exchange coupling at the interface. An exchange-spring magnet was proposed in 1991.[5] The proposed magnet would behave like a single-phase magnet with a giant energy product. The schematic in Figure 1.14 depicts magnetic behavior of such a magnet with exchange-coupled hard and soft layers. In this figure, the applied field is opposite to the magnetization of the hard phase, but lower in magnitude than the switching field of the hard phase. The moments closer to the hard layer are more strongly coupled, and thus the soft magnetization resembles a torsional spring upon demagnetization. The exchange-spring concept requires the soft phase to be sufficiently small such that domain walls do not form upon reversal. The soft phase dimensions should be about twice the width of the hard phase domain walls (i.e., ≈ 2 to 4 nm).[57] The smaller the hard phase, the larger the volume fraction of soft-phase can be accommodated, and thus can results larger M_S and $(BH)_{max}$. The implications of the exchange-spring magnet are that a hard, rare-earth-free magnet could be coupled with a soft, high M_S magnet in order to form rare-earth-free permanent magnets that would have competitive $(BH)_{max}$ compared to Nd-Dy-Fe-B magnets. In the exchange coupled nanocomposites, the magnetic moments of soft and hard phase rotate coherently, giving rise to a smooth hysteresis loop with no shoulder or kink (red curve). Compared to the counterpart of soft and hard magnets, the coupled material has relatively high M_S and H_C, resulting in a high energy product.

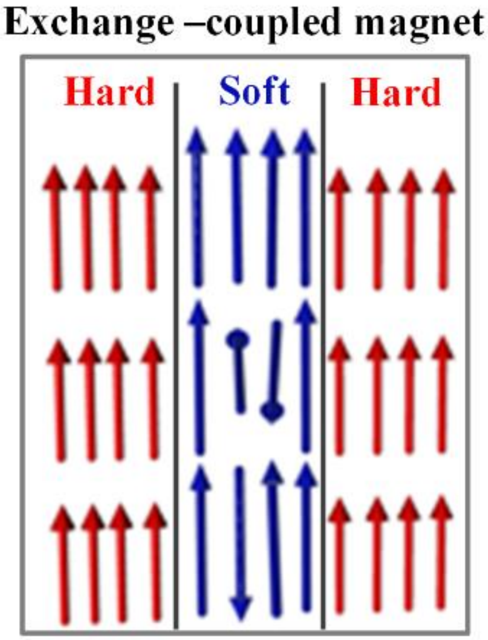

Figure 1.14 A model of an exchange-coupled magnet shows the hard/soft interfaces and the "spring" that forms within the soft magnetization.

1.3.3 AlNiCo Permanent Magnets

Alnico magnets composed of Fe, Co, Ni, and Al with much higher coercivity than the best steel magnets of the time were discovered by T. Mishima in early 1930s.[58] The high H_C in Alnico magnets is developed from the shape anisotropy of the ferromagnetic Fe-Co precipitates (α_1 phase) finely dispersed in a non-magnetic Ni-Al matrix (α_2 phase). This typical Fe-Co/Ni-Al dispersion is caused by spinodal decomposition of the α phase into the α_1 and α_2 phases during the heat treatment. The spinodal decomposition is a spontaneous diffusion process and occurs only at relatively high temperatures ~850°C.[11, 18, 59-61] The concentrations of the Fe and Co atoms in the two phases vary periodically and the magnitude of the composition fluctuations increases gradually until the phase separation is complete. A schematic representation of the Alnico phase diagram is shown in Figure 1.15a. The early Alnico magnets (Alnicos grade 1, 2, 3 and 4) were comprised of randomly oriented FeCo parallelepipeds. The random distribution of magnetization easy axis exhibited low coercivity 0.58 - 1.31 kOe.[62, 63] By applying a magnetic field during the annealing stage, an elongated anisotropic microstructure of FeCo can be obtained. This process results in the development of aligned elongated FeCo precipitates that possess a <001> texture (Figure 1.15b) and H_C as high as 2.04 kOe.[59,64, 65] In contrast to the isotropic grade, the anisotropic Alnico magnets exhibited higher coercivity and energy product. The textured Alnico magnets are referred by their energy product and graded as Alnico 5-9. The progress of Alnico magnets development since their discovery is summarized in Figure 1.15c and d. The timeline of Alnico development reveals that the magnetic properties of Alnico magnets is very sensitive to the addition of Co and Cu. The addition of these elements leads to refinement of the nanostructures and composition, and thus enhances the magnetic performance of the Alnico alloys.

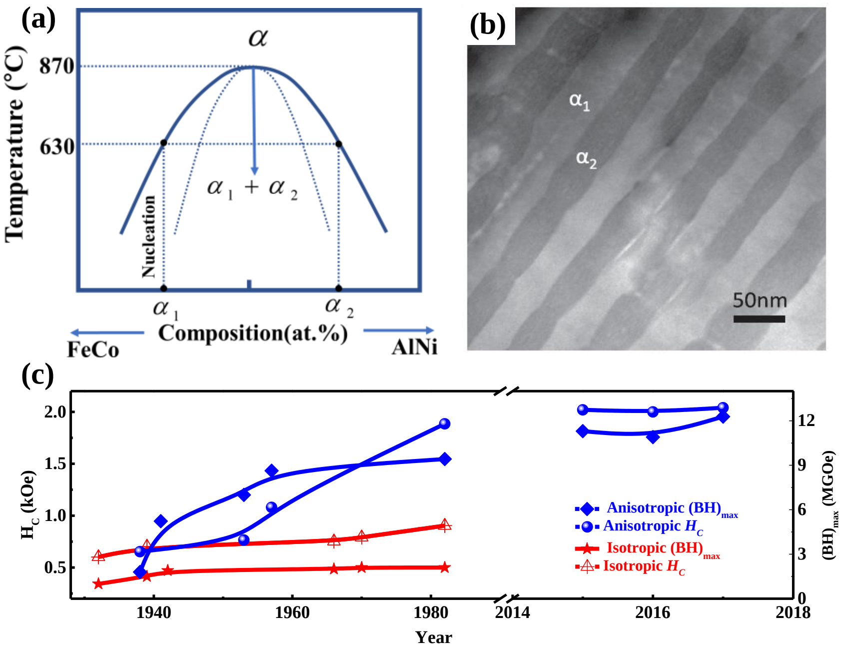

Figure 1.15 (a) Schematic representation of Alnico phase diagram depicts the spinodal decomposition process. The α_1 (FeCo-rich) and α_2 (NiAl-rich) phases originate from the parent bcc phase via spinodal decomposition. (b) Scanning transmission electron microscopy (STEM) image shows a side view of α_1 rods distributed in the α_2 matrix in an Alnico 8 alloy.[65] (c) the corresponding development in coercivity and energy product in Alnico magnets.

Recent theoretical research proposed that a promising $(BH)_{max}$ of 21.4 MGOe and H_C of 3.9 kOe can be obtained via the optimization of microstructures.[18] Meanwhile, the Stoner-Wohlfarth theory predicted that a maximum energy product $(BH)_{max}$ of 49 MGOe for a 67 vol% packed $Fe_{65}Co_{35}$ nanowires with radius less than the coherence limit (~10 nm).[66] The above two predictions reignited interests in Alnico magnets for future development.

1.3.4 Co Nanowires with High Aspect Ratio

The magnetic hardening in single crystal and single domain hcp-Co nanowires (NWs) is attributed to the use of shape anisotropy and exploitation of nanoscale effects. Moreover, during the synthesis, the growth of hcp-Co prefers to take the c-axis direction as shown in Figure 1.16 a-c. As c-axis is the easy axis and parallel to the long axis of the NWs, the corporative effect of the MCA and the shape anisotropy would lead to a giant anisotropy field and lifts the upper limit of H_C for hcp-Co NWs to 16.5 kOe.

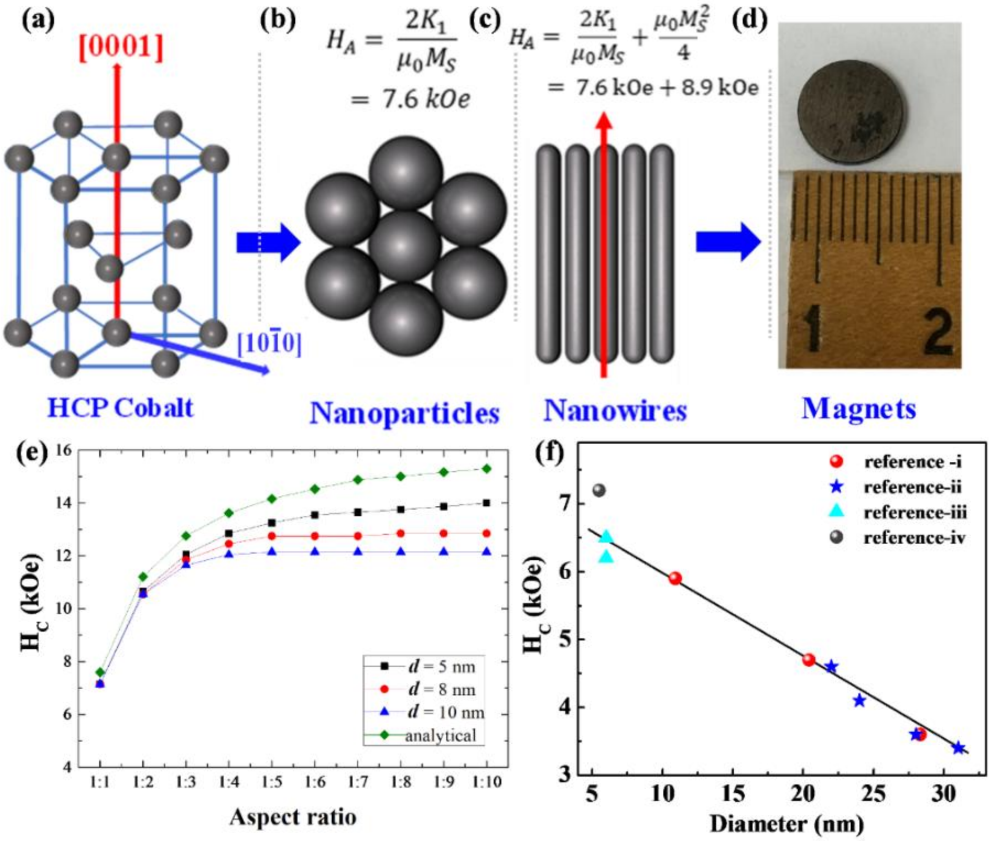

Figure 1.16 Schematic view of (a) crystal structure of hcp-Co. (b) and (c) the magnetic anisotropy sources and the corresponding anisotropy field (H_a: theoretical upper limit of coercivity field) for nanoparticles and nanowires. The red arrow in figure c represents easy axis direction that is parallel to the long axis of NW. (d) The digital photograph of the pellet of Co NWs assemblies.[67] (e) Evolution of the H_C of Co cylinders as a function of their aspect ratio for different diameters. The prediction of analytical result is plotted as a red continuous line.[68] (f) The experimental H_C

values obtained for Co nanowires/nanorods synthesized via polyol-based reduction of Co-carboxylate shows a linear trend with diameter (*Ref.* i to iv[68-71]).

Using micromagnetic simulations, it is possible to calculate the hysteresis curves for nanorods and nanowires with the variation of diameter, aspect ratio, and the tip morphologies. It has been observed that irrespective of the morphology, the coercive field increases as the aspect ratio is increased up to a ratio of 10, after which the coercive field barely changes. Moreover, in the case of nanorod/nanowire with less ideal shapes than the perfect ellipsoidal, a strong loss of coercive field of about 20% is observed. The loss is attributed to the relatively high demagnetizing field localized at these tips.[68, 72] This local increase of the demagnetization field acts as a nucleation point, which triggers the magnetization reversal along the wire. Thus, the coercivity of such an object is reduced compared to the case of a perfect ellipsoid. For the ellipsoid with homogeneous demagnetizing field, the coherent rotation model is valid only when the radius of the ellipsoid approaches $D_{coh} \leq 7.3 l_{ex}$. The coherent radius limit for Co NWs is 7.5 nm. Thus, in 1.18e, the coercive field of cylindrical particles increases with the decrease of diameter from 10 nm to 5 nm. The H_C value expected from the analytical model, which is an upper limit of H_C, is plotted in green for comparison. In cylinders with a very small aspect ratio, i.e. from 1 to 2, the H_C values obtained from the micromagnetic model are identical to the analytical prediction. Thus, the magnetization reversal can be considered as coherent rotation. However, when the aspect ratio increases, the H_C value is reduced with respect to that of the analytical model, which is due to the incoherent rotation of the magnetization. Moreover, when the aspect ratio goes above 8 the H_C no longer increases. The micromagnetic simulations thus provide the following guidelines to produce high coercivity nanowires: the diameter should be close to the D_{coh}, and the tips of the wires should be as rounded as possible to avoid providing a nucleation point.

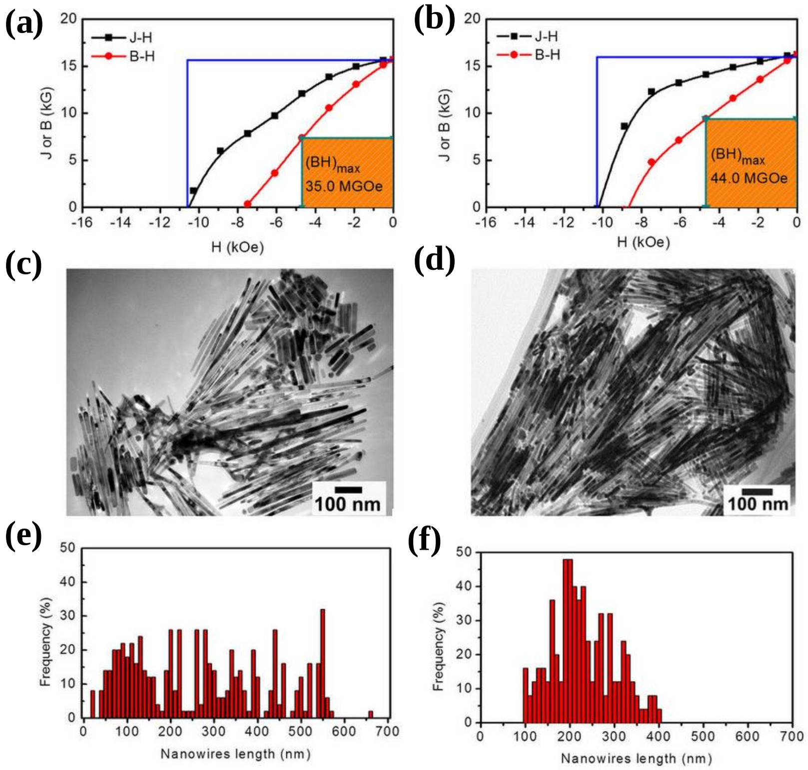

Figure 1.17 Second quadrant B-H curves for the aligned Co nanowire assemblies (along the easy axis) at 300 K. (c, d) TEM images of the Co nanowires corresponding to samples (a) and (b) respectively. (e, f) The histograms of the Co nanowires showing their length distributions of the samples shown in (c, d) respectively obtained using statistical analysis of ~600 nanowires each.[67]

To obtain the single crystal and single domain hcp-Co NWs, various approaches such as chemical synthesis, electrochemical growth using anodic aluminum oxide template, and physical deposition have been adopted.[73-76] However, the polyol-soft-chemistry process thrived alone to prepare high-coercivity Co NWs of well-controlled morphology.[77] For a better comparison, the experimental H_C obtained for Co nanowires or nanorods synthesized via the polyol-soft-chemistry is summarized in Figure 1.16f. The experimental H_C values are comparable to the theoretical predictions only for smaller diameter Co nanowires ($d \leq 10$ nm). Moreover, the H_C values increase linearly with the decrease of diameter. A significant improvement in H_C was observed when the mean diameter was decreased to less than 10 nm, resulting in H_C values higher than 7 kOe. Based on the high shape anisotropy and alignment of the nanowire assemblies, a record high room-temperature H_C of 10.6 kOe (843.5 kA/m) was obtained in single crystal Co nanowires.[67, 78] As a result, $(BH)_{max}$ estimated based on a 100% volume fraction of closely packed Co nanowires reaches 44 MGOe (350.1 kJ/m^3). Figure 1.17 also demonstrated that the uniformity in morphology of the nanowires is vital to achieve the high coercivity and high energy density. While keeping the NWs diameter constant, the variation of the length distribution from narrow (Figure 1.17c and e) to wide (Figure 1.17d and f) can decrease the energy product by 25%.

Chapter 2 Experimental Methodology and Related Physics

2.1 Materials Synthesis

There are generally two approaches for producing nanoscale objects, the top-down approach, and the bottom-up approach. The former means tailoring large scale objects into nanoscale objects and has an advantage for scaling-up productions. However, it also has some disadvantages, such as high cost and large critical dimension. High energy ball milling, electron lithography are the typical top-down approaches.[79, 80] In comparison to the top-down approach, bottom-up approach is to build up nanoscale objects from atoms or molecules. It is capable of synthesizing objects with size from a few nanometers to micron size. Furthermore, bottom-up approach has the advantage in shape control of nanoscale objects. Chemical reduction method, Electrochemical method, and molecular beam epitaxial are the typical bottom-up approaches.[75, 81, 82] Figure 2.1 displays the schematic view of magnetic NPs synthesized using top-down and bottom-up approaches. In this thesis we will focus on the bottom-up methods.

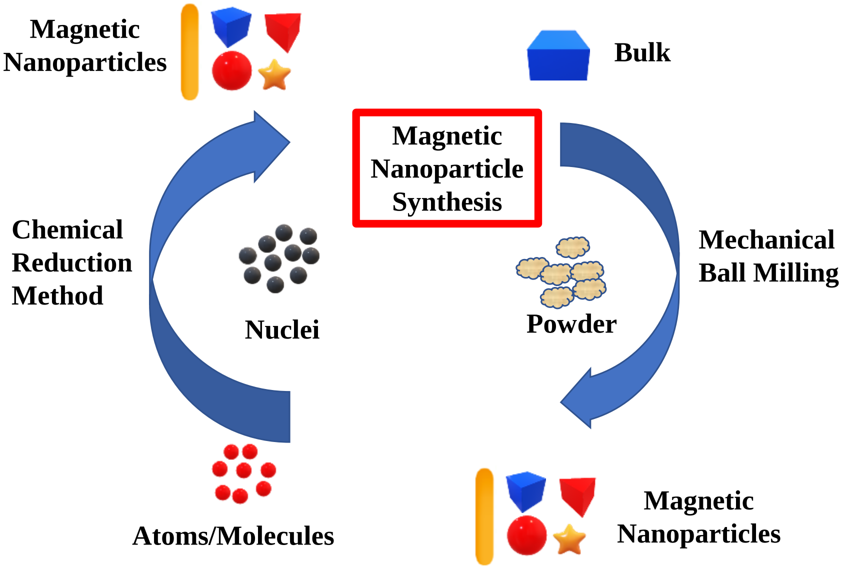

Figure 2.1 Schematic view of top–down (right side) and bottom–up (left side) approaches for the synthesis of magnetic nanoparticles.

2.1.1 Nucleation and Growth Mechanism-LaMer Theory

The liquid-phase chemical synthesis method has flourished in producing high-coercivity transition-metal-based nanorods and nanowires of well-controlled morphology. The homogeneous nucleation and growth process can be explained in view of LaMer model.**[83]** As illustrated in Figure 2.1, the synthesis of nanocrystals involves three consecutive stages: generation of atoms, self-nucleation, and growth by diffusion. During stage I, when the concentration of 'monomers' increases to the nucleation threshold; nuclei start to form. At stage II, the burst of nucleation occurs, leading to the formation of nuclei and thus a rapid decrease of the monomer concentration. When the concentration drops to the level below the nucleation threshold in stage III, there are no new nuclei forming. In the growth stage, Gibbs free energy drives the attachment of monomers to the facets of nuclei. The growth process continues until the monomer concentration drops below the saturation level. However, due to the higher surface energy of the nanoparticle with smaller size, they can dissolve into the solution to form monomers, which is known as Ostwald ripening.[84] As a result, the nanoparticles of the final reaction product are polydisperse. To avoid Ostwald ripening and prepare monodisperse nanocrystals, it is critical to shorten the nucleation process and to maintain the uniform rate of growth around each nucleus. Reducing the nucleation process aims to separate the nucleation and growth process. In this thesis, we have investigated the synthesis of monodisperse Co NWs, FeC NPs, Co NPs and NiC NPs.

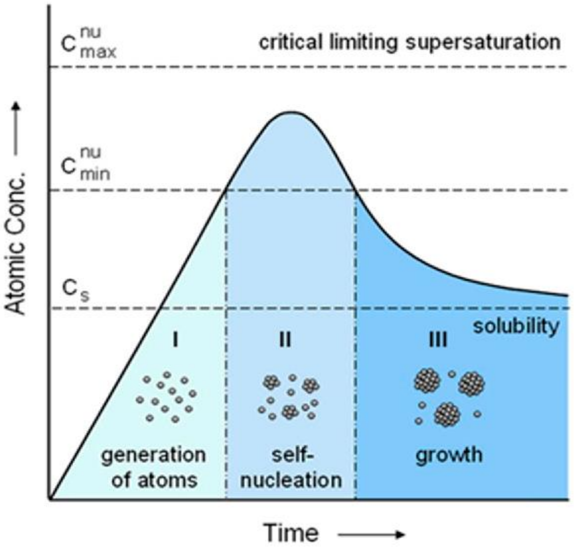

Figure 2.2 LaMer model illustrates the separation of nucleation and growth during the synthesis of monodisperse nanocrystals. C_S and $C_{\max}^{nu}$ are equilibrium and supersaturation concentration of monomers, respectively.[83]

2.1.2 Growth Mechanism of Anisotropic Nanoparticles

The manipulation of the growth regime is important in determining nanocrystals shape. Gibbs-Wulff theorem predicted the equilibrium shape from the thermodynamic stability of facets. The shape of a small crystal is determined by the minimization of the sum of surface energies over all crystal facets which can be calculated by Wulff construction shown in Figure 2.3.[77, 85, 86] As a result, the minimization of the chemical potentials of the crystallographic facets leads to the selective growth along the high-energy crystal facets and thus results in anisotropic nanoparticles. The effective surface energy of nanocrystals can be tuned via using the long-chain capping ligands such as phosphines, carboxylates, or amines which can preferentially adsorb onto a certain crystallographic facet.

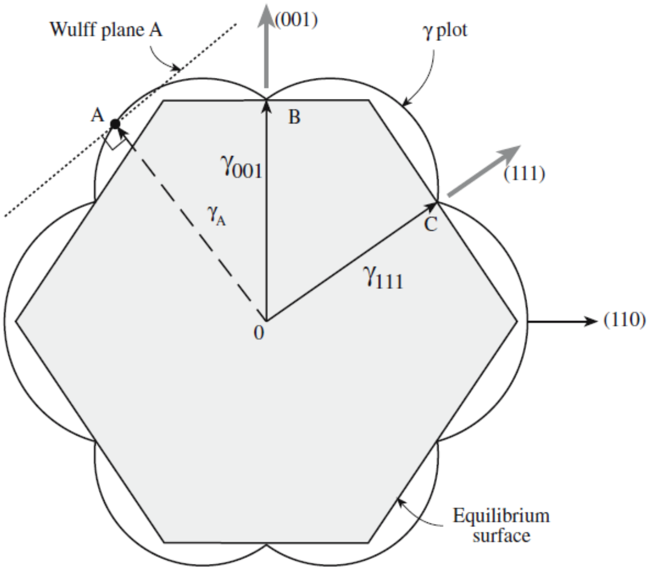

Figure 2.3 Wulff plot looking along the $[1\bar{1}0]$ direction for a fcc crystal.

For example, $BiFeO_3$ nanorods are obtained by introducing oleylamine as the surfactant. The oleylamine molecules have different affinity to different crystal surface. The surface with lower density of oleylamine grows faster than those with higher density, leading to the one-dimensional nanocrystals shown in Figure 2.4. In fact, the shape of nuclei can be also controlled by modulating reaction environment such as temperature, solution concentration, surfactant content or use of catalyst. In this thesis, we have investigated the growth of anisotropic Co NPs and iron carbide NPs.

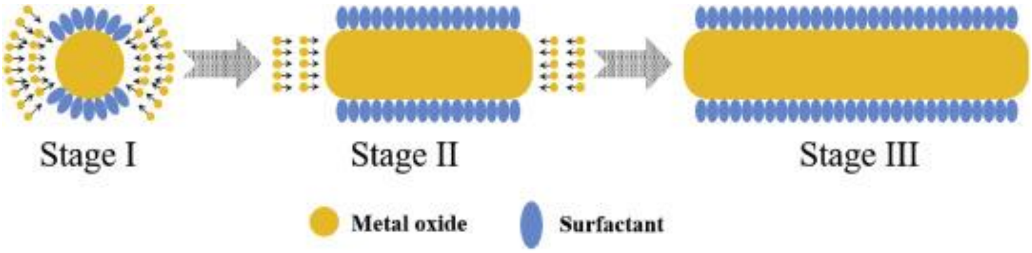

Figure 2.4 The schematic representation for the growth mechanism of $BiFeO_3$ nanorods.[87]

2.1.3 Solvothermal Method

Solvothermal processing is heterogeneous aqueous reactions in a sealed and heated container carried out under high-pressure at high temperatures. These supercritical conditions expedite the kinetics of the hydrolysis reactions. The enhanced temperatures increase the solubility of most ionic species. As a result, the viscosity of solutions decreases. The increased mobility allows growth process at a faster rate and the uniformity of the precipitates improves. Size and morphological control in solvothermal reactions is achieved by controlling reaction time, heating rate and reaction temperature. The final crystalline products usually have a varied morphology such as nanowires, nanotubes, nanoplates, nanocubes and nanospheres. Cetyl-trimethyl ammonium bromide (CTAB), olelamine, hexadecylamine, trioctylphosphine oxide and sodium dodecylsulfonate have been used as long chain capping agents in solvothermal reaction.[81, 88, 89] In this thesis, we adopted the solvothermal method to synthesize Co anisotropic nanocrystals.

2.1.4 Thermal Decomposition Method

In thermal decomposition method, the decomposition of organometallic precursors is mainly driven by heat. The relatively low decomposition temperature of organometallic compounds is a distinct advantage over the other processing techniques. Because size and morphology play a significant role for influencing the magnetic properties of the nanoparticles, control of the size and shape is a primary goal. The manipulation of decomposition temperature and heating rate is used to control the nanoparticle growth and thus tune the uniformity, size and morphology of final nanocrystals. In many cases, polymers, organic capping agents or templates are used to limit the size of the nanoparticle. For example, hcp-Co disk-shaped nanocrystals were obtained by rapid decomposition of cobalt carbonyl in the presence of primary amines.[90] In this thesis, we adopted the thermal decomposition method to synthesize iron carbide nanocrystals and nickel carbide nanocrystals.

2.2 Materials Characterization

2.2.1 Morphological Characterization

For the scanning electron microscopy (SEM), the interaction of the electron beam with the sample causes the valence electrons (secondary electrons) near the sample's surface to be ejected, which are then collected by detectors. By scanning the beam across the surface of the sample, enough secondary electrons are collected by detectors to image the surface features, however it does contain atomic number or elemental information. It allows the study of the morphology of the particles, the particle size, and can image the fracture surfaces. In this thesis, the morphology of the samples were studied via images recorded by a Hitachi S-4800 II Field emission scanning electron microscopy (FE-SEM) operated at acceleration voltage of 0.5-30 kV. EDX (Energy Dispersive X-ray) detector connected to the SEM was used for studying the elemental composition of samples. The samples were mounted on an Aluminum sample stub or Si substrates using double-sided carbon stick tabs.

The second type of electron microscopy is transmission electron microscopy (TEM). TEM also uses electron beam, but rather than collecting secondary electrons, the beam strikes the sample, and depending on the thickness, parts of the beam will transmit through the sample. The transmitted portion of the beam is focused through an objective lens and captured by a screen. From there they are redirected where they are collected, and the image is magnified. Limitations of the TEM include the sample thickness, which must be less than 100Å, as well as the projection of a 3D sample as a 2D image. In this thesis, Hitachi H-9500 high-resolution transmission electron microscopy (HR-TEM) operated at an accelerated voltage of 300 kV was also used to characterize the morphology of the samples. The HRTEM samples were prepared using the 300 meshes copper grid with a deposited carbon film on one side. The NPs were dissolved in the solvent (chloroform/toluene). One drop of the nanoparticle dispersion liquid was put on the formvar side of grid and was allowed to dry in air. To be mentioned, the nanoparticles should be cleaned many times to get rid of the excessive surfactants before preparing the HRTEM samples. Excessive surfactants result in the block of the transmission of the electron beam through the sample, decreasing the contrast and hence preventing the clear observation of the nanoparticles.

2.2.2 Phase and Crystallographic Structure Characterization

X-ray diffraction (XRD) is an analytical technique used to analyze the crystalline nature of a solid material. It is a popular and useful tool because it is a relatively fast and is non-destructive to the material being tested. The mechanism behind XRD based on the constructive interference of monochromatic X-rays and a crystalline sample. A cathode ray tube generates X-rays which are filtered to produce monochromatic radiation and concentrated towards a sample. The interaction between the X-rays and the sample produces constructive interference when Bragg's law is satisfied shown in equation 2.1.[91] A schematic for Bragg diffraction is shown in Figure 2.5.

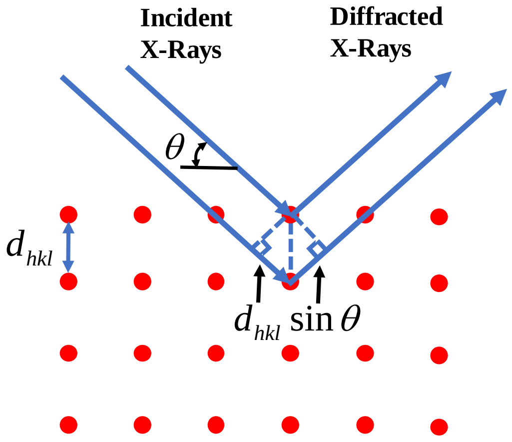

Figure 2.5 Schematic of Bragg Diffraction.

$$n\lambda = 2d_{hkl} \sin\theta \qquad 2.1$$

where n is an integer value, λ is the wavelength of the incident X-rays, d_{hkl} is the interplanar spacing between adjacent crystal planes, and θ is the angle at which constructive interference occurs. The most common X-ray source is a Cu Kα source, which emits a wavelength of 1.5418 Å. This wavelength is an average between the Cu Kα_1 ad Cu Kα_2 emission lines. X-rays penetration depths are on the order of hundreds of nanometers for most materials, making XRD a bulk materials analysis technique.

As mentioned above, in a typical experiment a sample is irradiated with X-rays over a range of angles. At angles where Bragg's Law is satisfied, constructive interference occurs. The constructive interference results in the detection of increased signal and the formation of a peak on the collected diffractogram. The diffractogram plots the intensity of the signal for various angles of diffraction at their respective two theta positions. The intensity of the peaks is related to the number of molecules with that spacing. The width of the peaks is inversely related to the crystal size. In a basic analysis, collected diffractograms are compared to known standards. The most extensive database of XRD standards is maintained by the International Centre for Diffraction Data (ICDD). For advanced analysis, peak position, peak width, and peak intensity can be used to determine the lattice parameters, crystal size, and crystal shape for a given material. In our laboratory, Rigaku Ultima IV diffractometer with Cu Kα wavelength (1.5406 Å) X-ray source was used to collect the powder X-ray diffraction (XRD) spectra and characterize the crystal structure of the prepared samples.

2.2.3 Magnetic Characterization

A vibrating sample magnetometer (VSM) in a physical property measurement system (Quantum Design Dynacool-PPMS) capable of fields up to 9 T (90 kOe) was used to study the magnetic properties of the samples. The system uses a superconducting coil with a dry sample chamber, cooled to cryogenic temperatures (4K) by liquid helium, to produce large magnetic fields. The samples were attached to a Quantum Design brass sample holder with GE varnish, sandwiched between two pieces of quartz and wrapped in Teflon tape to prevent rotation of the sample during the switching applied field direction. A schematic of the basic setup for a VSM coil is shown below in Figure 2.6. In a typical VSM measurement, a magnetic sample is placed between two electromagnets and vibrated at a constant frequency and amplitude. A uniform magnetic field is then applied perpendicular to the axis of vibration which causes the sample to magnetize and permeate magnetic flux on its surroundings. This magnetic flux causes Faraday Induction and generates an electric potential. The amplitude of electric potential is then measured by coils located next to the vibrating sample. The amplitude of electric potential generated is directly proportional to the magnetic moment of the sample. The measurements were performed in magnetic fields, ***H***, up to 9 T (90 kOe) at temperatures from 1.8 K to 1000 K. The VSM is calibrated using a cylindrical standard sample with a resolution of 0.016 mT.

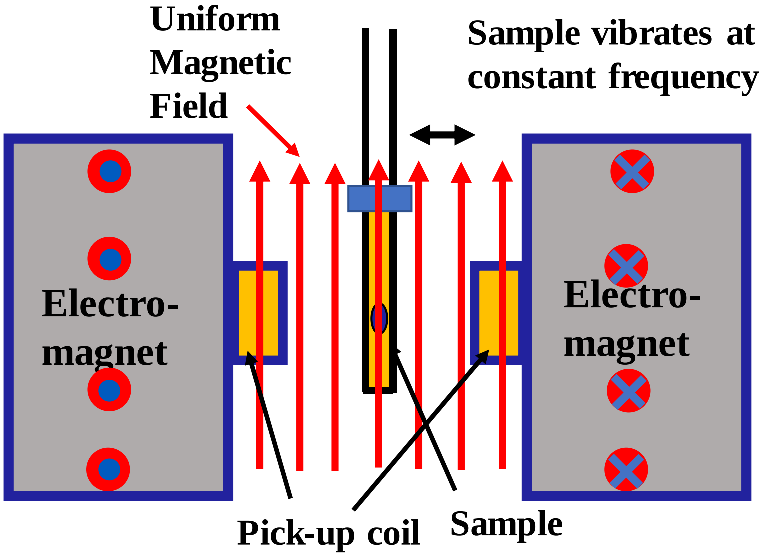

Figure 2.6 Basic setup for VSM coil.

2.3 Error Analyses

The limitation of accuracy of the characterization machine limits the maximum precision of the measurements. To maintain high accuracy and to reduce the systematical error in the magnetic measurements, the machine is calibrated with the standard sample before it is used to measure the samples. In addition, there is a mean field region in the VSM coil, which requires the sample size and position fit to the center in order to reduce the random error of the measurement. There will be error from the samples such as the presence of surfactants which will also affect the magnetization values of the sample and must be accounted for when calculating the true *M* value. To decrease these random errors, repeated measurements were adapted. Due to the repeatable measurements, statistical analysis of data is crucial to display and record the obtained values. Standard Deviation (SD) is used for descriptive error bars because they show how the data are spread. SD is calculated by the formula:[92]

$$SD = \sqrt{\frac{\sum_{1 \le i \le n} (x_i - \overline{x})^2}{n-1}} \qquad 2.2$$

Where x refers to the individual data points, $\overline{x}$ is the mean vale, and $\sum$ means to calculate the sum value of all of the n data points. Moreover, there will be some error from the data analysis such as the particle size calculation. Thus, the particle size distribution histograms are fitted with the Log-normal distribution function. In our work, we estimated error bars to show data accuracy.

Chapter 3 Magnetic Hardening and Exchange Bias in Co Nanoparticle Assemblies

3.1 Introduction

Cobalt is one of the most important 3*d* transition metal elements used in the development of magnetic materials, especially in hard magnetic materials, from the early Co-based steel magnets to the rare-earth permanent magnets based on the 3*d*-4*f* compounds. Like Fe, Co possesses a high M_S and a high T_C. Unlike Fe, Co has high magnetocrystalline anisotropy due to its spin-orbit coupling. As a result, it can be used to achieve a high degree of magnetic hardening in its elemental materials. In addition, Co atoms can crystallize into three phases including hexagonal close-packed (hcp), face-centered cubic (fcc) or ε-phase (β-manganese-type simple cubic structure) with distinct magnetic properties.[93, 94] The hcp-Co is magnetically anisotropic compared to fcc-Co and ε-Co due to its non-cubic crystalline symmetry[8]. The appreciable uniaxial magnetocrystalline anisotropy (MCA) (5.3 Merg/cm^3) compared to the low MCA of fcc-Co (2.7 Merg/cm^3) and ε-Co (1.6 Merg/cm^3) makes hcp-Co the preferred structure for magnetic recording and permanent magnets.[95, 96] Indeed, the use of magnetic nanoparticles for high density magnetic storage requires small nanoparticles with high magneto-crystalline anisotropy at usable temperatures.[97] To apply Co nanoparticles in advanced applications, it is critical to control the shape, size, phase, and the surface defects. An intensive research has been focused on the synthesis of monodispersed Co nanoparticles.[90, 98, 99] However, all the synthesis process either resulted in the mixed phase containing ε-Co spheres or displayed the compromised magnetic properties due to surface spin disorder effects.

Another interesting phenomena in Co nanoparticles is that they are prone to surface oxidation and the developed Co/CoO core-shell nanoparticles exhibited prominent exchange bias behavior.[100] Exchange bias is shown to be induced by the strong exchange coupling between the ferromagnetic (FM) Co core and the antiferromagnetic (AFM) CoO shell. The typical exchange bias effect is an obvious shift of the hysteresis loop against the applied field, commonly referred to as an exchange bias field, H_{EB}, when field cooling the sample from temperatures above the Néel temperature T_N of the AFM to temperature below T_N. Due to the use of exchange bias in magnetic sensors and as stabilizers in magnetic reading heads, it has attracted a flurry of research.[101, 102] Even though it was investigated for more than 60 years, the underlying mechanism remains controversial.[103, 104] Uncompensated spins associated with the antiferromagnet or their interfaces have early been suggested to mediate the coupling between AFM and FM materials. Moreover, all the investigations are about the exchange bias of Co/CoO core-shell nanoparticles with fcc-Co core, which intrinsically possess low magnetic anisotropy. There is no research about the exchange bias in hcp-Co core with CoO shell attributed to the challenge of successful synthesis of hcp-Co nanocrystals.

Here, we report the successful synthesis of hcp-Co nanoparticles with prominent magnetic properties via using the solvothermal method. In order to tune the magnetic properties, the size of Co nanoparticles was modulated from 12 nm to 17 nm by manipulating the Co-precursor to long-chain amine concentration. In addition, the interface coupling between FM Co core and AFM CoO shell has been controlled via manipulation of surface oxidation in hcp-Co nanoparticles (NPs) to study the H_{EB} behavior. We also identified and separated two distinct contributions to the training effect (TE): the symmetry of the anisotropy of the antiferromagnet and the atomic spin relaxation.

3.2 Synthesis of Monodisperse Co and Co/CoO Nanoparticles

In a typical synthesis of 14.0 nm Co NPs, 1 g (2 mmol) of cobalt (II) laurate, 2 g (8 mmol) of hexadecylamine and (60 mg) $RuCl_3$ were dissolved in 30 ml of 1, 2 Butanediol in a teflon bottle. The teflon bottle was purged with forming gas (Ar 93% + H_2 7%) for 5 min then placed in an ultrasonic water bath adjusted to 65°C for 60 min. Then, the teflon bottle was transferred to an autoclave reactor and heated at 250 °C for 75 min. The obtained precipitates were cleaned in chloroform using centrifugation. Further increasing HDA to 12 mmol results in the formation of Co NPs with diameter of 12.5 nm. When 1.95 ml oleic acid was introduced to replace HDA, 17.0 nm Co NPs were obtained. The oxygen was introduced naturally by putting the Co NPs solution in the air to form the cobalt oxide (CoO) shell covering the Co clusters, which ensures that all Co clusters are uniformly oxidized. Via controlling the air exposer time, the thickness of CoO shell is manipulated.

Powder X-ray diffraction (XRD) spectra were collected from a Rigaku Ultima IV diffractometer with Cu Kα wavelength (1.5406 Å) X-ray source to characterize the crystal structure of the as-prepared Co NPs. In order to analyze the morphology of Co NPs and Co/CoO core-shell NPs, High-resolution transmission electron microscopy (TEM) images were taken using a 300 kV Hitachi H-9500 TEM. The TEM sample was prepared following the method described in section 2.2.1. A Hitachi S-4800 II Field emission scanning electron microscopy (FE-SEM) operated at acceleration voltage of 0.5-30 kV was also used to record images to study the morphology of Co NPs. The magnetic properties of the samples were studied using a physical property measurement system (Quantum Design Dyanacool-PPMS). For exchange bias measurement, hysteresis loops were measured at 10 K, 25 K, 50 K, 75 K, 100 K, 125 K, 150 K, 175 K, 200 K, 250 K and 300 K under field cooling (FC) in 50kOe from 300K to 10 K for Co nanoparticle assemblies. The zero-field-cooled (ZFC) magnetization were measured over the temperature range 10-300 K with an applied field of 50 kOe. The frequency dispersion of the AC susceptibility (f = 11, 110, 1110 and 9984 Hz; amplitude of 5 Oe) was measured as a function of temperature.

3.3 Magnetic Hardening in Co Nanoparticle Assemblies

The TEM image as shown in Figure 3.1a indicates that the prepared Co NWs have uniform size distribution with a mean diameter of 12.5 nm. All the XRD patterns of Co NPs with varied size display five diffraction peaks which corresponds (100), (002), (101), (102) and (110) planes of pure hcp-Co phase as shown in Figure 3.1b. The sharp and prominent peaks exhibit the pure phase and good crystallinity of hcp-Co NPs with varied diameter.

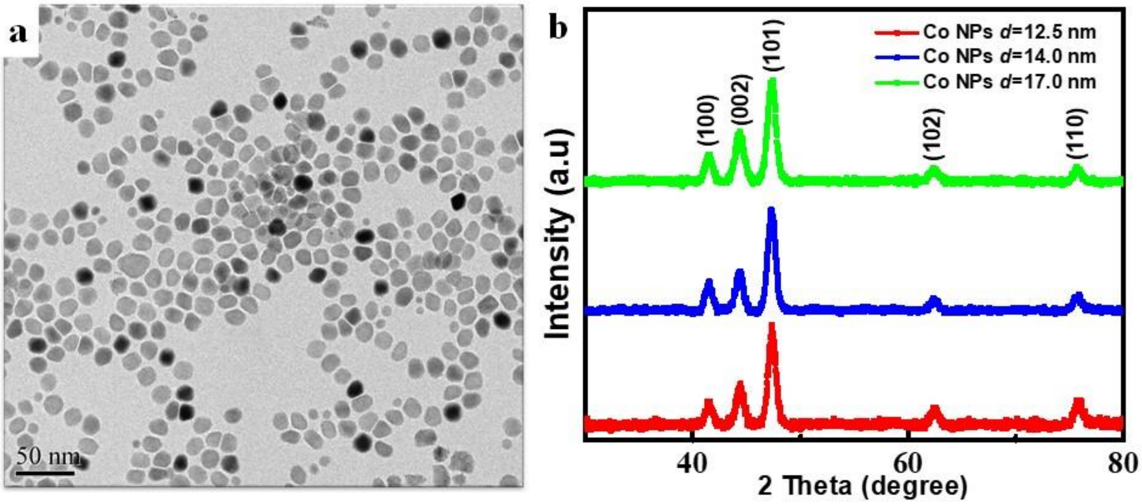

Figure 3.1 (a) TEM micrograph of the as-prepared Co NPs. (b) XRD patterns of Co NPs with diameter of 12.5 nm, 14.0 nm, and 17.0 nm.

Figures 3.2a-c display SEM image of the Co NPs, which confirm the efficacy of the solvothermal chemical process in synthesizing monodispersed Co NPs with different diameters.

The histograms of diameter distributions as shown in the insets of Figure 3.2a-c demonstrated the size of Co NPs can be well controlled in the range of 12.5 nm to 17.0 nm with simultaneously tuned magnetic properties. The coercivity of Co NPs increases from 0.9 kOe to 2.7 kOe with the increase of diameter from 12.5 nm to 14.0 nm as shown in Figure 3.2e-f. The further increase of diameter from 14.0 nm to 17.0 nm yields a reduced coercivity of 2.3 kOe. The corresponding coercivity mechanism is discussed in the following part.

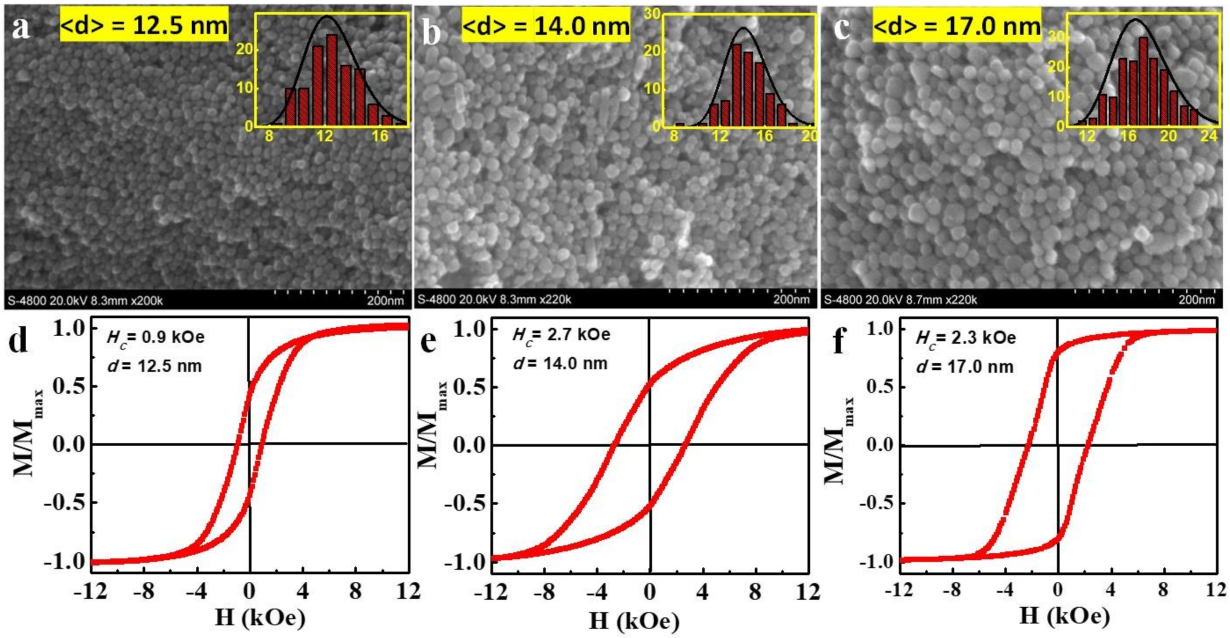

Figure 3.2 (a-c) SEM micrographs of Co NPs with mean diameter of ~ 12.5 nm, 14.0 nm, and 17.0 nm, respectively. The insets are the histograms of diameter distributions of Co NPs. In the histogram, the x-axis represents diameter and the y-axis represents the counts. (d-f) M-H plots of Co NPs at room temperature.

The coercivity dependence of diameter of Co NPs is summarized in Figure 3.3. The curve exhibits two different stages with respect to diameter which are corresponding to different magnetization reversal mechanisms. The coercivity first increases with the increased diameter and the maximum coercivity of 2.7 kOe is obtained in Co NPs with mean diameter of 14.0 nm. This is congruent with the discussions in 1.2.2.3 Coercivity Mechanisms in Nanoparticles, as long as the radius of the Co NPs is near coherent radius $R_{\mathrm{coh}} = \sqrt{24}\, l_{\mathrm{ex}} = 9.7$ nm, the ultrasmall Co NPs exhibit the coherent magnetization reversal which needs larger magnetic field to switch the spins. As a result, a pronounced coercivity of 2.7 kOe is achieved in the Co NPs. The reduced coercivity of the Co NPs with diameter smaller than 14 nm is owing to the thermal fluctuation effects. In addition, the decreased coercivity with the further increased diameter is resulted from the fact that the magnetization reversal in Co NPs is not the coherent rotation.

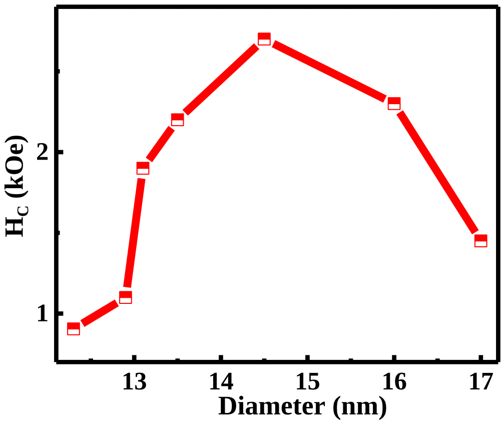

Figure 3.3 The coercivity dependence of diameter of Co NPs.

3.4 Exchange Bias in Co/CoO Core-Shell Nanoparticles

To investigate the phase evolution with the oxidation time, the XRD patterns of Co NPs with different exposure time to the air were collected (see Figure 3.4a). Compared to the XRD patterns of the as-prepared Co NPs (green curve), there is a small hump in XRD patterns of the Co NPs after one-week exposure time to air (blue curve). After one more week, the hump becomes more prominent (red curve). This peak corresponds to (111) plane of CoO, which reveals that the CoO shell thickness increases with the increased exposure time of Co NPs to oxygen atmosphere. The HRTEM images in Figure 3.4b and c also confirm the oxidation process. Figure 3.4b reveals the as-prepared Co NP is single-crystalline in nature and the distance between the lattice fringes is 0.192 nm which is close to the (101) planes of hcp-Co. While Figure 3.4c displays the nanoparticle has a clear core-shell structure. The shell consists of the amorphous matrix and the ultrasmall CoO nanocrystals with the lattice fringes of 0.204 nm which is close to the (002) planes CoO. This is consistent with the results of XRD analysis.

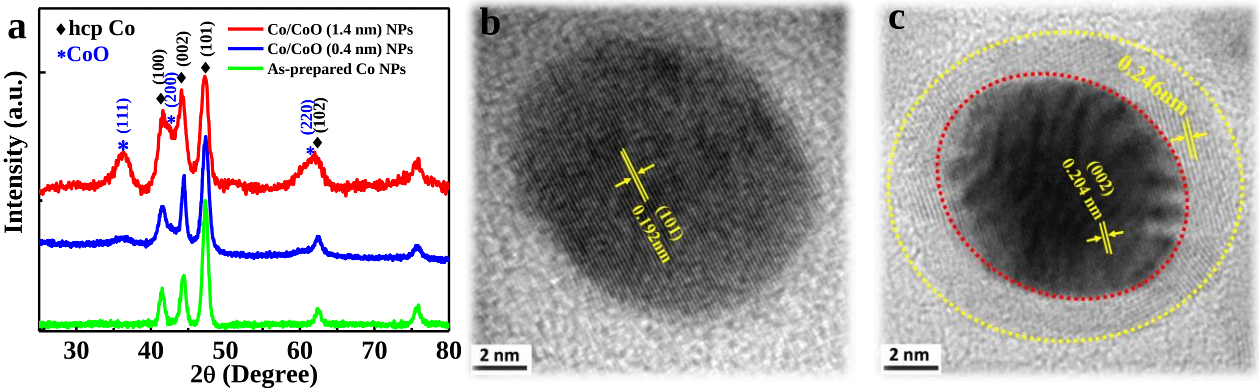

Figure 3.4 (a) XRD patterns of Co and Co/CoO NPs. (b) HR-TEM image pristine Co NP and Co/CoO core-shell NP.

The saturation magnetization (M_S) values of Co NPs and Co/CoO NPs are determined from the room temperature M-H loops (see Figure 3.5a). With the increased oxygen exposure time, M_S value decreases from 150 emu/g to 70 emu/g. The shell thickness t is calculated by using the following equation:

$$M_S = M_{S(pure)}\left(1-6\frac{t}{d}\right) \tag{3.1}$$

The obtained CoO thickness for the surface oxidized samples are 0.4 nm (135 emu/g), 0.7 nm (120 emu/g) and 1.4 nm (70 emu/g), which is in congruence with the results of HRTEM analysis. The shell thickness will have effects on exchange coupling between FM Co core and AFM CoO shell, and further affect the exchange bias field (H_{EB}) and training effect (T_E). There is no exchange bias in the as-prepared CoN Ps shown in Figure 3.5b. With the increase of the shell thickness, the maximum H_{EB} of 3.6 kOe is achieved in Co/CoO (0.4 nm) nanoparticles. The enhanced H_{EB} is attributed to the uncompensated spin structures of the spin disorder at the interface, which needs high magnetic field for the reversal.[102] The further increase of CoO shell thickness leads a sharp decrease of H_{EB} as the effective interface volume decreases when there is the formation of many small CoO crystallites with the increase of CoO thickness. The AFM spins at the interface needs comparatively lower field for the reversal. Moreover, H_{EB} rapidly decreases with the increased temperature and becomes undetectable above T_V = 150 K (T_V is the temperature where exchange bias appears and is called blocking temperature) shown in Figure 3.5b. T_V is much lower than the Néel temperature (T_N = 293 K) of the bulk CoO. The temperature dependence of H_{EB} indicates that exchange anisotropy disappears at about 150 K which is attributed to the superparamagnetic behavior of the AF oxide shell with very small crystallites above the blocking temperature ~150 K.

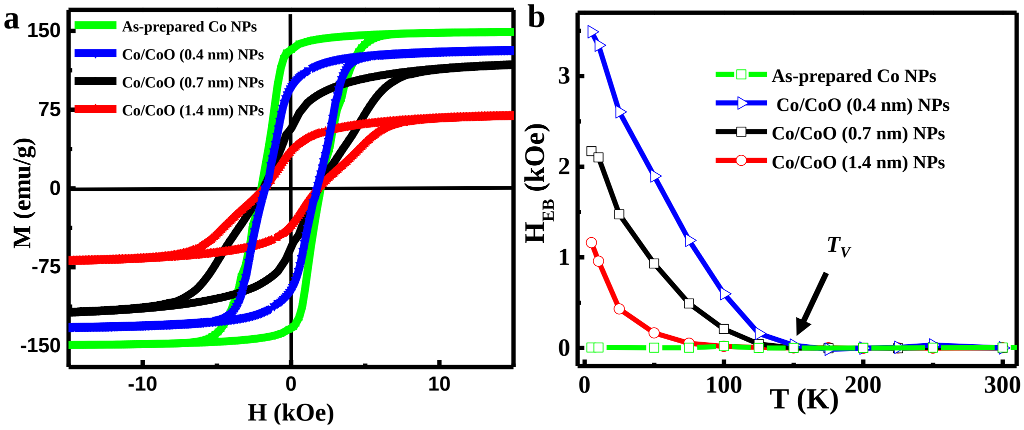

Figure 3.5 (a) Room temperature M-H loops of Co NPs and Co/CoO NPs. (b) Temperature dependence of H_{EB} Co NPs and Co/CoO NPs.

As training effect of exchange bias is related to the microstructure of core-shell system, TE of the Co/CoO nanoparticles shown in Figure 3.6 was measured to investigate the microstructure effect. The hollow points are experimental data. The solid lines are the fitting curves using the hybrid function:[105]

$$H_{EB} = H_0 e^{-(n-1)/\tau} + H_1 n^{-1/2} + H_{EB}^{\infty} \qquad 3.2$$

where H_0 and H_1 denote the component of the symmetry of the anisotropy in the antiferromagnet and spin relaxation modes in the training effect, respectively.[105, 106] H_{EB}^{∞} is H_{EB} field after the infinite training cycles, and τ is a characteristic relaxation time length which has the same dimension of time. The symmetry of the anisotropy in the CoO shell contributes to the training effects mainly due to the existence of multiple easy axes in the antiferromagnetic shell.[106] It can initially stabilize a noncollinear arrangement of the antiferromagnetic spins, which relaxes into a collinear arrangement after the first magnetization reversal of the ferromagnet. This effect is dominant in the first training circle. Training effect in the following circles mainly results from the spin relaxation below the spin glass transition temperature and is quite slow compared to that in the first circle. To be mentioned, with the increased shell thickness the value of $\frac{H_0}{H_0 + H_1}$(Table 3.1) enhances noticeably. For Co/CoO (1.4 nm) NPs, H_0 accounts 93% in training effect, which means the symmetry of the anisotropy in the antiferromagnet plays more and more significant role in the training effect. However, in Co/CoO (0.4 nm) NPs, H_1 contributes more in the training effect, which means spin relaxation dominates the training effect in Co/CoO NPs with thin CoO shell. This further confirms there is more spin disorder in Co/CoO NPs with thin CoO shell and the formation of the small CoO crystallites in Co/CoO NPs with thick CoO shell.

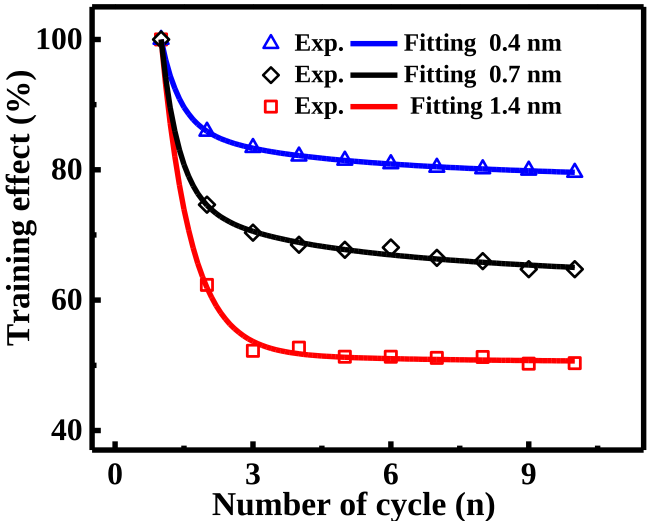

Figure 3.6 TE: Experimental data and fitting curves of Co/CoO NPs with varied CoO shell thickness**.** The hollow points are experimental data. The solid lines are the fitting curves using the hybrid function**.**

Table 3.1 Fitting parameters for TE of Co/CoO NPs using the hybrid function.

CoO t (nm)	H_0	H_1	$H_0/(H_0+H_1)$	$H_1/(H_0+H_1)$
0.5	378	487	44 %	56 %
0.7	363	365	50 %	50 %
1.4	544	41	93 %	7 %

To confirm the spin glass existence in the samples, zero field cooling M-T (Figure 3.7a) and temperature dependence of in-phase ac susceptibility $\chi'_{(T,f)}$ (Figure 3.7b) were measured. The first broad peak (black arrows) at 290 K comes from the T_N of CoO shell. The second peak (red arrows) at ~50 K represents the spontaneous magnetic order of solid oxygen.[107] The prominent increase of magnetization at lower temperature (< 50 K) reveals there is spin glass transition, which confirms the existence of the uncompensated spin structure leading the enhanced H_{EB} in Co/CoO (0.4 nm) NPs. The increase of magnetization becomes less prominent in Co/CoO (1.4 nm) NPs, which reveals the formation of crystalline CoO shell. Figure 3.7b reveals the presence of a “cusp-like” maximum in $\chi'_{(T,f)}$ locating at 6 K and shifting to the high temperature with the enhanced frequency. Such characteristics are expected for “ideal” spin glasses.[108] Moreover, spin glass can also be characterized by the value of φ.[109]

$$\varphi = \frac{\Delta T_f}{T_f \Delta \log f} = 0.047 \tag{3.3}$$

where T_f is the average value of the frequency-dependent blocking/freezing temperature determined by the maximum of $\chi'_{(T,f)}$, while ΔT_f represents the difference between T_f measured in the $\Delta \log f$ frequency interval. The parameter φ assumes values in the range 0.0045–0.06 for atomic spin glasses.[109] $\varphi = 0.047$ further confirms the spin glass state in Co/CoO (0.4 nm) NPs.

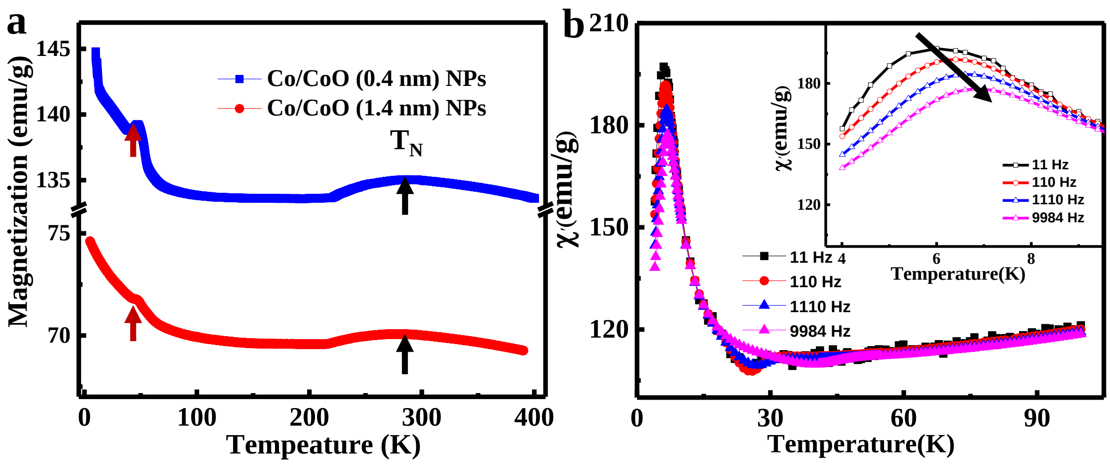

Figure 3.7 (a) Zero-Field-Cooling (ZFC) magnetization curve measured under magnetic field of 5 T of Co/CoO (0.4 nm) NPs. (b) The temperature dependence of the ac magnetic susceptibility was

measured with keeping the ac amplitude constant (H_{ac} = 5 Oe) at 11, 110, 1110 and 9984 Hz frequency for Co/CoO (0.4 nm) NPs.

3.5 Conclusion

The pure hcp-Co NPs is successfully synthesized via using the solvothermal method with the optimized reaction condition. Via introducing different surfactant, the size of Co NPs is tuned from 12.5 nm to 17.0 nm. With the decrease of size, the coercivity of Co NPs first increases to the optimum value of 2.7 kOe and then decrease to 0.9 kOe. The obtained record coercivity value of Co NPs results from the single crystal and ultrasmall size which is near the coherent diameter. Moreover, we have demonstrated a strategy to tune the exchange bias and training effect in Co/CoO nanoparticles by controlling the surface defects and the formation of small CoO crystallites. Following surface oxidation, the sample with ultrathin oxidation surface exhibited a giant exchange-bias field up to 2.7 kOe, whereas the H_{EB} for the sample with thick oxidation surface is only 1.2 kOe. The prominent H_{EB} is owing to the sufficient uncompensated spins in the surface with high spin disorder. The lower H_{EB} is attributed to the decreased effective interlayer resulting from the formation of CoO crystals in the shell. More importantly, Co/CoO nanoparticles with lower H_{EB} revealed a prominent TE with a large decrease of H_{EB} to 62 % from the first to the second cycles. The large training effects are attributed to the symmetry of the anisotropy of CoO. TE of the Co/CoO nanoparticles with thin shell is dominant by the spin-glass relaxation at the interface of Co/CoO core-shell. These results provide a powerful approach towards manipulating and optimizing the exchange bias effects via tuning the internal magnetic structure of nanoparticles for applications.

Chapter 4 Magnetic Hardening and Exchange Bias in Co Nanowire Assemblies

4.1 Introduction

Magnetic nanowires have attracted substantial interests in recent years because of their potential applications in the ultrahigh-density magnetic recording media and future permanent magnets.[69, 110-112] Moreover, the magnetic properties, particularly the coercivity of NWs, can be tailored by precise control of the geometry and morphology, especially the mean diameter and aspect ratio.[78] A typical example is hcp-structured Co NWs, which exhibit a giant shape anisotropy.[70, 112] In general, the magnetocrystalline anisotropy field is considered to be the theoretical upper limit of the coercivity in a ferromagnetic material and H_a value of hcp-Co is 7.6 kOe.[113] However, both the theoretical and experimental investigations have shown that the coercivity exceeding 10 kOe can be achieved in aligned Co NW assemblies, which is mainly ascribed to cooperating magnetocrystalline anisotropy and shape anisotropy contributions.[81, 114-116]

Magnetic performance of metallic nanowires may be robustly affected by shell oxidation. When they contact the air, there will be oxidation passivation and thus results in a finite sized shell of oxide. As a result, there will be the formation of ferromagnetic/antiferromagnetic (FM/AFM) interface and the hysteresis cycle can be biased due to the exchange bias (EB) effect. The investigation of exchange-bias has essentially been focused on the systems with FM/AFM interfaces such as core-shell nanoparticles[117, 118] and thin film systems.[119, 120] However, only a few reports were found on the EB effect in core-shell nanowires.[121-123] In the case of core-shell nanowires, EB is resulted from the interfacial exchange coupling between FM core and AFM shell.

An interesting topic is temperature dependence of coercivity in 1D core-shell nanowires with AFM shell. Is it same with 0D core-shell nanoparticles and 2D thin films.

This chapter we have demonstrated that the coercivity of the magnetically aligned nanowires in epoxy can reach up to a record high coercivity of 13.0 kOe, which is nearly double that of the randomly oriented NWs.[78] In addition, we explored the consequences of the exchange bias on the magnetic performance of 1D Co/CoO core-shell nanowires.

4.2 Diameter-Controlled synthesis of Co Nanowires

Co nanowires of different diameters were synthesized via a solvothermal method by controlling the cobalt (II) laurate to HDA mole concentration, as reported earlier by our group.[81] The Schematic view of solvothermal synthesis of Co NWs is summarized in Figure 4.1 . The mechanism of surfactant effect on the growth of anisotropic nanocrystals is already discussed in section 2.1.2 Growth Mechanism of Anisotropic Nanoparticles. In our synthesis process, the long-chain amine molecules adsorb more favorably on the lateral facets, which favors growth along the inefficiently passivated (0002) basal facet.[124] The preferred c-axis growth facilitates formation of perfect single crystals with wire-shaped morphology. HDA is used as the surfactants to control the length and uniformity of Co NWs and thus manipulates the magnetic properties of Co NWs.[15, 81, 125, 126] In a typical synthesis of Co NWs with length ~190 nm and diameter ~8 nm, 60 ml 1,2-butanediol, 2 mmol of cobalt (II) laurate, 0.0048 mmol of $RuCl_3$ and 4 mmol of HDA were taken in a Teflon-lined stainless-steel enclosure and heated at 250 °C for 75 min. The Co NW diameter was controlled by varying the Co-precursor to HDA mole ratio as 1:2 (8 nm), 2:3 (12 nm), 1:1 (15 nm) and 2:1(20 nm), respectively. While other reaction parameters such as the mole ratio of Co-precursor to $RuCl_3$, the heating rate, and the reaction time (75 min) were strictly maintained the same. Similarly, with keeping the mentioned reaction parameters same, the $RuCl_3$ was altered from

0.0048 to 0.12 mmol to control the lengths. For example, with keeping the Co NW diameter 8 nm, the length can be varied by adjusting the $RuCl_3$ content as 0.067 mmol (~160 nm), 0.077 mmol (~120 nm), 0.096 mmol (~100 nm) and 0.12 mmol (~80 nm), respectively. The control exercise over Co-precursor, HDA and $RuCl_3$ mole contents enables to control the aspect ratio over a wide range from 8 to 23. The as-synthesized Co nanowires are susceptible to oxidation when exposed to air. The Co/CoO core-shell nanowires were obtained in the same oxidation process as described in section 3.2.

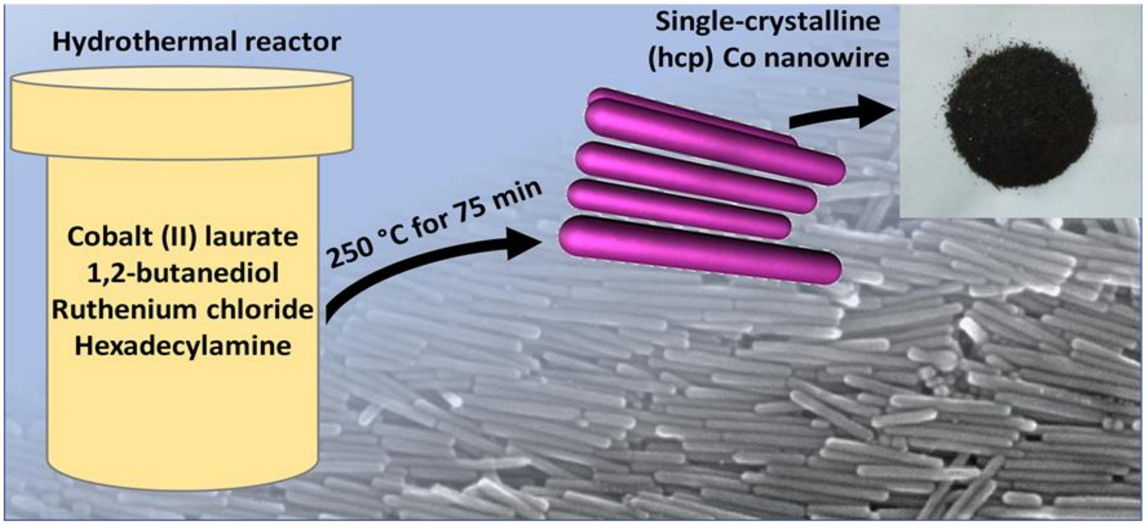

Figure 4.1 Schematic view of solvothermal synthesis of Co NWs.

Transmission electron microscopy (TEM) micrographs were obtained using a Hitachi H-9500 TEM operating with an accelerating voltage of 120 kV and 300 kV to characterize the morphology and crystal structure of Co NWs. The TEM sample was prepared following the method described in section 2.2.1. XRD patterns were collected on a Rigaku Ultima IV diffractometer with Cu *Kα* X-ray source. To measure the magnetic properties, the aligned Co nanowire assemblies were prepared. First, the as-synthesized Co NWs were dispersed in chloroform and then, a required amount of epoxy resin was added into the Co nanowires dispersion. The nanowires were uniformly dispersed in the epoxy with concentration 5-20 wt. % so that the magnetic interaction between neighboring nanowires can be neglected. This composite was then poured into a mold and allowed to cure under the external magnetic field of 2.0 T. Magnetic properties were measured using a Quantum Design Physical Property Measurement System (DynaCool PPMS-9T).

4.3 Magnetic hardening in the Aligned Co Nanowire assemblies

$RuCl_3$ is used as nucleation center to control the length and uniformity of Co NWs and thus the magnetic properties of Co NWs is manipulated. When $RuCl_3$ content increases from 0.067mmol to 0.12 mmol the length of Co NWs decreases from 190 nm to 80 nm with diameter approximate 9.0 nm demonstrated in Figure 4.2a-c. All of Co NWs have cylindrical morphology and uniform diameter. The average length estimated from the TEM micrographs using the lognormal distribution (see the inset of Figure 4.2a-c) are about 190 nm, 120 nm and 80 nm, respectively. The histograms display Co NWs with mean length of 190 nm and 120 nm possessing narrow length distribution compared to the Co NWs with mean length of 80 nm. The narrow length distribution is critical for squareness of M-H loop and maximum energy product. Moreover, Co NWs with average length of 190 nm and 120 nm display superb alignment under magnetic field of 2 T (see Figure 4.2a and b). However, when the mean length of Co NWs decreases to 80 nm, the aligned NWs possess a poor alignment shown in Figure 4.2c. As a result, hysteresis loop of Co NWs with longer length possesses better squareness (Figure 4.2d), which is congruent with the narrow distribution of length and good alignment of Co NWs. The record H_C value of 13.0 kOe and optimum energy product of 60 MGOe are obtained in Co NWs with mean length of 190 nm shown in Figure 4.2e and f. The higher H_C of Co NWs with longer mean length is also associated with the high aspect ratio which is already demonstrated in theoretical paper.[68] The Co NWs with higher aspect ratio have high nucleation field, which leads magnetization reversal at the high magnetic field and consequently results in good squareness of the hysteresis loop and an enhanced $(BH)_{max}$.

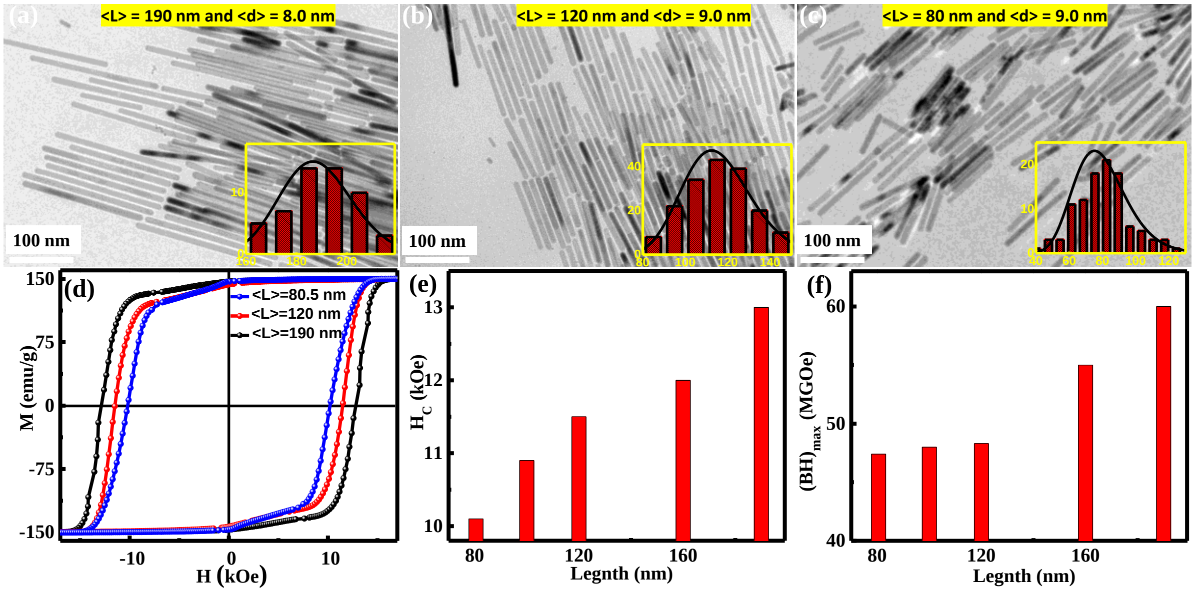

Figure 4.2 TEM images of Co NWs with average diameter of ~ 9.0 nm and mean length of (a) 190 nm, (b) 120 nm and (c) 80 nm. The insets are the histograms of length distribution of Co NWs. In the histogram, the x-axis and y-axis represent diameter and counts, respectively. (d) The corresponding M-H plots of the aligned Co NW assemblies in epoxy. (e) and (f) The length dependence of coercivity and $(BH)_{max}$ of Co NWs.

As we mentioned in section 1.2.2.3 Coercivity Mechanisms in Nanoparticles, the diameter of Co NWs is vital for the magnetic reversal mechanism as well as H_C. Accurate control of the diameter of the Co NWs has been achieved in this study. The concentration of HDA which is used as surfactant in the solvothermal reaction is tuned to control the diameter and thus manipulate the magnetic properties of Co NWs. When the mole ratio of Co precursor to HDA increases from 1:2

to 2:1, the Co NWs with diameter of 8 - 20 nm are obtained, respectively. All the Co NWs are very uniform shown by the representative TEM micrographs in Figure 4.3a-d.

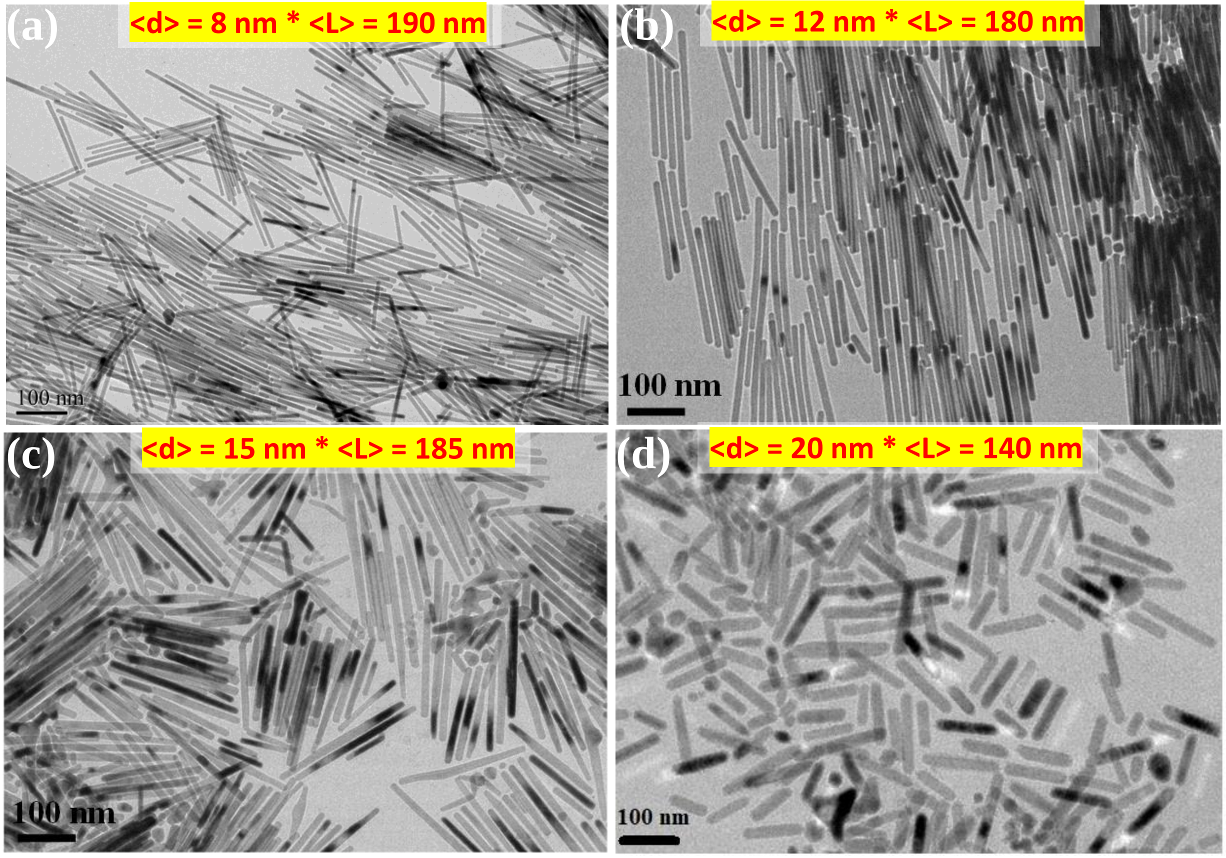

Figure 4.3 Co NWs with average diameter of (a) 8 nm, (b) 12 nm, (c) 15 nm and (d) 20 nm.

The uniform morphology of Co NWs leads the good squareness of hysteresis loop of Co NWs with various diameters (see Figure 4.4a). The M-H plots Figure 4.4b display as the diameter decreases from 20 to 8 nm, the coercivity for their aligned assemblies increases from 8 kOe to 13kOe. It is important to note that the aligned Co nanowire assemblies were prepared in epoxy resin with concentration of 5-20 wt. % Co. The coercivity of the Co nanowires assemblies remains unchanged with varying the nanowires concentration, which rules out the effect of dipolar interaction between the neighboring wires and the proximity effect in the studied system. The record high coercivity and good squareness of M-H loop result in the record $(BH)_{max}$ value up to 60 MGOe shown in Figure 4.4d. Energy product of 56 MGOe, 48 MGOe and 44 MGOe are achieved in Co NWs with diameter of 12 nm, 15 nm, and 20 nm, respectively (see Figure 4.4c). To be mentioned, the energy product of the aligned nanowires in Figure 4.4f is calculated based on the full volume fraction of tightly densified Co nanowires with the theoretical density of 8.92 g/cm^3. Although the potentially factors such as the packing factor, demagnetization, dipolar interactions, or exchange coupling can decrease the $(BH)_{max}$ value of a bulk magnet, which is not reflected in this result. The noticeable magnetic properties demonstrate the Co nanowires can be potentially ideal building blocks for high performance bonded magnets, densified magnets as well as thin film magnets with both isotropic and anisotropic magnetic structures.

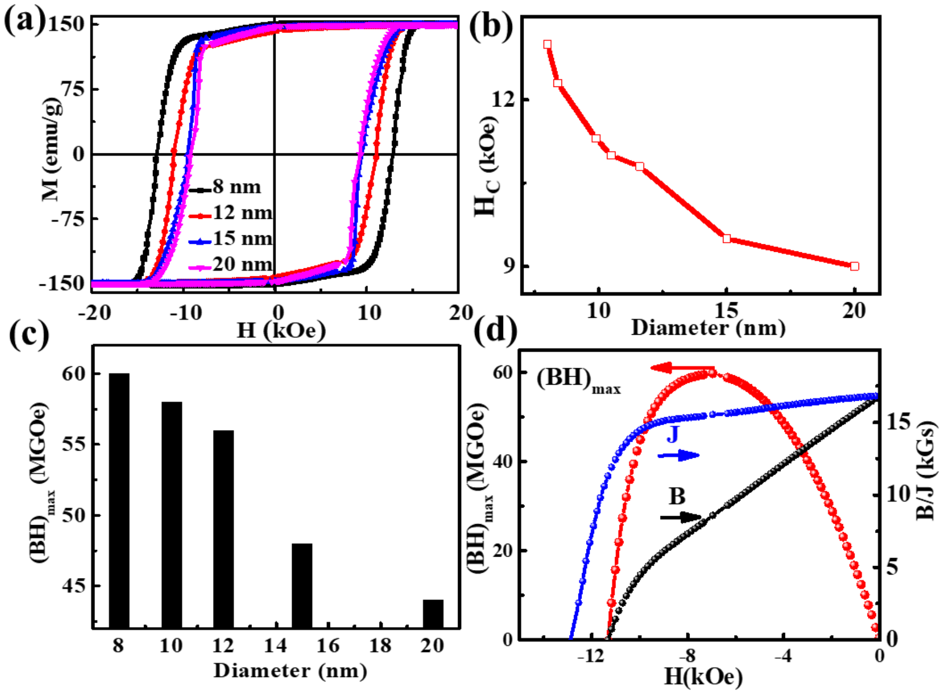

Figure 4.4 (a) M-H plots of Co NWs with diameter of 8 nm, 12 nm, 15 nm, and 20 nm at room temperature. (b) Diameter dependence of coercivity. (c) Maximum energy product with respect to diameter. (d) B-H, J-H and $(BH)_{max}$ curves of Co NWs with diameter of 8 nm at room temperature.

To characterize the temperature dependence of coercivity for the aligned Co NWs assembly, the M-H plots of Co NWs with varied diameter at different temperatures were measured. Figure 4.5a displays M-H plots of Co NWs with dimeter of 8 nm. The temperature dependence of coercivity for all the Co NWs was summarized in Figure 4.5b. With the decreasing temperature, the coercivity increased monotonously and reached a giant coercivity of 22.0 kOe at 10 K. The coercivity enhancement at low temperatures (below the Néel temperature) could be caused by exchange bias as a result of surface oxidation.[127] However in our case, the Co nanowire assemblies do not exhibit exchange bias behavior, which rules out the presence of CoO phase on the surface of nanowires. Thus, the coercivity enhancement is only related to the increase in magnetic anisotropy and the reduction of the thermal fluctuation with the decreasing temperature.

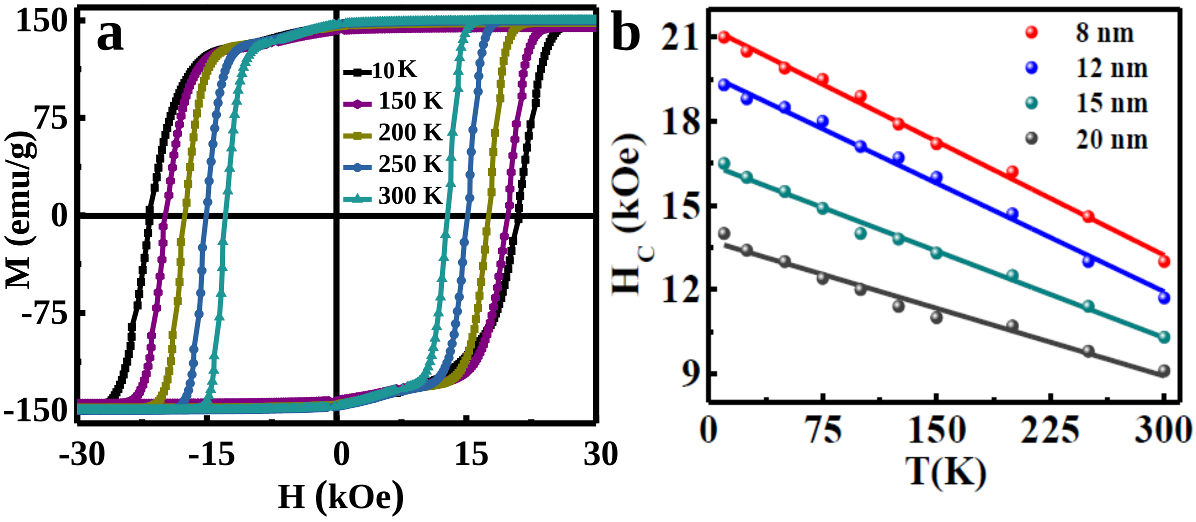

Figure 4.5 (a) The hysteresis loops of 8 nm Co NWs at different temperatures. The hysteresis loop was measured under field cooling (FC) in 50 kOe from 300 K to 10 K. (b) The temperature dependence of coercivity for Co NWs assembly with different diameters.

As demonstrated above, the record high coercivity in the fabricated Co nanowire assemblies is ascribed to the uniform morphology, the good alignment and the unoxidized surface of nanowires.

In addition, it is also due to perfect single-crystalline structures and easy axis orientation along the long axis of nanowires, as manifested by the high resolution TEM analysis in Figure 4.6a-c. The FFT and IFFT patterns shown in Figure 4.6b and c confirm the formation of hcp-Co phase and the distance between the lattice fringes is 0.205 nm, which is close to the (002) planes of hcp-Co. On the other hand, the record high coercivity in the fabricated Co nanowire assemblies originated from the single-domain structure of Co nanowire, as demonstrated by the magnetic holography analysis in Figure 4.6d-f. The phase shift value across the NW in the electron hologram shown in Figure 4.6e is calculated from the phase profile measured in the red line 1, 2 and 3 shown in Figure 4.6e to confirm the single-domain structure of the Co NW. Attributed to the internal magnetic field of nanowire, the relationship of the phase shift $\Delta\varphi$ and the internal magnetic flux density B is as follows:[128]

$$\Delta\varphi = 2\pi({}^{e}\!/_{h})BS \qquad 4.1$$

where e is the electron charge, h is the Plank’s constant, and S is the cross-sectional area of the nanowire. At the line 1, 2, and 3, $\Delta\varphi$ is nearly the same (0.23 rad, 0.25 rad and 0.26 rad) between the left and right side of the wire, which indicates that B is uniform in the nanowire and thus demonstrates that Co nanowire is in the single domain state. In addition, the magnetic flux lines are along the wire direction, validating the magnetization orientation along the long axis.

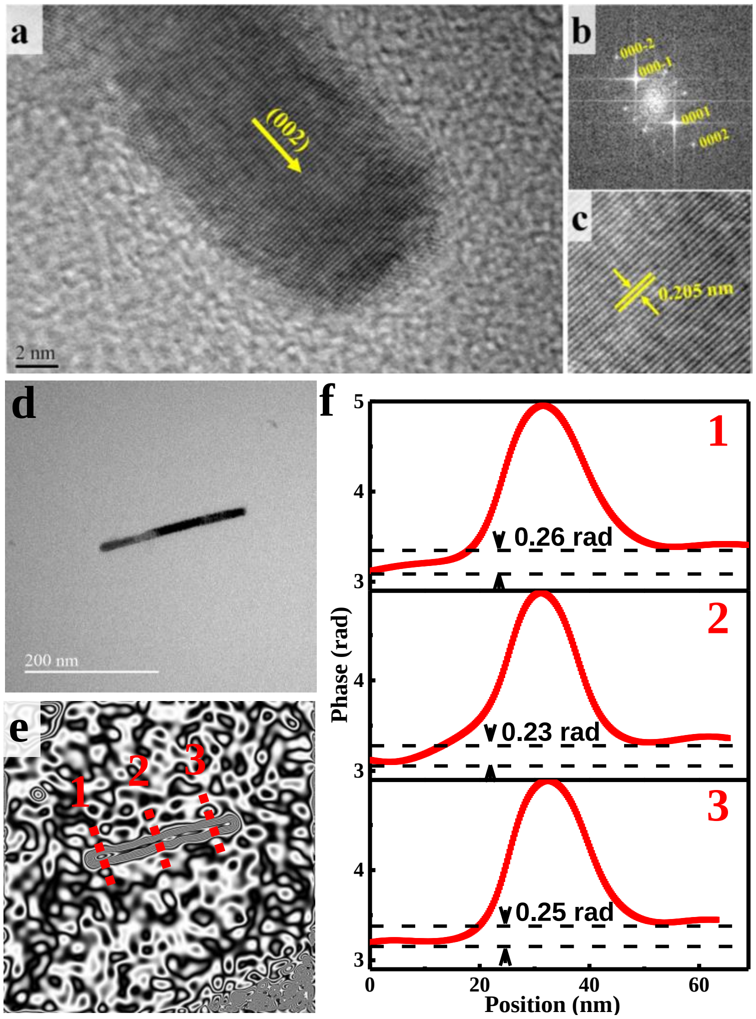

Figure 4.6 (a) High resolution TEM image of a single Co nanowire. (b) The Fast Fourier Transform (FFT) and (c) Inverse Fast Fourier Transform (IFFT) patterns of the crystalline region. (d) Bright-field TEM micrograph of a single Co nanowire with diameter 8 nm and (e) the amplified phase profile of electron hologram. (f) Phase profiles of Co NW for the cross-sectional area along lines 1−3 numbered in e.

As we mentioned before, the high coercivity values shown in Figure 4.4 was measured from the nanowires aligned in epoxy. The wires are diluted, so the magnetic interactions between the individual single-domain nanowires can be neglected and the magnetization reversal can occur via either coherent rotation mode or curling mode, depending on the thickness of the nanowire.[16] To understand the magnetization reversal phenomenon, angular dependent hysteresis loops were measured and compared with the analytical curves computed based on the Stoner-Wohlfarth (SW) model as shown in Figure 4.7a and b. For instance, the experimental magnetization loops with shapes are identical to those predicted by SW model have been found in 8 nm Co NWs sample, exceptionally, the experimental coercivity measured along the alignment direction for 8 nm Co NWs is nearly double that for the angle of 90°. In addition, the remanent magnetization of the aligned sample also increased greatly, leading to the remanent magnetization ratio M_R/M_S of 0.99. This doubling in coercivity and remanence ratio of 0.99 along the alignment direction is a typical Stoner-Wohlfarth coherent rotation-type behavior of a single-domain nanowire system.[129] Although the 20 nm Co NWs sample exhibits a similar enhancement in coercivity and M_R/M_S ratio, but the coercivity along the alignment direction is only 1.4 times of that for the angle 90º, which indicates that the coherent rotation has not been taking place in the 20 nm Co NWs. Typically, the coherent rotation reversal is only favorable for ultra-thin NWs when the wire diameter is smaller than $D_{coh} = 7.3 l_{ex}$, $l_{ex} \sim 2 nm$ for Co.[130] While the 15 and 20 nm Co NW samples contain NWs with diameters larger than the coherent limit (~ 14.6 nm), a curling reversal mode can be expected.[131, 132] Thus, for Co NWs with diameter up to 12 nm, the record coercivity is ascribed to the coherent rotation-type magnetization reversal.

To get further insight of the actual magnetization reversal processes versus diameter, the angular dependence of coercivity for the aligned Co NWs is compared with the theoretical coherent rotation and curling curves. Figure 4.7c illustrates the results for Co NWs with various diameters. As evidenced from the angular dependent coercivity plots, the coercivity value shows a gradual increase when the orientation of the magnetic field is shifted from 90° (hard-axis, i.e. normal to the NWs) to 0° or 180° (easy-axis, i.e. along the NWs). Moreover, a diameter effect on the coercivity variation can be seen in Figure 4.7d, the increasing rate of coercivity with the angle, when the field rotated from 90°, is found to be low in 20 nm Co NWs. More importantly, when the experimental coercivity values for NWs with different diameters are compared separately with the analytical coercivity curves (see Figure 4.7d), we have noticed that the experimental coercivity is well consistent with the analytical curve of SW coherent rotation for 8 nm Co NWs. In contrast, the experimental coercivity of 20 nm Co NWs follows the analytical curve of curling model and for the entire angle, the observed coercivity just lies below the theoretical values. The variation of coercivity in 12 nm and 15 nm sample do not fit to both the models, particularly the coercivity at angle 0° or 180° is higher than that estimated for the curling, which means that the magnetization reversal in 12 nm and 15 nm sample takes places by a complex contribution from both the coherent rotation and magnetization curling.

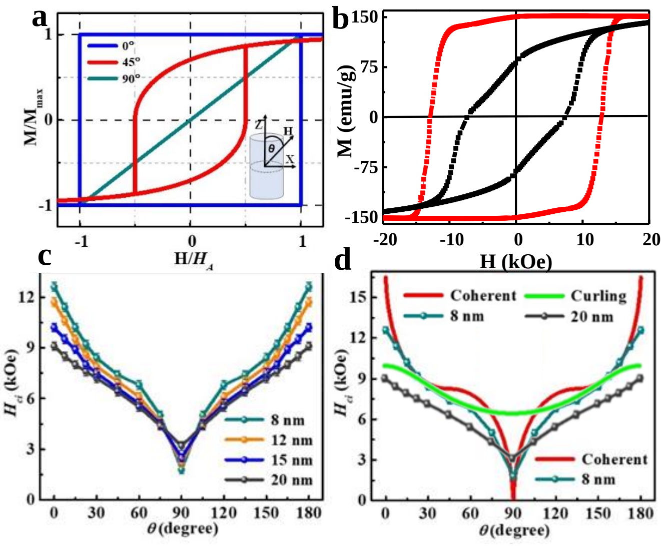

Figure 4.7 (a) Hysteresis loops predicted by the Stoner–Wohlfarth model for indicated angles between the magnetic field and easy axis (NW long axis). (b) Room temperature hysteresis loops

of aligned Co NWs measured at the mentioned angles with wire diameter 8 nm. (c) The angular dependence of the coercivity for different diameter Co NWs. (d) Comparison between experimental and analytical angular dependence of coercivity for NWs with diameter 8 nm and 20 nm, respectively. The red solid line and green line in (d) correspond to the analytical coercivity plots calculated by adapting Stoner-Wohlfarth model[133] (Coherent reversal) and Aharoni model[131] (Curling reversal), respectively.

4.4 Exchange Bias Effect of Co/CoO Core-Shell Nanowires

Figure 4.8a and b show the transmission electron microscopy (TEM) images of Co nanowires and Co/CoO core-shell nanowires with diameter of ~ 8 nm. The high resolution transmission electron microscopy (HRTEM) images (Figure 4.8c and d) of a nanowire reveal that the core is single crystalline with the c-axis (002) (the easy magnetization axis of hcp-cobalt) orienting along the long axis of the nanowire. Figure 4.8b displays a variation in contrast along the edge of the Co/CoO nanowire, which indicates the core-shell nanostructure. The thickness of the thin oxide shell is ~ 1.5 nm in Figure 4.8d. The oxide shell is continuous all over the nanowire edge. Moreover, it composed of randomly oriented small crystallites. The diffraction patterns on the edge and on the tip of the wire reveal that the oxide shell is with the fcc-CoO structure. The fringe distances of 0.212 nm and 0.245 nm correspond to the (002) and (111) plane reflections of the cubic CoO, respectively. As a result, we conclude that the core-shell structure consists of a metallic hcp-Co core and a 1-2 nm polycrystalline fcc-CoO shell.

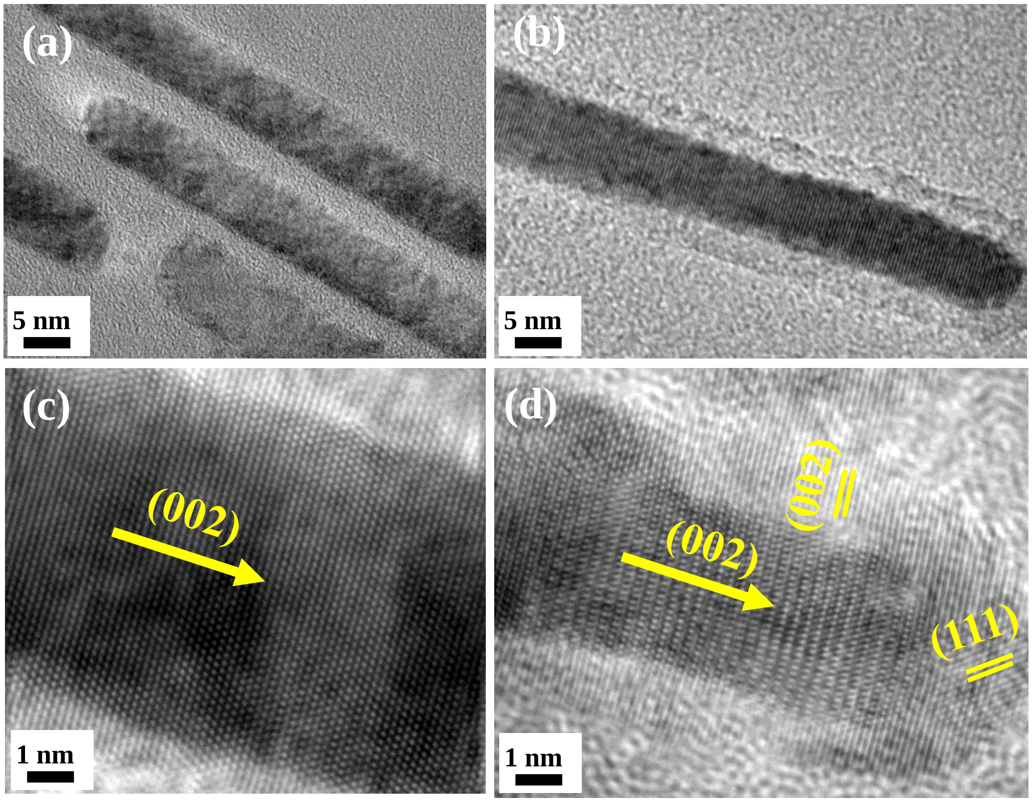

Figure 4.8 (a) and (b) TEM images of Co NWs and Co/CoO NWs. (c) and (d) HRTEM images of Co NWs and Co/CoO NWs.

In order to understand the effect of the surface oxide shell on the magnetic properties, the temperature dependent magnetic measurements were investigated. Figure 4.9a and b display the magnetic hysteresis loops measured at 300 K and 10 K with field cooling (FC) in 50 kOe from 300 K to 10 K for the aligned nanowire assemblies. The aligned sample was prepared by hardening Co and Co/CoO nanowires in epoxy resin which has been described in detail in section 4.2. For Co aligned nanowires, M-H curves at 300 K and 10 K are symmetric in Figure 4.9a. However, a robust shift opposite to the cooling field direction is found in FC M-H curve of Co/CoO nanowires at 10 K in Figure 4.9b, which indicates a FC-induced unidirectional magnetic anisotropy of Co/CoO nanowires.

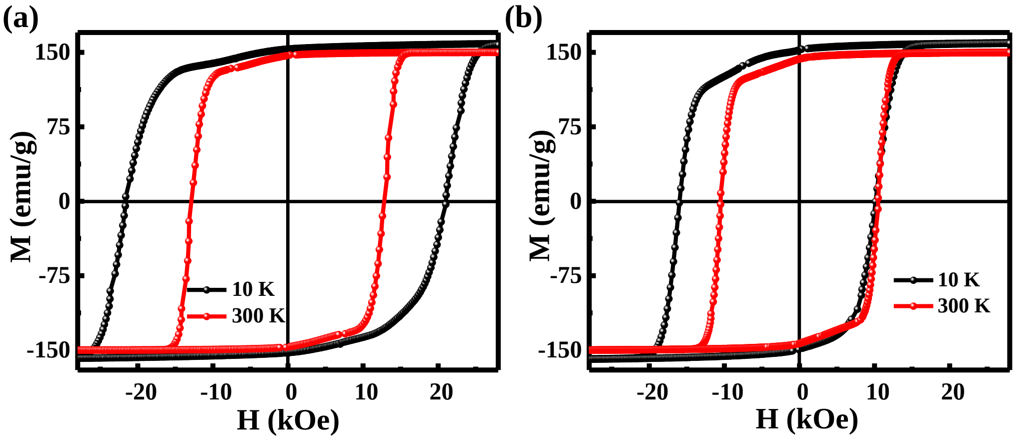

Figure 4.9 (a) and (b) M-H curves of the as-prepared Co NWs and Co NWs with thick CoO shell at room temperature (red curve) and 10 K (black curve), respectively.

To explore the EB effects and the temperature dependence of coercivity, the H_C and H_{EB} as a function of temperature are summarized in Figure 4.10. The coercive field values of the nanowires are shown in Figure 4.10a. The coercivity is defined by $H_C = (H_{C2} - H_{C1})/2$, where H_{C1} and H_{C2} are the left and right coercive fields, respectively. For as-prepared Co NWs, the H_C monotonously decreases from 22 kOe to 13 kOe with the increased temperature. However, it can be observed that the temperature dependence of coercivity in Co/CoO core-shell nanowires is non-monotonous and has noticeable oscillatory behavior. In Co nanowires with thick CoO shell (Figure 4.10a blue curve), initially, H_C decreases to a minimum at 60 K, then rises to a maximum at 150 K, and finally decreases again up to 300 K. The most important feature is the increase in the coercive field to a maximum value of 15.2 kOe at 150 K. Such temperature dependence oscillatory behavior of coercivity is uncommon and is not observed in unidirectional 0D Co/CoO nanoparticles and 2D Co/CoO bilayers systems.[118, 134] The peak value of H_C at 150 K reveals the Néel temperature T_N = 150 K, which is below the bulk T_N of CoO (293 K) caused by the finite size effect of AFM grains in a ~ 1.5 nm thick CoO shell.[135] The reduced H_C above T_N is due to the decrease in the magnetocrystalline anisotropy of hcp-Co with the increased temperature. Maurer et al. explained that the minimum in H_C at 60 K is due to blocked AFM moments located to the tips of the nanowire which act as nucleation points and promote the magnetization reversal of the wires.[121] Below 60 K, the disordered interfacial spins become freezing and thus more effective interface layer forms, which leads the improved exchange anisotropy.[122] Therefore, the enhanced H_C appears. By careful observation it can also be seen that, with the increased thickness of CoO shell, the “pit” in the coercivity curve is increasingly deep seeing the red arrow in Figure 4.10a. This indicates there are more and more small CoO crystallites on the tip of nanowire with the increased CoO shell thickness. The H_{EB} with respect to temperature for Co/CoO samples is shown in Figure 4.10b. The EB effect robustly depends on temperature, vanishing above the so-called blocking temperature (T_{EB} = 100 K). The exchange-bias field is defined by $H_{EB} = -(H_{C2}+ H_{C1})/2$, where H_{C1} and H_{C2} represent the left and right coercive fields. With the increase of CoO shell thickness, exchange bias field enhances, which should be due to the increased FM/AFM interface layer. The H_{EB} for the Co NWs with thick CoO shell reaches 3.0 kOe at 10 K.

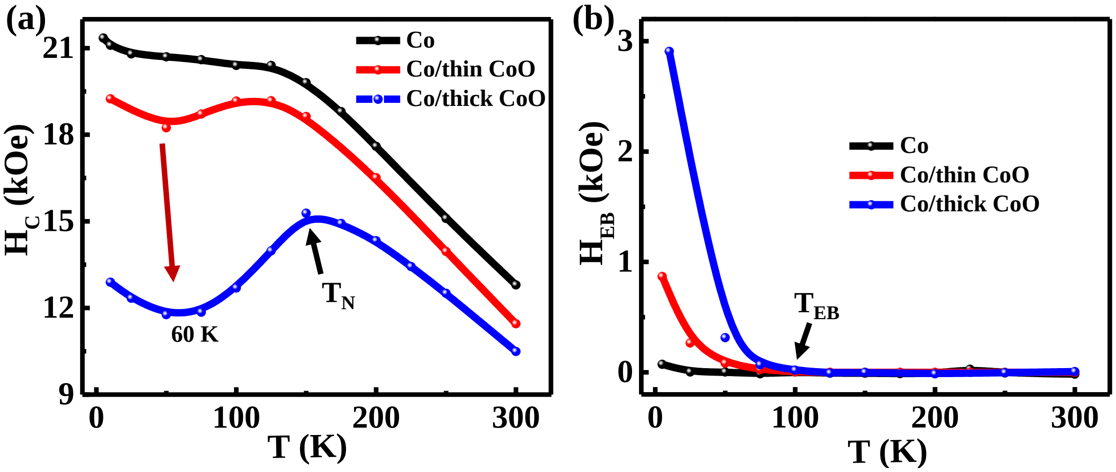

Figure 4.10 (a) Temperature dependence of coercivity of the as-prepared Co NWs (black curve), Co NWs with thin CoO shell (red curve), and Co NWs with thick CoO shell (blue curve). (b)

Temperature dependence of exchange bias effect of the as-prepared Co NWs (black curve), Co NWs with thin CoO shell (red curve), and Co NWs with thick CoO shell (blue curve).

4.5 Conclusion

A series of Co nanowires with controlled geometry have been fabricated, achieving extremely high coercivity (13.0 kOe) and record energy product (60 MGOe). The prominent magnetic performance is attributed to the successful control of the diameters, crystallinity, and domain structure. The correlations between the coercivity and the diameter are studied by experimental and analytical analysis. The angular dependence of coercivity has been experimentally investigated for the aligned Co NW assemblies. According to an analytical simulation based on the Stoner-Wohlfarth model, for 8 nm Co NWs, the magnetization reversal mode is demonstrated to be a coherent reversal mode. However, it is curling reversal mode for 20 nm Co NWs revealed by the analytical simulation based on Aharoni model. Ascribed to the enhanced magnetocrystalline anisotropy with the decreasing temperature, the coercivity monotonously increases in as-prepared Co MWs. However, it is oscillatory in Co/CoO NWs. The drop of coercivity in the temperature ranging from 150 to 60 K is due to the interaction between the spin ordered AFM grains and the demagnetizing field, which is a unique property of 1-D core-shell nanowire system. With the increased CoO shell thickness, the drop of coercivity at low temperatures becomes more and more prominent resulted from the increased amount of CoO grains on the tip of Co NWs.

Chapter 5 Proximity Effects in Densified Random and Aligned Co Nanowire Assemblies

5.1 Introduction

Magnetic nanowires attracted intensive interest both scientifically and for practical applications in the modern nanotechnology such as magnetic memories,[136] magnetic recording media,[137] sensors,[138] or microwave devices.[139] The prominent magnetic properties of nanowires are mainly dominated by the very strong shape anisotropy yielding high coercive fields which have applications for permanent magnets fabrication. In chapter 4, we have demonstrated that after alignment a record high coercivity of 13.0 kOe was obtained in the single crystalline and single domain Co NW assemblies. The above studies are mainly focused on the low-density NW assemblies, in which the effective magnetostastic interactions among the NWs are negligible. Note that the magnetostastic interactions may have a strong influence on the macroscopic magnetic behavior of the NW assembly and consequently on the coercivity, which has not been thoroughly investigated in experiments. Therefore, it is interesting to understand the coercivity variation with the packing fraction in order to design high performance magnets for the future applications. According to the theoretical investigation, the coercive filed decreases with packing fraction and thus a maximum energy product can be achieved at an intermediate packing fraction.[110,12] In this chapter, the effects of packing density on the coercivity of the random Co NW assemblies and aligned Co NWs assemblies are investigated.

5.2 Fabrication of Densified Random and Aligned Cobalt Nanowire Assemblies

The single crystalline and single domain Co NWs with varied diameter were used to fabricated densified random and aligned Co nanowire assemblies. Prior to the compaction, randomly oriented and aligned Co nanowire assemblies were prepared via evaporating the chloroform dispersion of the Co NWs (20 mg/ml) on copper foil without and with the external magnetic field of 2.0 T generated by an electro-magnet, respectively. For the densified random Co NWs assemblies, the dry powder of Co NWs was compacted using a uniaxial hydraulic press. For the random Co NWs assemblies, the applied pressure was varied as 100 MPa, 200 MPa, 300 MPa, 400 MPa and 500 MPa to get compacted Co NWs assemblies with different packing density as 2 g/cm^3, 3.8 g/cm^3, 4.36 g/cm^3, 5.2 g/cm^3 and 6.0 g/cm^3, respectively. The densified aligned Co NWs assemblies were prepared by the flowing procedure. The dry Co NWs were grinded using a mortar and then compacted in the 2 T magnetic field using a uniaxial hydraulic press with pressure varying from 14 MPa to 34 MPa. A Hitachi S-4800 II Field emission scanning electron microscopy (FE-SEM) were used to record the scanning electron microscope (SEM) micrographs of randomly oriented and aligned Co nanowire assemblies.

5.3 Magnetic Hardening in the Densified Random Cobalt Nanowire Assemblies

Although the high coercivity in Co NWs is a very strong evidence for the formation of the hcp-Co phase, XRD measurement was performed to examine the phase of as-prepared Co NWs before and after the compaction. Both the XRD patterns, shown in Figure 5.1a, exhibit five prominent diffraction peaks for (100), (002), (101), (102) and (110) planes of hcp-structured Co. These peaks match well with the standard diffraction peaks of hcp-Co with ICDD card No. 01-089-4308. Top view SEM micrographes of the compacted Co NW assemblies with density of 4.45 g/cm^3 and 6.0 g/cm^3 in Figure 5.1b and c confirm that the Co NWs were closely packed together and the morphology maintained even at high pressure of 500 MPa. Moreover, with increasing density, the NWs approached to each other more and more intimately, which will result in more prominent proximity effects.

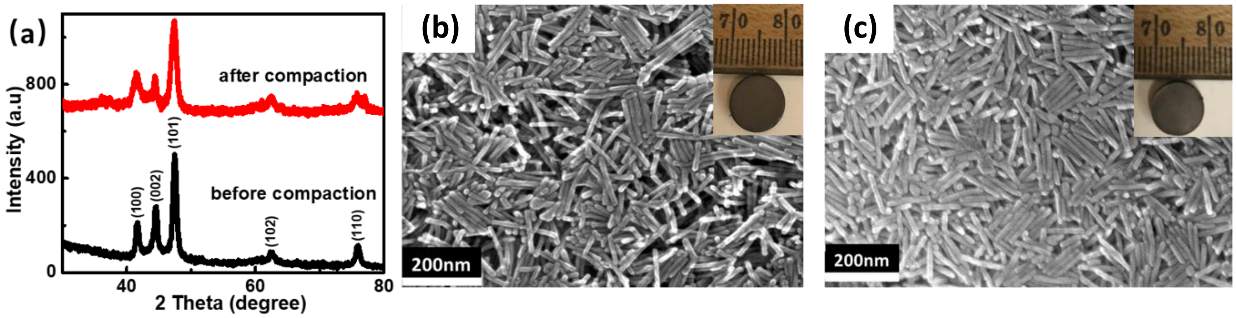

Figure 5.1 (a) XRD pattern of random Co NWs before and after compaction. (b) and (c) Top view SEM micrographs of the compacted Co NWs assemblies with density of 4.45 g/cm^3 and 6.0 g/cm^3, respectively. The inserts in (c) and (d) are digital photographs of the corresponding pellets of Co NWs assemblies. (All the Co NWs with diameter of 12 nm)

The magnetic properties of as-prepared Co NWs are measured at room temperature prior to the compaction. The obtained H_C values for the Co NWs of diameter 12 nm, 15 nm and 20 nm are 5.5, 5.3 and 4.9 kOe, respectively. The significant coercivity nearly 73 % of the anisotropy field of bulk Co material (7.6 kOe) is attributed to the coupling of magnetocrystalline anisotropy and shape anisotropy.[9] The high coercivity Co NWs were compacted to Co NW assemblies with different packing density (2.0 g/cm^3 to 6.0 g/cm^3) and their magnetic properties were studied as shown in Figure 5.2. Interestingly, the at room temperature increases from 5.5 kOe to 6.1 kOe with the increase in packing density from 2.0 g/cm^3 to 4.5 g/cm^3. A similar trend in the H_C value has also been found at different temperatures as shown in Figure 5.2a. Moreover, the remanence (M_R) increased from 72.0 emu/g to 82.5 emu/g with the increased packing density. The initial increase in H_C and M_R values may be due to the enhanced magnetostatic interactions between the nanowires upon densification. However, when the density is higher than 4.5 g/cm^3, the H_C decreases.

To further understand the coercivity dependence of density, we also investigated the effect of NW diameter on the H_C value. Co NW assemblies made up of Co NWs with larger diameters of 15 nm and 20 nm were prepared. When the diameter increases from 12 nm to 15 nm, there is only an unnoticeable increase of H_C, followed by a sharp decrease with increasing packing density as shown in Figure 5.2b. When the diameter increases to 20 nm, a monotonous decrease of H_C is obtained in the whole studied region, as shown in Figure 5.2b.

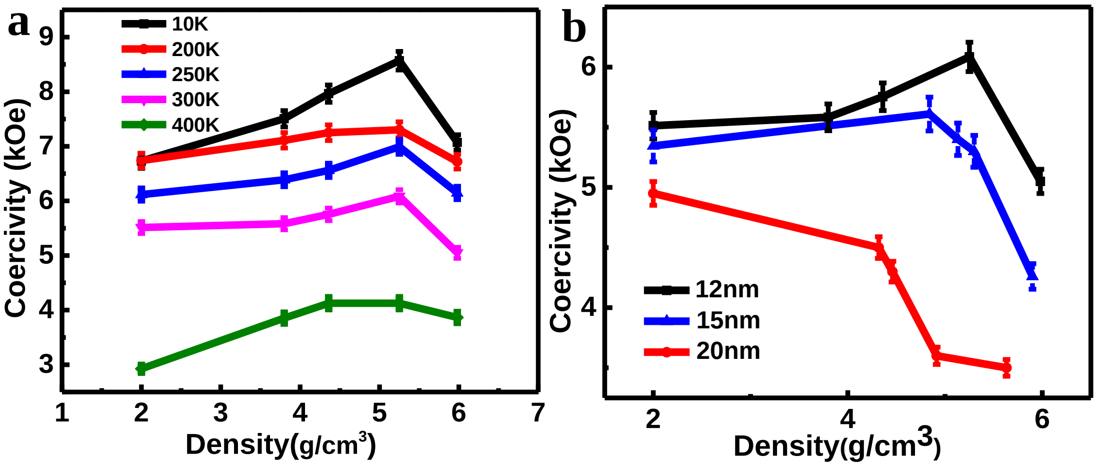

Figure 5.2 (a) Packing density dependence of coercivity at different temperatures for Co NW assembly (Co NWs with diameter of 12 nm). (b) The coercivity vs. packing density of random Co NWs with different diameters at room temperature.

To understand the H_C dependence on packing density as well as the diameter effect, the δM plots were measured for the compacted samples of the NWs with diameter of 12 nm. The δM plots in Figure 5.3 show that the negative peak becomes more and more prominent at high fields with increasing packing density. The negative peaks are the sign for strong dipolar interactions between the adjacent Co NWs.[110, 140] The proximity effect as it shows reduces the coercivity. Taking the diameter effects into account, it may be related to the fact that a larger diameter could lead to a decrease in H_C upon the increased packing density that in turn reduces the dipolar interactions. Nevertheless, the mechanism for the diameter effect still needs to be further investigated.

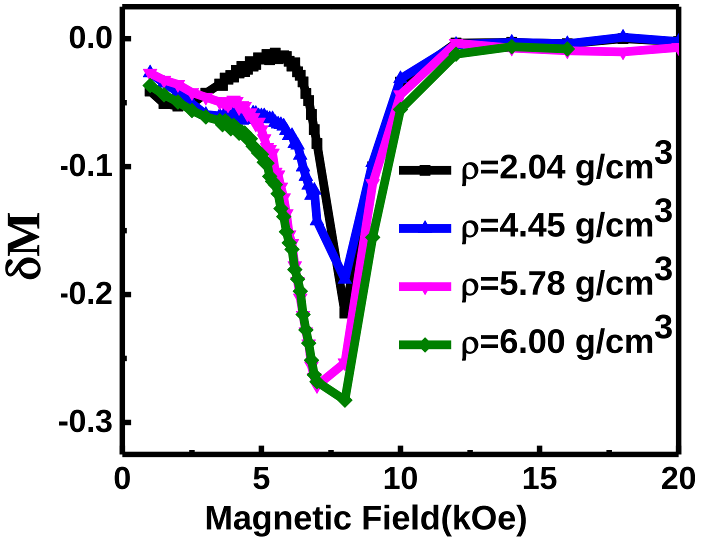

Figure 5.3 Delta M plots of Co NW assemblies with varied packing density (Co NWs with diameter of 12 nm).

5.4 Magnetic Hardening in the Densified Aligned Cobalt Nanowire Assemblies

Our group has been exploring the creation of permanent magnets based solely on shape anisotropy from last decade.[67, 78, 141, 142] However, the coercivity is an important issue in the case of samples with high packing fractions.[110] In section 5.3, we have demonstrated a coercivity decrease effect in randomly oriented Co NW assemblies.[143] It is understandable that when the ferromagnetic nanowires get close to each other, magnetic interactions take place, which reduces coercivity and the phenomenon is called the proximity effect. In order to assess the proximity effect on the coercivity, the compacted Co NW assemblies were prepared by compacting pre-aligned Co nanowires under the magnetic field without adding any binding materials, as schematically illustrated in the Figure 5.4a. The compaction conditions are given in Table 5.1.

Table 5.1 Experimental compaction conditions and magnetic properties of the compacted assemblies.

NWs diameter	Pressure (MPa)	Density (g/cm^3)	Coercivity (kOe)	$(BH)_{max}$ (MGOe)
8 nm	**14**	**4.2**	**10.2**	**14.1**
	21	**4.8**	**9.3**	**16.4**
	28	**5.4**	**8.6**	**14.2**
	34	**5.7**	**7.7**	**13.4**
10 nm	**14**	**4.3**	**10.1**	**19**
	21	**4.9**	**9.2**	**17.3**
	28	**5.5**	**8.6**	**15.4**
	30	**6.0**	**7.6**	**13.7**
12 nm	**14**	**4.7**	**9.6**	**20**
	21	**5.1**	**9.2**	**19**
	28	**6.0**	**8.4**	**15.7**
	30	**6.1**	**8.2**	**13.8**
15 nm	**14**	**4.9**	**8.5**	**17.1**
	21	**5.7**	**8.1**	**14.4**

	28	**6.3**	**7.9**	**12.1**
	30	**6.3**	**7.7**	**11.5**
20 nm	**14**	**4.9**	**7.6**	**10**
	21	**5.6**	**7.3**	**8.6**
	28	**6.5**	**6.8**	**7.4**

Interestingly, the compacted assemblies maintain the Co NWs morphology and alignment even after being compacted up to the packing fraction of 0.74, as confirmed by the SEM micrographs, XRD analysis, and magnetic measurements shown in Figure 5.4b-g. The XRD patterns clearly demonstrate a single diffraction peak, (002) orientation, i.e. the c-axis which is parallel to the magnetic field direction (see Figure 5.4f). Besides, the compacted NW assembly exhibits a nearly rectangle-shaped hysteresis loop with a remanent magnetization to saturation magnetization ratio (M_R/M_S) of 0.96 and the enhanced coercivity of 10.5 kOe at room-temperature, as shown in Figure 5.4g. While, when the field was applied perpendicular to the wire axis, a sheared hysteresis loop with a very small coercivity of 2.4 kOe is obtained. A compacted NWs assembly of this type, which upholds the shape anisotropy and texture, is critically important for developing a new type nanowire-based magnet in the future.

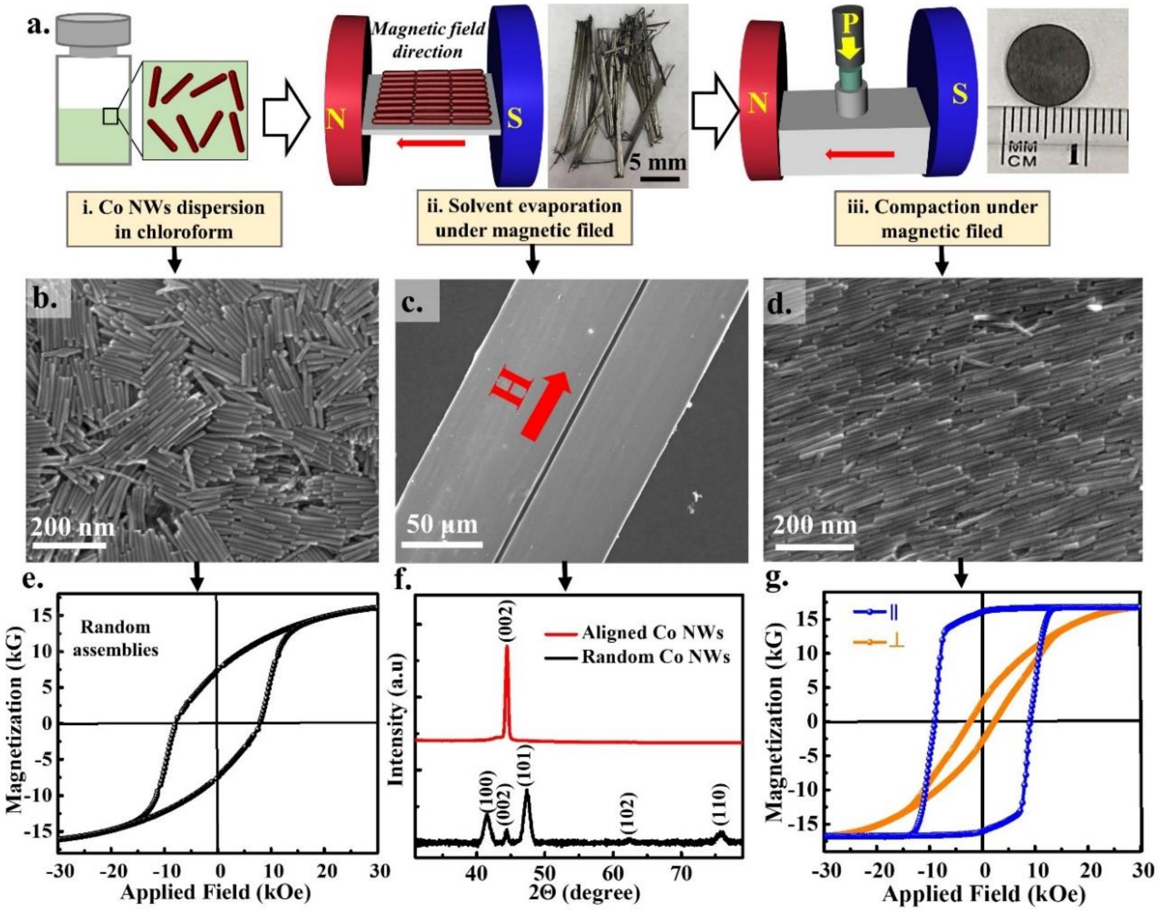

Figure 5.4 Fabrication procedure, structural and magnetic properties of compacted nanowire assembly, where the diameter of the Co nanowires is 12 nm. (a) Schematic illustration of the experimental setups for preparation of compacted aligned nanowires assembly: (i) formulation of NWs dispersion in chloroform, (ii) development of aligned assembly by the magnetic-field-assisted assembly of the nanowires and (iii) compaction of the dry NWs assemblies. SEM micrograph of: (b) randomly oriented NWs assembly, (c) millimeter size aligned NWs assembly and (d) compacted aligned NWs assembly. (e) Magnetization loop of a randomly oriented NWs assembly at 300 K. (f) XRD patterns of the NWs in random orientation and compacted assembly

in the alignment direction. (g) Room temperature magnetization loops along the parallel and perpendicular directions of the alignment.

A series of aligned Co NW assemblies with different packing fractions and wire diameters has been prepared, and their obtained microstructural and magnetic properties are displayed in Figure 5.5a-d. As a rule, in the case of compacted bulk sample, the saturation magnetization is simply proportional to the density, thus it increases linearly for the Co NWs assemblies with the increase of packing fraction as shown in Figure 5.5a. However, as explained above, there is always a major concern on coercivity, particularly for compacted NWs assemblies, as the coercivity is strongly affected by proximity effect induced by local stray fields and macroscopic demagnetizing field.[144, 145] In addition, a significant loss of coercivity could also be possible due to the misorientation of NWs with respect to each other. To quantify the proximity effect and to understand the problem of interplay between the coercivity and packing fraction, the packing fraction dependence coercivity plot for different diameter Co NWs is fitted with a modified formula as shown in Figure 5.5b. According to the formula, the relationship between coercivity and packing fraction can be described by[66]

$$H_C(p) = H_{CO} - A_1 p \tag{5.1}$$

where p is the packing fraction, H_{CO} stands for the effective anisotropy field (sum of shape anisotropy and magnetocrystalline anisotropy fields) and the fitting parameter A_1 indicates a reduction rate of the coercivity. A linear decrease in coercivity with packing fraction is always expected for single domain nanowires due to the proximity effect.[66] In our case, the compacted assemblies of Co NWs with diameter 20 nm and 15 nm show a linear decrease in coercivity values with the increase of packing fraction. Since the nanowire misalignment has been removed by the

SEM analysis (see Figure 5.5e), the coercivity decrease, in this case, can be solely ascribed to the proximity effect. As explained above, the coercivity decrease is then ascribed to the decrease of magnetostatic energy in the spaces among nanowires as these spaces get smaller after the compaction.[146] It is important to mention here that the reduction rate parameter A_1 for both the samples (15 nm and 20 nm) is nearly same (~3.34 kOe) and the estimated coercivity values for the hexagonal closed-packed assembly (theoretical packing fraction 0.91) of the corresponding nanowires are 7.4 and 6.4 kOe, respectively.

While the compacted assemblies of Co NWs with diameter 8-15 nm reveal a deviation from the linear trend, particularly above the packing fraction 0.54. The nonlinear dependence of the coercivity on the packing fraction for an assembly of nanowires is a complicated issue as both the proximity effect and misalignments are involved. To explain the nonlinear dependence of coercivity, the coercivity plots are fitted with the quadratic formula,

$$H_C(p) = H_{CO} - A_1 p - A_1 p^2 \qquad 5.2$$

where the fitting parameters A_1 and A_2 indicate reduction of the coercivity due to proximity effect and the misalignment effect, respectively. Especially, the fitting parameter, A_2, related to the misalignment effect increased from 0.4 kOe to 1.2 kOe with a decrease of the NW diameter from 12 nm to 8 nm. The quality of misalignment in these samples can be assessed by the remanence to saturation ratio M_R/M_S as the squareness of the hysteresis loop is related to the distribution of the easy-axis orientation with respect to the applied field. The M_R/M_S ratio of compacted assembly of 8 nm nanowires decreased from 0.98 to 0.86 and the corresponding misalignment angle increased from 10° to 30°. The combined effects of the misalignment and the proximity effect result in a quadratic decrease in the coercivity value with the packing fraction. The influence of the NWs diameter on the packing fraction is also observed by the density values measured by pycnometry. The maximum packing fraction obtained for the compacted samples increased from about 0.65 to 0.74 for rod diameter varying from 8 nm to 20 nm. Importantly, we have almost reached the limit of packing fraction that can be attained in the surfactant coated nanowires. The relative increase of density and M_R/M_S ratio with the increased diameter of NWs is expected for the compacted samples because the NWs with thinner diameter always exhibit high specific surface area with higher loading of organic ligands. Qualitatively the results show a strong coercivity dependence on packing fraction and especially, the proximity and misalignment effects are prominent with the diameter and lead to a low coercivity.

The control exercised over both the diameter of Co NWs and compaction condition enable to achieve high energy product, $(BH)_{max}$, of 20 MGOe, as shown in Figure 5.5c and d. More importantly, as expected, the $(BH)_{max}$ values for the compacted NWs assemblies increased to the maximum value with increase of the packing fraction and then decrease as the compacted assembly with higher packing fraction exhibited low coercivity and remanent magnetization. The energy product reached by the compaction of NWs of different diameter is nearly two times higher than that of the commercial Alnico magnets, which are also based on the shape anisotropy of Fe-Co needles.[147] Among all the compacted samples of different NWs diameters, the samples composed of 10 nm (~ 19 MGOe) and 12 nm (~20 MGOe) Co NWs exhibited record high $(BH)_{max}$ value, thanks to their high magnetic coercivity and M_R values. Besides the high $(BH)_{max}$ values, the Co NWs-based magnets possess more than four times the coercivity of the anisotropic grade Alnico magnets, thus they can be used for advanced applications. In addition, the high coercivity Co NWs can be used to further improve the energy product via exchanged-coupled with high saturation magnetization Fe or FeCo alloys. Thus, our sophisticated Co NWs production and compaction techniques not only develops a new magnet with high energy product but also opens a potential direction to increase the energy product by increasing the remanence magnetization.

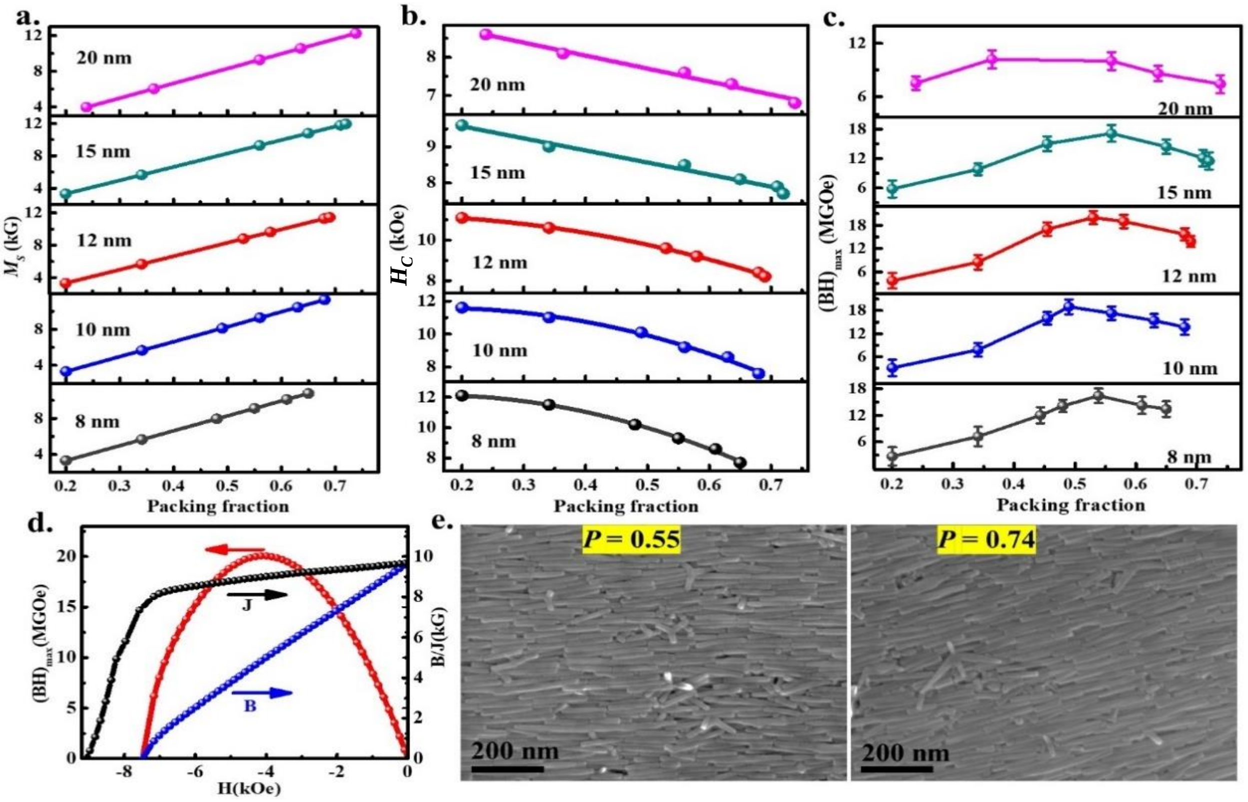

Figure 5.5 Effect of proximity on the coercivity and performance of compacted nanowires assemblies of different wire diameters. (a-c) Dependence of saturation magnetization (M_S), coercivity (H_C) and $(BH)_{max}$ on the packing fraction of compacted assemblies. (d) Second quadrant B-H, J-H and (BH)-H curves at 300 K for the compacted Co NWs assembly of wire diameter 12 nm. (e) SEM micrographs of the compacted Co NWs assembly with packing fraction $p = 0.55$ and $p = 0.74$, respectively.

5.5 Conclusion

We have shown that the magnetic properties of Co NW assemblies are strongly dependent on the packing density and diameter of the NWs. The Co NWs with average diameter 12 nm show an enhancement of coercivity with increasing packing density up to 4.5 g/cm^3. The H_C decreases with the further increase of the packing density due to proximity effects. In contrast, a sample with larger NW diameter, 20 nm, exhibit a trend of decreased H_C with increasing density, likely due to the proximity effects. Moreover, the high coercivity allows the compaction of pre-aligned Co nanowires to bulk magnets with energy product as high as 20 MGOe, higher than that of the of anisotropic cast Alnico grades commercially available. This finding is very interesting and useful for producing magnetic nanowire assemblies with controllable properties and to develop NW-based permanent magnets for future applications.

Chapter 6 Magnetic Hardening and Exchange Bias in Iron Carbide Nanoparticles

6.1 Introduction

Iron carbide are interstitial compound where carbon atoms are introduced to the interstices between close-packed iron atoms.[148] Iron carbide family consists of Fe_2C, Fe_7C_3, Fe_5C_2, and Fe_3C compounds.[149] The introduction of carbon atoms to Fe lattice results in the high chemical stability, unique catalytic properties, biocompatibility and unique magnetic properties to iron carbide. As a result, iron carbide has divergent applications such as contrast agent in magnetic resonance imaging, carrier for drug delivery, magnetic recording material, magnetic hyperthermia agent and catalyst.[149-152] Despite the fact that iron carbide compound is amongst the oldest materials known to mankind and are used widely, the physical understanding of the formation and the tune of the nanocrystal phase, size, morphology and composition of iron carbide phases are still in a premature state.[152-155] The robust wet chemical method provides the capability to synthesize the low dimensional iron carbide nanoparticles (NPs). Amsarajan *et al.* prepared the Fe_3C nanorods and revealed the contribution of shape anisotropy to the anisotropy field yielding the prominent coercivity at low temperature.[156] Compared to the other iron carbides, Fe_5C_2 have the highest saturation magnetization (M_S=140 emu/g).[157] Moreover, Fe_5C_2 is a robust, novel and effective catalysts in Fischer-Tropsch process as well as a bactericidal material.[158, 159] It is significant and valuable to investigate the morphology effects on the magnetic performance and the other related properties of Fe_5C_2 nanocrystals. However, the morphology control of Fe_5C_2 nanocrystals has not been achieved.

In addition, due to the carbon penetration growth mechanism of iron carbide, the reactants usually result in the core-shell structure. The core-shell interface constructs the multifunctional interface with reduction, catalysis, corrosion resistance, and immobilization capabilities. As a result, iron carbide/iron oxide core-shell structure has attracted an intensive research interest. Fe_5C_2/Fe_3O_4 and Fe_3O_4/Fe_5C_2 have shown a great potential in cancer therapy and an efficient catalytic properties in Fischer−Tropsch synthesis, respectively.[160, 161] $Fe_3C/Fe_3O_4/C$, Fe_3C/Fe_3O_4, Fe_3O_4/Fe_3C and $Fe/Fe_3C/Fe_3O_4$ have been developed and displayed the efficient dye adsorption, effective electromagnetic wave absorption, the efficient lithium ion storage and great supercapacitor properties, respectively.[162-167] When there is Fe_3O_4 shell, it is necessary to mention Verwey transition. Verwey transition of Fe_3O_4 is known that below 125 K, the cubic crystal is distorted to monoclinic crystal. The appearance of Verwey transition is the symbol of the good crystallinity of Fe_3O_4. Usually, Verwey transition has the scale (size) effects and gets suppressed in the nanocrystals smaller than 25 nm attributed to the missing coordinated oxygen atoms and the spin disorder of the surface.[168] FeO/Fe_3O_4 core/shell nanoparticles with spherical shape and anisotropic shape displayed the exchange bias.[169, 170,20] The anisotropic shaped FeO/Fe_3O_4 nanocrystals show larger exchange bias and an enhanced exchange bias is induced across the Verwey transition of Fe_3O_4 shell attributed to the magnetocrystalline anisotropy change accompanying the crystal structure transition. In addition, via controlling the core-shell dimensions, the magnetic anisotropy, which plays a crucial role in magnetic properties, can be controlled.[171-173]

Here, we successfully realized the morphology control of Fe_5C_2 and Fe_5C_2/Fe_3O_4 core-shell nanoparticles. The rod-shaped morphology generates the shape anisotropy resulting in a larger coercivity. The good crystallinity of the ultrathin Fe_3O_4 shell yields the Verwey transition which induces the exchange bias which is more prominent in Fe_5C_2/Fe_3O_4 nanorods. This paper promotes the further study of Fe_5C_2 in applications such as hyperthermia and photo thermal therapy.

6.2 Synthesis and Characterization of Monodispersed Iron Carbide Nanoparticles

Fe_5C_2/Fe_3O_4 core-shell nanoparticles of spherical and rod-shaped morphology were prepared using long-chain amine as solvent, reducing and surface functionalizing agents, with some modifications of a previously reported protocol.[174] In a typical synthesis of 13.2 nm spherical-shaped iron carbide nanoparticles (SNPs), 13 g (54 mmol) octadecylamine (ODA) and 0.226 g (0.6 mmol) cetrimonium bromide (CTAB) were taken in a European style three-neck round bottom flask. The reaction mixture was heated to 130 °C at 10 °C/min and kept at 130 °C for 10 min with the continuous flow of the forming gas. 0.3 ml (2.2 mmol) of iron pentacarbonyl ($Fe(CO)_5$) was injected by a syringe to the flask at 130 °C. Then, the temperature was elevated to 190 °C with the heating rate of 10 °C/min and stayed there for 10 min. Finally, the mixture was refluxed to 300 °C at 10 °C/min and aged for 1 h. The obtained black colored precipitate was collected and washed several times with toluene. When iron pentacarbonyl ($Fe(CO)_5$) was 3.2 mmol, 2.7 mmol and 1.7 mmol, iron carbide SNPs with diameter of 18.4 nm, 15.1 nm and 9.8 nm were obtained. In order to prepare rod-shaped nanoparticles (RNPs), ODA was replaced with hexadecylamine (HDA) and dodecylamine (DDA).

The microstructure analysis of the Fe_5C_2/Fe_3O_4 core-shell morphology was performed using Hitachi H-9500 High-resolution transmission electron (HR-TEM) microscopy operated at an accelerated voltage of 300 kV. The particle size was calculated using DigitalMicrograph software from Gatan Inc. The particle size distribution histograms were fitted with the appropriate Log-normal distribution functions. Rigaku Ultima IV diffractometer with Cu Kα wavelength (1.5406 Å) X-ray source was used to collect the powder X-ray diffraction (XRD) spectra and characterize the crystal structure of the prepared samples. The magnetic properties of the samples were studied using a physical property measurement system. The zero-field-cooled (ZFC) and field-cooled (FC) magnetization curves were measured over the temperature range 10–400 K under an applied magnetic field of 50 Oe. The hysteresis loops were measured at various temperatures after FC from 300 K under an applied magnetic field of 50 kOe. The shift of the hysteresis loop is quantified as $H_{EB} = -(H_{C2} + H_{C1})/2$, where H_{C1} and H_{C2} the fields at which the magnetization equals zero for decreasing and increasing branch of the loop, respectively. To confirm the oxidation state of Fe in the prepared samples, room temperature 57Fe Mössbauer spectroscopy was measured. The Mössbauer spectrometer (SEE Co. Minneapolis, MN USA) was calibrated against the α-Fe foil.

6.3 Magnetic Properties of Iron Carbide Spherical Nanoparticles

XRD patterns carried out on the as-synthesized iron carbide nanoparticles are shown in Figure 6.1. All the diffraction peaks are indexed to the Fe_5C_2 phase with monoclinic crystal structure (ICDD 051-0997). To be mentioned, there is one small peak labeled by the blue circle other than the peaks of Fe_5C_2 phase. This peak matches with the standard peak of magnetite (Fe_3O_4), which indicates there is a trace amount of Fe_3O_4 in the prepared samples.

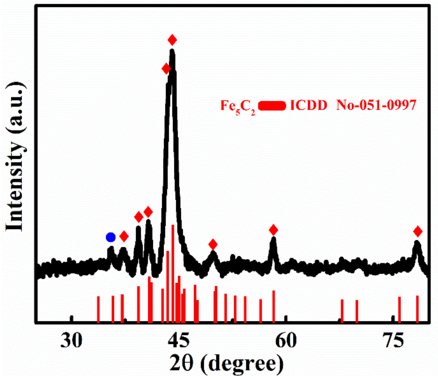

Figure 6.1 XRD patterns of Fe_5C_2 nanoparticles synthesized via thermal decomposition of iron pentacarbonyl. The red bars at the bottom are corresponding to the standard patterns of iron carbide with ICDD card No. 051-0997.

The size and morphology of the Fe_5C_2 NPs were characterized by TEM. Figure 6.2a displays that the Fe_5C_2 NPs were ~15 nm in diameter with narrow size distribution. In addition, all the nanoparticles are with core-shell structure (Figure 6.2a and Figure 6.2b). Figure 6.2c shows the HRTEM image of an isolated 20 nm Fe_5C_2 NP which is the same nanoparticle in red circle in Figure 6.2b. The core part showed highly crystalline features with a lattice spacing of 2.05Å, which corresponding to the (510) plane of Fe_5C_2. The HRTEM image reveals the core of Fe_5C_2 NPs is single crystal, while the shell structure appeared to be amorphous. Some literatures reported that the shell structure of Fe_5C_2 NPs was amorphous carbon.[175, 176]

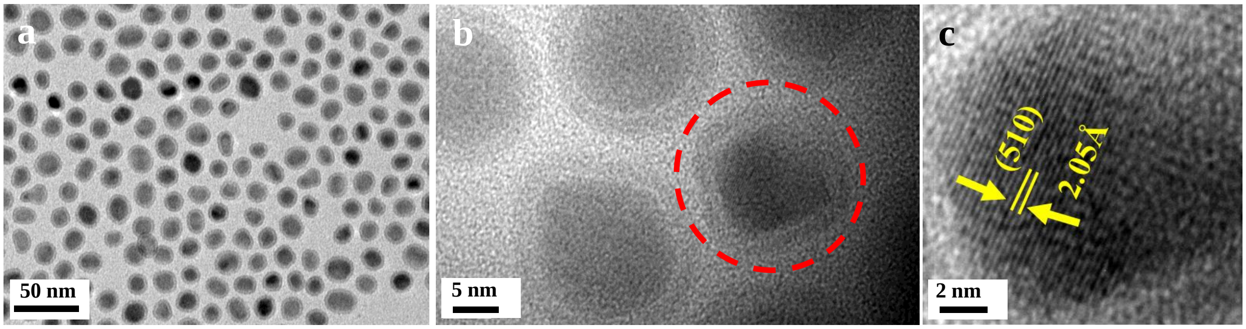

Figure 6.2 (a) and (b) TEM micrograph of Fe_5C_2 nanoparticles synthesized via thermal decomposition of iron pentacarbonyl. (b) HRTEM micrograph of Fe_5C_2 nanoparticles. (c) HRTEM image of a single Fe_5C_2 nanoparticle labeled in (b) with red dashed circle.

Moreover, the particle size could be tuned by altering the concentration of $Fe(CO)_5$ in the mixture. The average particle size of Fe_5C_2 nanoparticles was calculated using Digital Micrograph software. Fe_5C_2 nanoparticles with the mean diameter of ~ 18.4 nm, ~ 15.1 nm, ~ 13.2 nm, and ~ 9.5 nm were obtained shown by the histogram of size distribution in Figure 6.3. Moreover, with the decreased diameter, the size distribution become narrow.

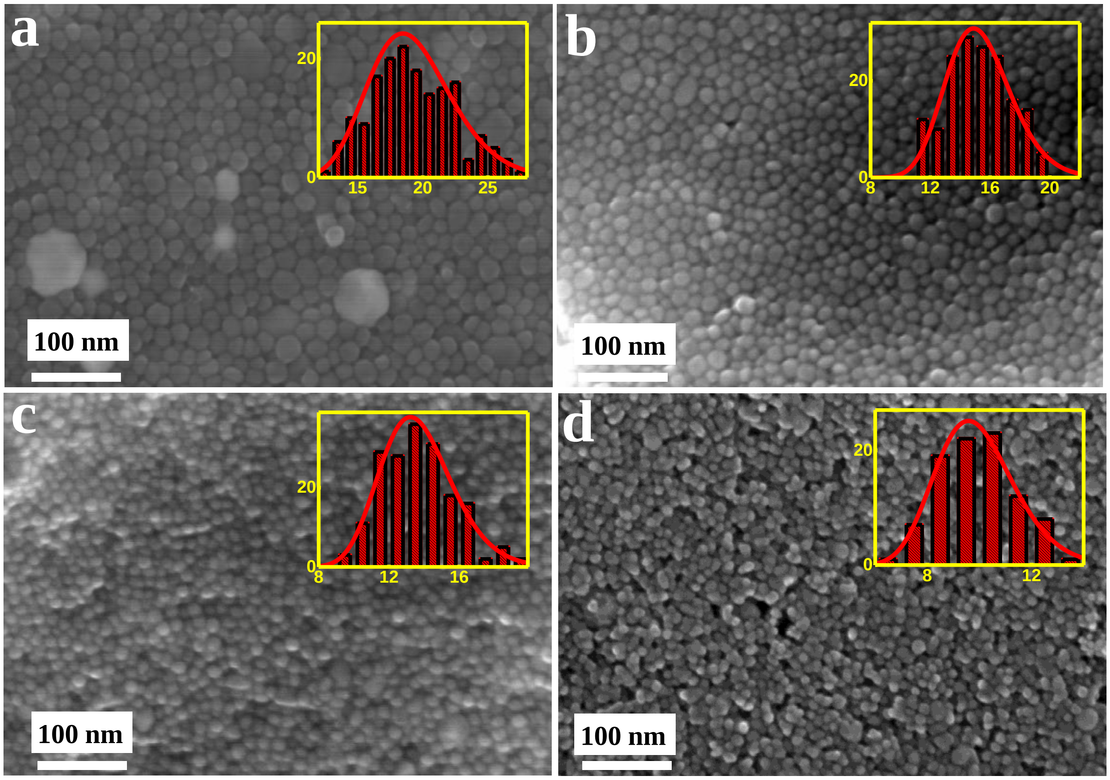

Figure 6.3 SEM micrographs of Fe_5C_2 nanoparticles synthesized by varying iron pentacarbonyl to amine mole concentration: (a) ~ 18.4 nm, (b) ~ 15.1 nm, (c) ~ 13.2 nm, and (d) ~ 9.5 nm. The insets are the histograms of size distributions of Fe_5C_2 nanoparticles. The x-axis and y-axis in the inset represent the diameter and the counts of particles, respectively.

Figure 6.4a shows M-H plots of Fe_5C_2 nanocrystals with mean diameter of ~18.4 nm, ~15.1 nm, and ~9.5 nm at room temperature. The size dependence of coercivity for Fe_5C_2 nanocrystals obtained from Figure 6.4a were summarized in Figure 6.4b. H_C increases with the decrease of size and attains the maximum coercivity of 750 Oe when the mean diameter is approximate 15.1 nm. The enhanced coercivity is attributed to the change of magnetization reversal mechanism in Fe_5C_2 nanocrystals with single crystal core structure.[78] The coherent rotation in Fe_5C_2 nanocrystals with diameter of 15.1 nm results in the optimum coercivity. However, with the further decreased diameter form 15.1 nm to 9.5 nm, H_C decreases to 300 Oe owning to the fluctuation of magnetization in nanocrystals caused by the thermal effects.

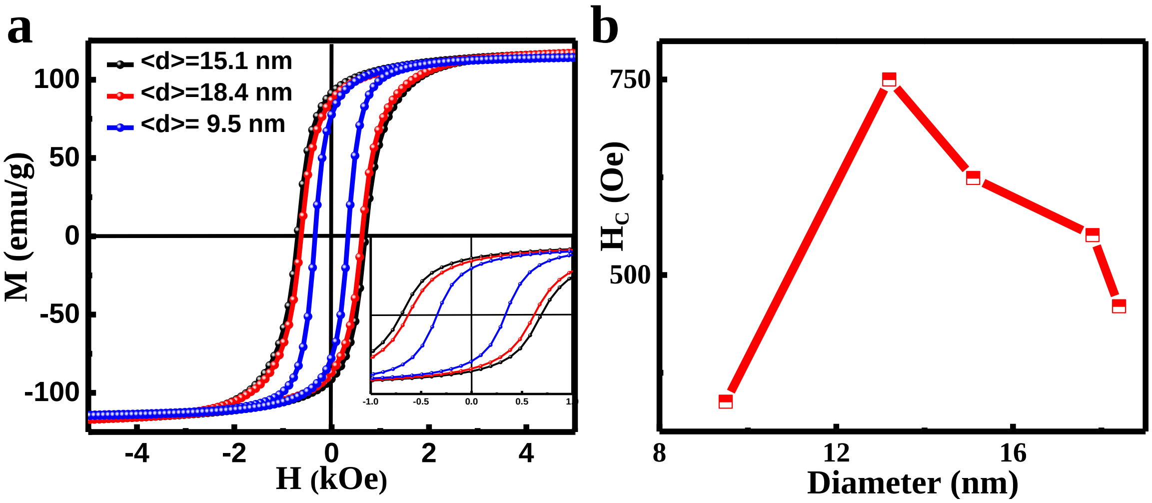

Figure 6.4 (a) M-H plots of Fe_5C_2 nanoparticles with mean diameter of ~18.4 nm, ~15.1 nm and ~9.5 nm at room temperature. (b) The corresponding size dependence of coercivity of Fe_5C_2 NPs at room temperature.

6.4 Morphology Control of Iron Carbide Rod-Shaped Nanoparticles

Due to the scaling effect, the size and shape control are quite effective in optimizing the magnetic properties of Fe_5C_2/Fe_3O_4 nanoparticles. Based on the electron donating ability and ligand stability of different long-chain amines, here we demonstrate the successful synthesis of Fe_5C_2/Fe_3O_4 SNPs and RNPs. Figure 6.5a and b, TEM micrographs of Fe_5C_2/Fe_3O_4 nanocrystals, display the SNPs synthesized using ODA and HDA with average diameter of 13 and 13.5 nm, respectively. Interestingly, RNPs with the mean diameter and length of 13 and 39 nm are obtained when ODA is introduced as the surfactant as shown in Figure 6.5c. Moreover, the SNPs and RNPs of iron carbide/magnetite show the clear core-shell structure as shown in Figure 6.5d.

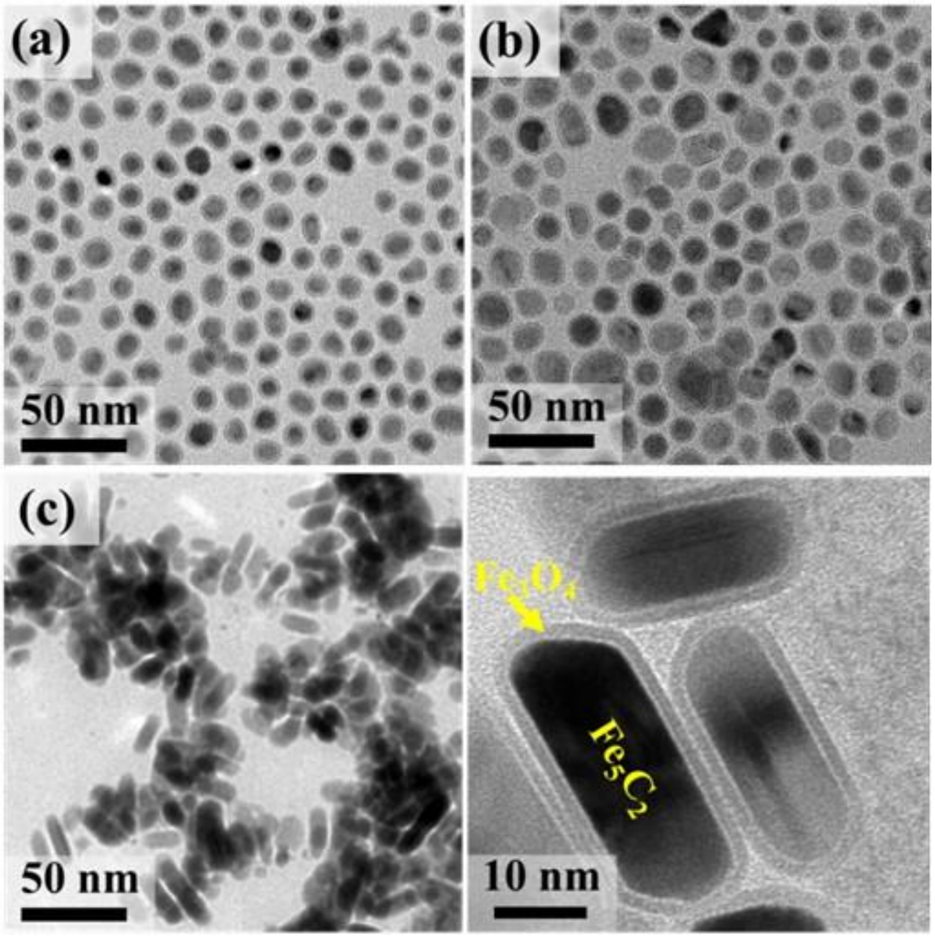

Figure 6.5 TEM micrographs of (a, b) Fe_5C_2 / Fe_3O_4 SNPs and (c) nanorods (NRs) synthesized via using ODA, HDA and DDA as surfactants. (c) HRTEM micrograph of Fe_5C_2 NRs.

To confirm the core-shell structure and reveal the detailed crystal structure of the core and the shell, HRTEM analysis is performed as shown in Figure 6.6. The core and the shell exhibit the crystalline lattice of 0.205 and 2.98 Å corresponds to the (510) crystal plane of the Fe_5C_2 with monoclinic crystal structure and (220) crystal plane of magnetite with spinel-cubic crystal structure, respectively. The shell with the thickness of about 2 nm shows the Fe_3O_4 crystal in the amorphous carbon matrix.[175, 176]

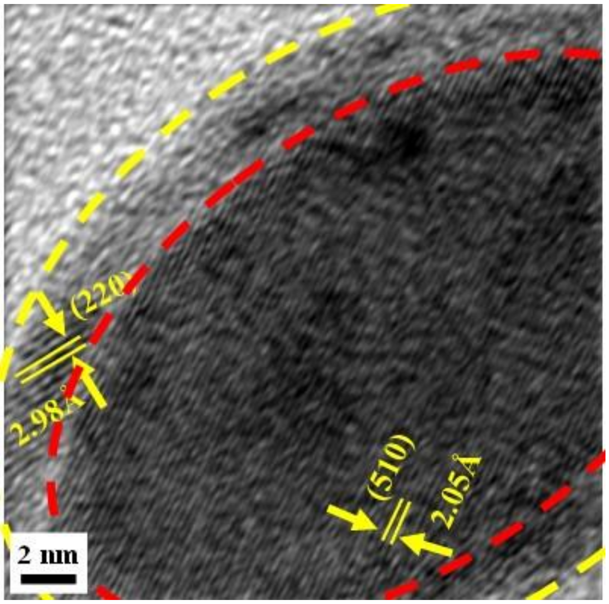

Figure 6.6 HRTEM micrograph of Fe_5C_2 / Fe_3O_4 core-shell nanoparticle.

To further investigate the mechanism for the evolution of the RNPs morphology, the sample were synthesized at 280 °C, 300 °C, and 300 °C with aging for 30 min, 30 min and 1 h, respectively. The corresponding TEM images and XRD patterns of samples are shown in Figure 6.7a-d. The TEM images clearly demonstrate that there is a morphology change from SNPs to RNPs with the elevated reaction temperature and increased aging time. The sample obtained at 280 °C possesses the spherical morphology with the average diameter of 11 nm (see Figure 6.7a). When the temperature is elevated to 300 °C with aging for 0.5 h, the mixture of SNPs and RNPs morphology is obtained as shown in Figure 6.7b. In addition, nanoparticles in red dashed circles show the fusion of two or three NPs into NRs via the collapse of the protective shell during the heating process. After keeping the rection at 300 °C for 1 h, the iron carbide NRs are obtained with the average diameter of 13 nm and the mean length of 38 nm in Figure 6.7c. Moreover, the XRD patterns in Figure 6.7d display the sample possesses iron phase at 280 °C (black curve). It transforms to the mixed phase of iron carbide and iron at 300 °C (red curve). Finally, the iron carbide phase (blue curve) is gained with prolonged heating time. In addition, there is a small hump at 35.5° in all the XRD patterns. This peak matches well with the strongest diffraction peak of magnetite with ICDD card No. 001-1111, which manifests the shell of all the samples is with the magnetite phase. Based on this, the schematic representation of the morphology evolution of RNPs is proposed in Figure 6.7e. Firstly, iron/magnetite core-shell NCs is formed at 280 °C. With the temperature increasing, the magnetite shell collapses, the nanoparticles infuse into the nanorods, and the carbon atom diffuses into the shell resulting in the formation of iron/iron carbide/magnetite intermediate structure. The further increased reaction time yields the iron carbide/magnetite core-shell structure.

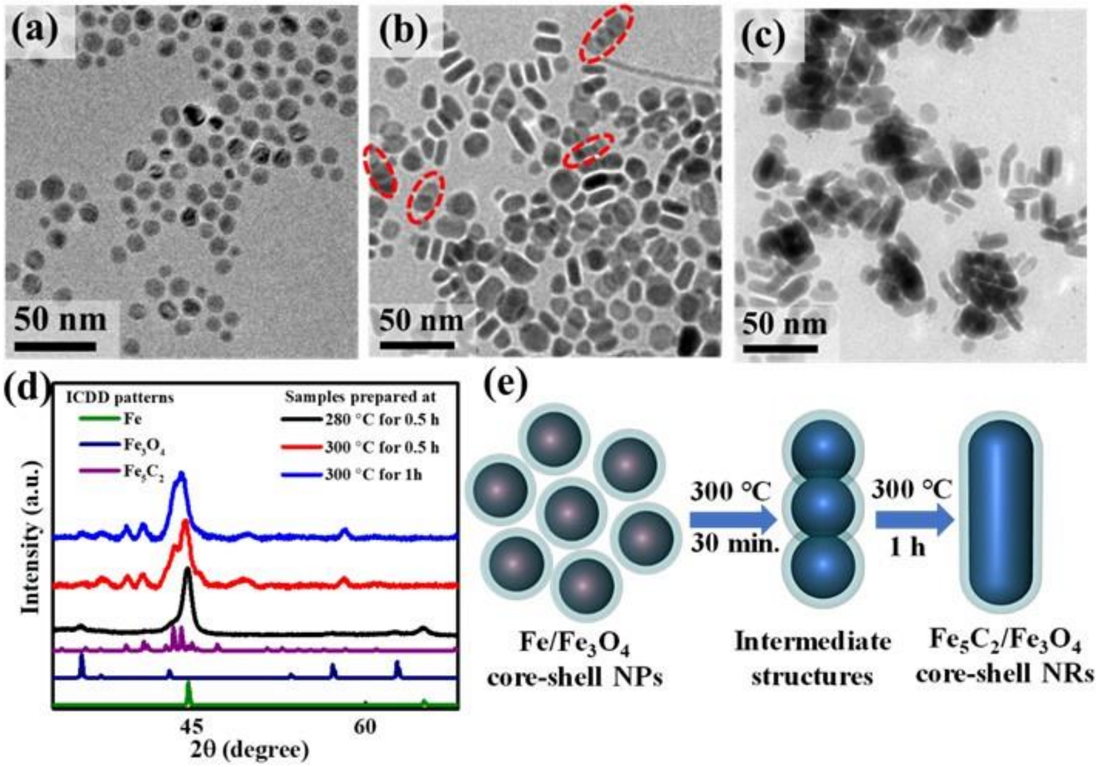

Figure 6.7 TEM micrographs of the samples synthesized at (a) 280 °C, (b) 300 °C, and (c) 300 °C with aging for 30 min, 30 min and 1 h, respectively. (d) The corresponding XRD patterns of samples in (a), (b), and (c). (e) The schematic representation of the morphology evolution of RNPs.

6.5 Mössbauer Spectroscopy Characterization

Mössbauer spectra was performed at room temperature on Fe_5C_2/Fe_3O_4 core-shell RNPs shown in Figure 6.8 to identify the formation of the magnetite shell and the iron carbide core during the synthesis. The two sextets (dark green and dark red) in the fitting analysis confirm Fe_5C_2 as the core and the majority phase. These two sextets represent Fe_5C_2 with different hyperfine parameters.[177, 178] In addition, there are two subspectra resolved sextets which can be clearly identified in Fe_5C_2/Fe_3O_4 core-shell RNPs, one belonging to Fe^{3+} in the tetrahedral (A) site of spinel magnetite structure (the red sextet) and the other one belonging to Fe^{3+} and Fe^{2+} ions located in the octahedral (B) site.[179, 180] These two resoled sextets of Fe^{3+} and Fe^{2+} ions further confirmed the existence of magnetite shell in Fe_5C_2/Fe_3O_4 RNPs. The presence of doublets (purple line) denotes that the possible existence of the superparamagnetic or nonmagnetic state of the Fe atoms.

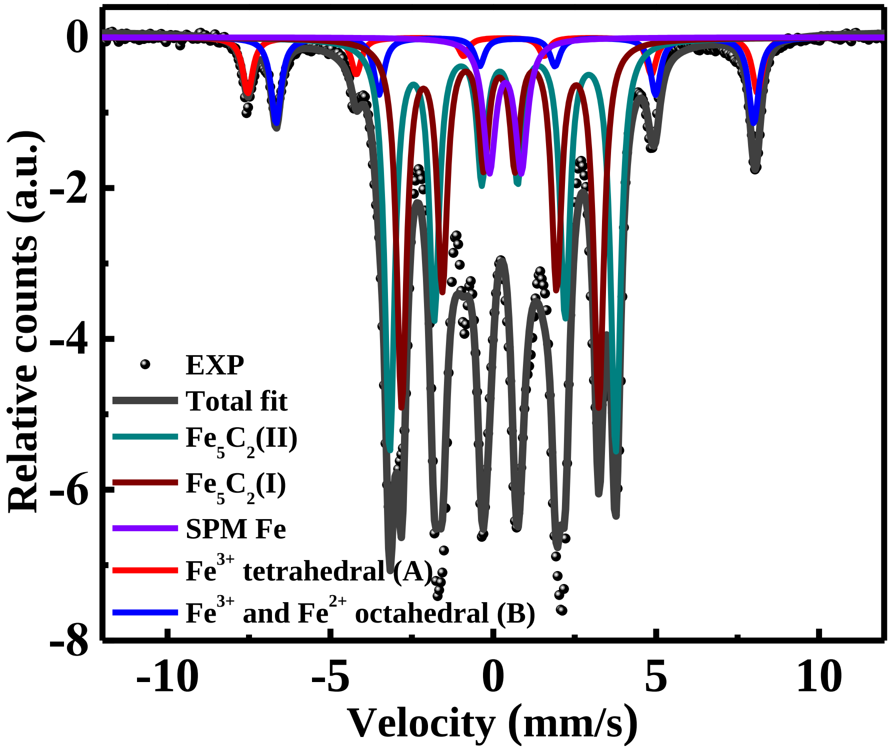

Figure 6.8 Room temperature Mössbauer spectra of Fe_5C_2 / Fe_3O_4 core-shell RNPs.

6.6 Exchange Bias Effects

ZFC and FC magnetization curves are measured to study the low temperature magnetic properties (see Figure 6.9a). Interestingly, the Verwey transition is observed in the Fe_5C_2/ Fe_3O_4 core-shell nanorods and nanoparticles at around 120 K in Figure 6.9a, which should be due to the thin layer of Fe_3O_4. To be mentioned, the Verwey transition temperature of Fe_5C_2/Fe_3O_4 SNPs (136 K) is higher than that of RNPs (116 K). The higher Verwey transition temperature of SNPs should be due to the existence of strain induced by the diverse nanofacets in SNPs.[181, 182] The Verwey transition is a distinctive property of magnetite and is observed in perfect stoichiometry and near 120 K. Below the Verwey transition temperature, the Fe_3O_4 shell undergoes a structural transition from cubic phase to monoclinic phase, which leads to the change of the easy axis from <100> to <110>. Usually, due to the surface defects, Verwey transition is uncommon in the small Fe_3O_4 nanocrystals. However, the good crystallinity of Fe_3O_4 in the shell yields the detected Verwey transition. The phenomena of Verwey transition further consolidate the existence of Fe_3O_4 and is congruent with the previous HRTEM and XRD results. A peak near 50 K is observed in the ZFC curves of Fe_5C_2/ Fe_3O_4 core-shell SNPs and RNPs, which is the blocking temperature (T_B) of representing the superparamagnetic transition of Fe_3O_4 gains in the shell.

M-H curves of the random Fe_5C_2 SNPs (green) and RNPs (blue) at room temperature in Figure 6.9b demonstrate the saturation magnetization value of 119 and 140 emu/g and the coercivity value of 516 and 603 Oe, respectively. Compared to the lower M_S of the SNPs, the prominent M_S of RNPs is owing to the high ratio of iron carbide and better crystallization of magnetite shell in RNPs. The higher H_C of RNPs is ascribed to the contribution of shape anisotropy of nanorod. To confirm this, the iron carbide NRs is aligned under magnetic field of 1.5 T. M-H curves of aligned Fe_5C_2 RNPs measured under parallel magnetic field (blue) and perpendicular magnetic field (green) at room temperature are shown in Figure 6.9c displaying H_C value of 901 and 492 Oe, respectively. The enhanced H_C of aligned iron carbide NRs substantiates the shape anisotropy contribution to the anisotropy field. In order to investigate the effect of the core-shell structure on the magnetic properties of the SNPs and RNPs, the H_{EB} and H_C as a function of temperature are summarized in Figure 6.9d.

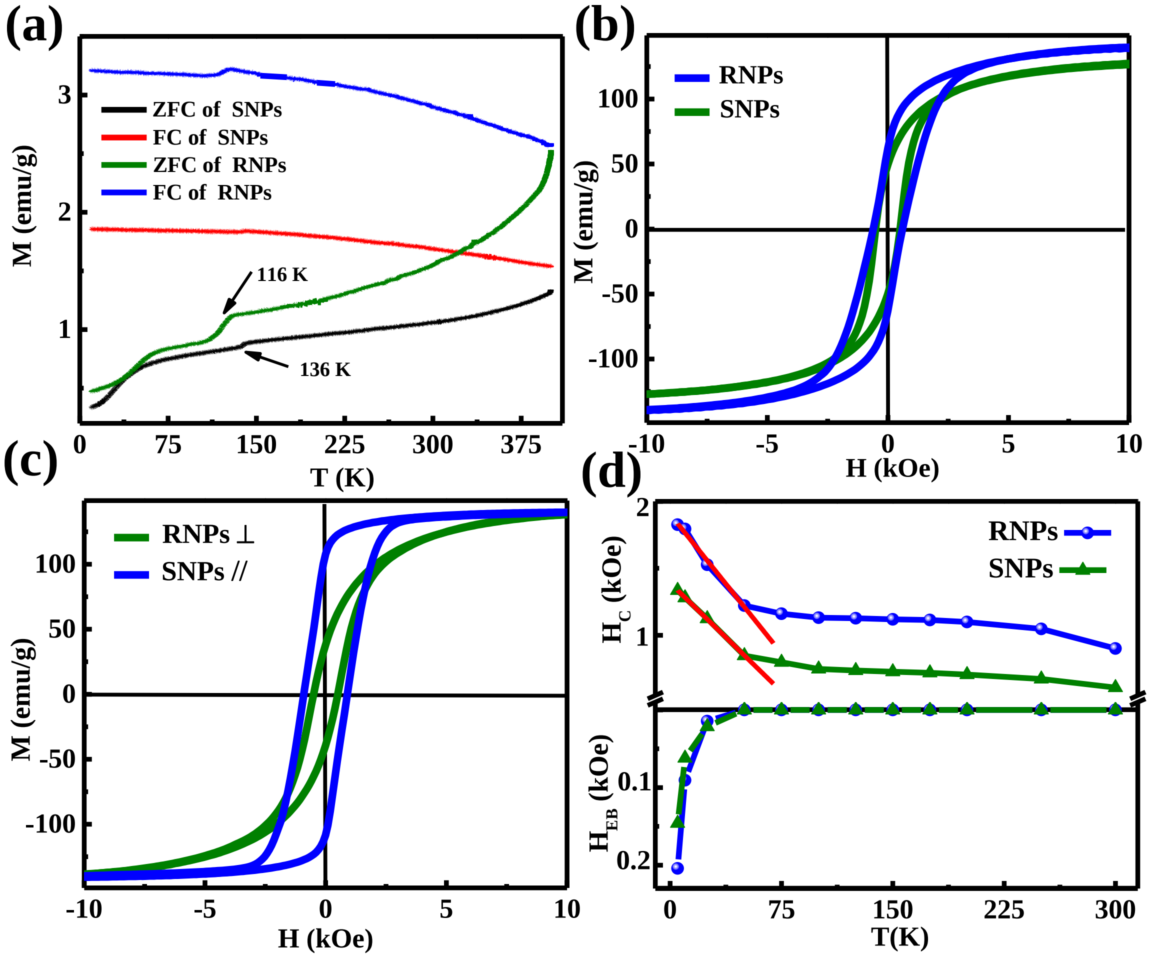

Figure 6.9 (a) ZFC and FC magnetization curves of Fe_5C_2 SNPs (black and red) and RNPs (green and blue). (b) M-H curves of Fe_5C_2 / Fe_3O_4 SNPs (green) and RNPs (blue) at room temperature. (c) M-H curves of aligned Fe_5C_2 RNPs measured under parallel magnetic field (blue) and

perpendicular magnetic field (green) at room temperature. (d) H_C and H_{EB} of temperature dependent curves of Fe_5C_2 SNPs (blue) and RNPs (green).

The most interesting phenomenon is the observation of exchange bias appearing at 50 K. The observed exchange bias behavior below 50 K is related to the Verwey transition in Fe_3O_4 shell, which leads to the change of the easy axis for magnetization and results in the effective exchange coupling at Fe_5C_2/Fe_3O_4 interface. The magnetic signature of the Verwey transition is directly responsible for the presence of exchange bias, which is first observed by Venta *et al.* in Py/Fe_3O_4/V_2O_3 film system.[183, 184] This is the first time to observe the exchange bias in iron carbide nanocrystal system resulting from the effective exchange coupling at Fe_5C_2/Fe_3O_4 interface. More interestingly, it can also be observed that the temperature dependence of H_C of Fe_5C_2/ Fe_3O_4 core-shell NRs is non-monotonous. Initially, it slowly rises to 1.2 kOe at 50 K, then sharply increases to a maximum value of 1.9 kOe at 5 K. The prominent increase of coercivity with low temperature was explained by the low blocking temperature (50 K) of the Fe_3O_4 shell. Above 50 K, Fe_3O_4 shell displays the superparamagnetic behavior and there is not effective exchange coupling in the interface. Below 50 K, the appearance of effective exchange coupling between ferromagnetic Fe_5C_2/ antiferromagnetic Fe_3O_4 results in the exchange bias. Via fitting the temperature dependence of H_C curve with $H_{C(T)} = H_0[1 - \frac{T}{T_B'}]$, T_B' is near 120 K for SNPs and RNPs.[119, 185] T_B' is defined as the temperature where the increasement of H_C happens, which is coincidently same with the Verwey transition temperature. This further consolidates the exchange bias is induced by the Verwey transition. The corresponding contribution of exchange anisotropy to the anisotropy field explains the sharp slope in H_C vs. temperature curve below 50 K.

6.7 Iron Carbide Nanoparticles for Multimodal Hyperthermia Heating

Localized heat induction using magnetic nanoparticles under an alternating magnetic field and photothermal therapy based on gold or silver plasmonic nanostructures are becoming very promising supplementary techniques to the well-established cancer treatments such as radiotherapy and chemotherapy.[175] The efficiency of both techniques for cancer treatment has been studied separately by making their respective nanostructures. As singular thermal therapy showed some limitations, there have been tremendous efforts to synthesize homogeneous nanocrystals with synergistic heat contributions from photothermal effects and magnetic hyperthermia. The schematic view of dual capacity of nanoparticles act as both magnetic hyperthermia agent and photothermal agent is shown in Figure 6.10.

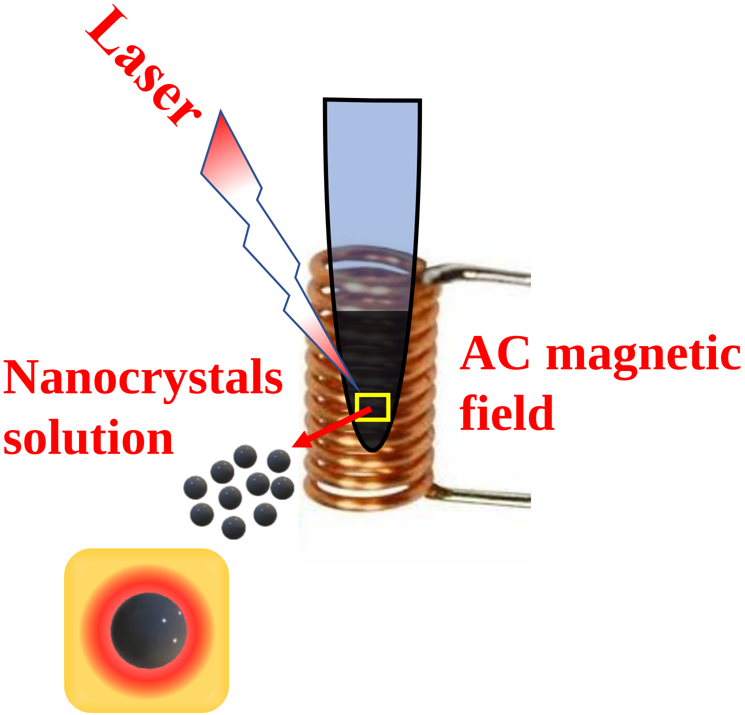

Figure 6.10 Schematic representation of dual capacity of iron carbide nanoparticles act as both magnetic and photothermal agents.

Here, we demonstrate that iron carbide (Fe_5C_2) nanoparticles with a thin amorphous graphitic shell (see Figure 6.11a) have the collective magnetic inductive heating and photothermal effects based on the magnetic and photonic properties. In accordance with the linear response theory, the inductive heating properties reveal a specific absorption rate (SAR) maximum of about 30 W/g at concertation of 4 mg/ml. In addition, exposure of Fe_5C_2 a nanoparticle suspension to near-infrared laser irradiation (808 nm) yields a unprecedented SAR up to 166 W/g (see Figure 6.11b), which is 5 folds higher than that obtained by magnetic stimulation alone. More importantly, the SAR values observed for the magnetite nanoparticles of equivalent size are lower than those of the Fe_5C_2 nanoparticles. The enhanced heating efficiencies in Fe_5C_2 nanoparticles are attributed to the high saturation magnetization and surface-enhanced IR absorption resulted from magnetite coating.

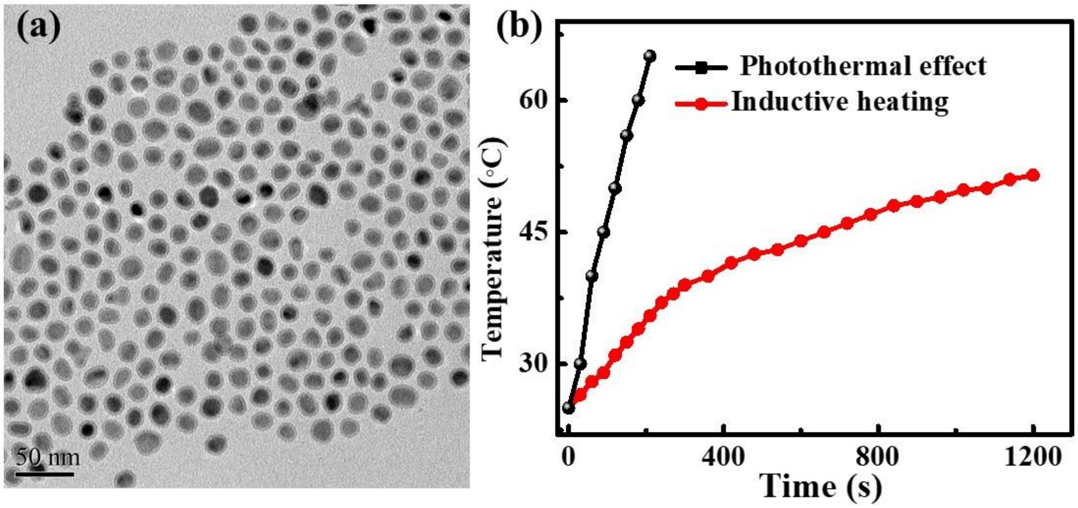

Figure 6.11 (a) TEM micrograph of Fe_5C_2 nanoparticles synthesized via thermal decomposition of iron pentacarbonyl. (b) Temperature changes of Fe_5C_2 nanoparticles suspension under NIR irradiation (808 nm, 0.8 W/cm^2) and AC magnetic field (amplitude of 184 Oe and frequency of 265 kHz).

6.8 Conclusion

The iron carbide/magnetite (Fe_5C_2/Fe_3O_4) core-shell SNPs and RNPs were successfully synthesized by a facile one-pot thermal decomposition process. The maximum coercivity of 750 Oe was achieved in Fe_5C_2/Fe_3O_4 SNPs with mean diameter of 15.1 nm attributing to the coherent rotation. Due to the contribution of shape anisotropy to the anisotropy field, the prominent H_C of 0.9 kOe and 1.9 kOe was obtained in Fe_5C_2/Fe_3O_4 RNPs at room temperature and 5 K, respectively. The exchange bias induced by the Verwey transition is observed in Fe_5C_2/Fe_3O_4 SCNs and RNPs systems. The corresponding exchange anisotropy results in the prominent enhancement of H_C especially below 50 K which is the blocking temperature of Fe_3O_4 NCs in the shell. Owing to the synergistic magnetic hyperthermia effect and photothermal effect, the unprecedented SAR value up to 196 W/g was obtained in Fe_5C_2/Fe_3O_4 NCs.

Chapter 7 Magnetic Hardening in Nickel Carbide Nanoparticles

7.1 Introduction

Nickel carbide nanoparticles (NPs) have attracted considerable interest due to their impressive properties, such as chemical stability, catalytic properties and magnetic properties.[186-189] Theoretical studies have shown that the nickel carbide without defects is diamagnetic due to the strong hybridization of the Ni and C orbitals.[190] However, the Ni_3C NPs synthesized by both the physical and chemical methods always have carbon vacancies, which yield formation of Ni-rich regions.[187, 188, 191] Further, depending on the exchange coupling among the spins in the Ni-rich regions, different magnetic behavior: superparamagnetic, weak ferromagnetic and spin-glass have been noticed.[189, 191-193] Moreover, in nanoparticles the surface spins also dominate the magnetization due to their lower coordination and uncompensated exchange couplings.[194] This in turn leads to the changes in the magnetic properties. Chen *et. al.* demonstrated a weak ferromagnetism and surface spin-glass like state in hexagonal phase Ni_3C nanoparticles.[191] According to our knowledge, these magnetic behaviors have not been studied with variation of carbon content in the nickel carbide NPs. In this study, we first time report the effect of carbon content on the low temperature magnetic properties of rhombohedral nickel carbide nanoparticles. At low temperature, a volume spin-glass like state with high coercivity has been observed in the nickel carbide nanoparticles.

7.2 Synthesis of Nickel Carbide Nanopatrticles

Ni_3C nanoparticles were prepared by the thermal decomposition of nickel (II) acetylacetonate ($Ni(acac)_3$) in oleylamine (OAm) and octadecene.[195] In brief, 20 mmol of $Ni(acac)_3$, 60 mmol OAm and required amount of octadecene were weighed in a three-neck round bottom flask. The reaction mixture was first dehydrated at 100 °C for 30 min under forming gas ambience, then heated to 150 °C and remained at this temperature for 15 min. The temperature was raised to 200 °C later at a rate of 8 °C/min with a further heating for 4 h. After the reaction, the final product was centrifuged and cleaned several times with mixture of acetone and hexane. By varying the octadecene 0, 5, 10 and 20 ml in the original reaction mixture shown in Figure 7.1, we obtained Ni, $Ni_3C_{0.7}$, $Ni_3C_{1.2}$, $Ni_3C_{1.5}$, respectively.

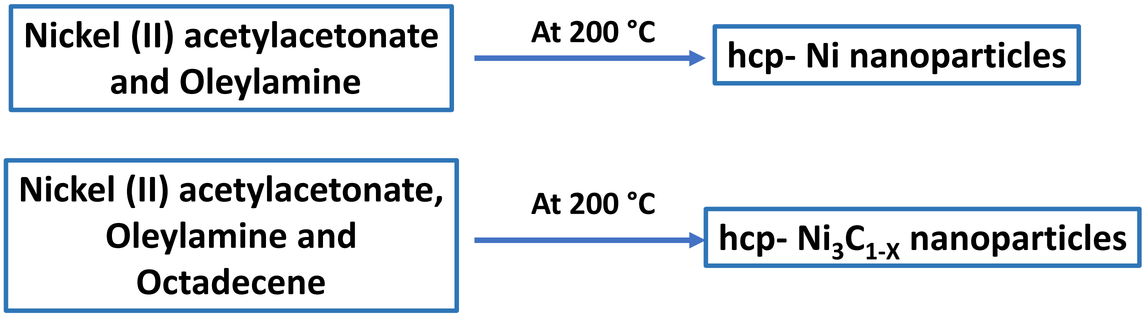

Figure 7.1 Illustration of the octadecene role in the formation processes of Ni_3C_{1-x} nanoparticles.

Powder X-ray diffraction (XRD) spectra were collected from a Rigaku Ultima IV diffractometer with Cu Kα wavelength (1.5406 Å) X-ray source at scan rate of 0.1 °/min to analyze the crystal structure and phase purity. The content of carbon in the prepared samples was determined by the Energy Dispersive X-ray Analysis (EDX) analysis after removing the organic capping. High-resolution transmission electron microscopy (TEM) images were collected to study the particle size and morphology, using a 300 kV Hitachi H-9500. The magnetic properties were measured using physical property measurement system (Quantum Design Dynacool-PPMS).

7.3 Structural Characterization

Figure 7.2a shows XRD pattern of Ni_3C_x (x=0, 0.7, 1.2, 1.5) nanoparticles. It confirms that all the samples have single phase without any impurities. Due to carbon atoms occupying the interstitial position, a higher angle shift in the XRD peak position is seen in Figure 7.2b with the increase of C content.[196] Most of the reflection peaks show Ni and Ni-carbide have identical crystal structure. However, Ni is hexagonal structure and Ni-carbide is classified as a rhombohedral phase, including long range ordering of interstitial carbons with refined hexagonal lattice constants. As the rhombohedral superlattice reflections are very weak, it is difficult to acquire concrete data to confirm rhombohedral supercell. In our slow scanned XRD data, it is substantiated by the minor peaks (102), $(10\bar{4})$ and $(20\bar{2})$ (See in Figure 7.2c).[189] The other peaks account for the reflections from hexagonal sub-cell. Fig.1d and 1e show that the TEM images of $Ni_3C_{0.7}$ and $Ni_3C_{1.5}$ NPs. The morphology and size for both NPs are identical. High-resolution TEM image shown in Figure 7.2f depicts the crystalline nature of Ni carbide NPs. The interplanar distance is 0.204 nm, which is attributed to the (113) plane and well matches with the ICDD 006-0697.

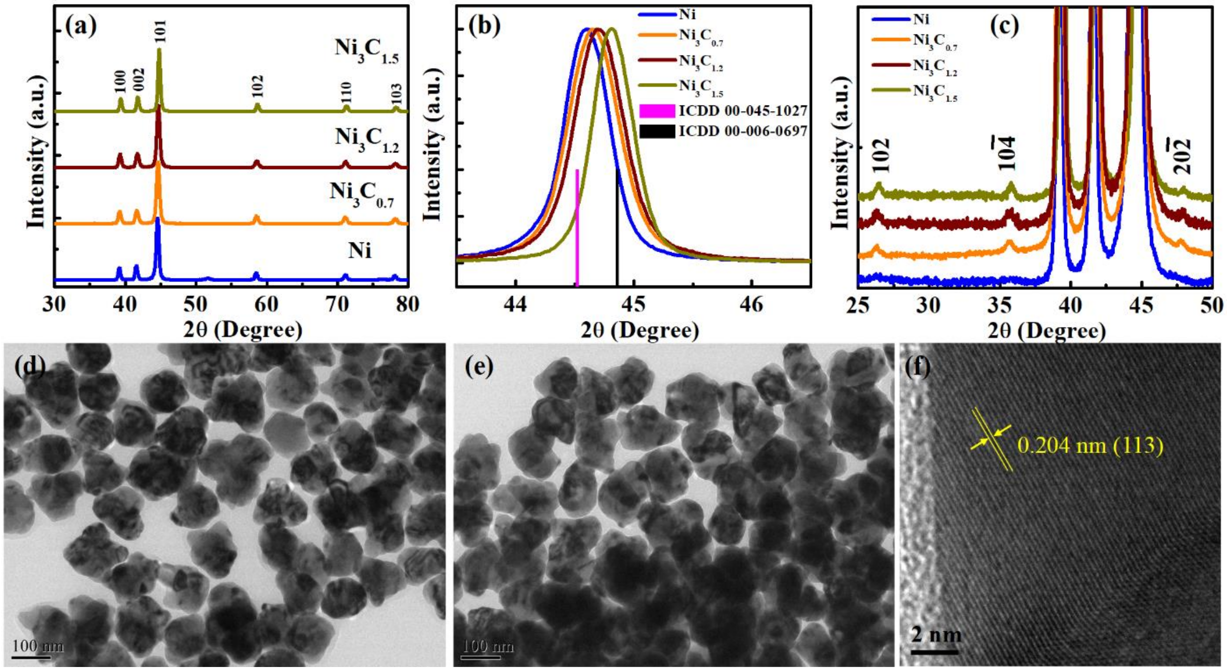

Figure 7.2 (a) XRD pattern of Ni_3C_x (x=0, 0.7, 1.2, 1.5) nanoparticles, (b) shows the shift of (101) XRD peak to higher angle with increase of the C ratio. (c) The rescaled XRD pattern in the 2θ range of 25 -50°. (d) and (e) TEM image of $Ni_3C_{0.7}$ and $Ni_3C_{1.5}$ nanoparticles. (f) High-resolution TEM image of $Ni_3C_{1.5}$.

For the elemental analysis, nickel carbide has also been examined via using EDX analysis. The SEM-EDX analysis of $Ni_3C_{1.5}$ nanoparticles is shown in Figure 7.3, which confirmed the presence of Ni and C. The slight content of Si comes from the Si substrate. In addition, the atom ratio of Ni and C is approximate 2:1, which further demonstrated the successfully systematical control of nickel carbide with different carbon content.

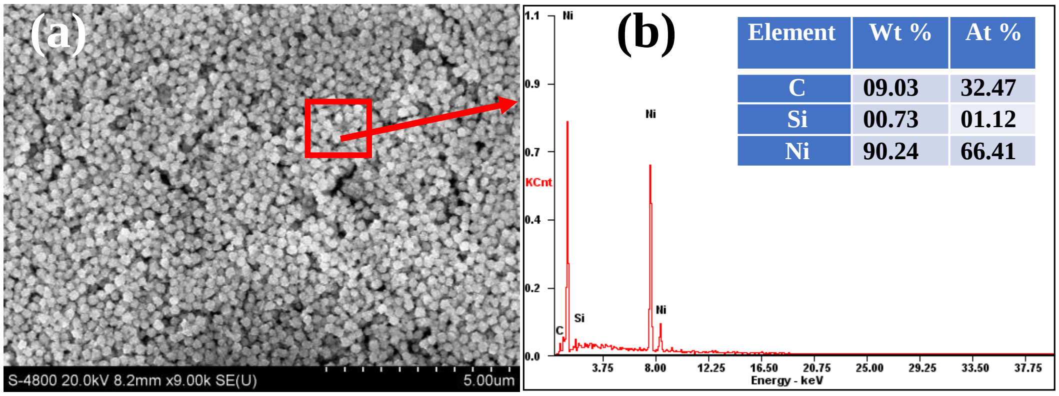

Element	Wt %	At %
C	09.03	32.47
Si	00.73	01.12
Ni	90.24	66.41

Figure 7.3 (a) SEM image of $Ni_3C_{1.5}$ nanoparticles. (b) EDX spectrum analysis of $Ni_3C_{1.5}$ nanoparticles in (a) labeled by the red scan area.

7.4 Evidence of Uncompensated Spin Structure

Figure 7.4a shows zero-field-cooling magnetization curves (ZFC) of Ni_3C nanoparticles under various constant magnetic fields. The ZFC magnetization is increasing with the increase of temperature, attained a maximum value at 17 K (under the magnetic field of 10 Oe) and decreases with further increase of the temperature. In case of superparamagnetic nanoparticles, this type of magnetic cooling effect has been seen when the effective anisotropy energy is equivalent to the thermal energy.[191, 197] It is worthwhile to mention that the ZFC peak position remains within the range 12 to 17 K for all the Ni-carbide nanoparticles. The magnetic cooling effect could also be possible due to the spin-glass freezing of localized spins.

For the confirmation of the magnetic behavior, the FC curves have been measured under different fields 10, 100, 200 and 500 Oe. The FC peak position shifts progressively to lower temperature with the increasing field. The relation between the freezing temperature (T_f) and the applied field can be described by the Almeida–Thouless (AT) equation[198]

$$H / \Delta J \infty \left(1 - \frac{T_f}{T_{f0}}\right)^n \qquad 7.1$$

where T_{f_0} is a fitting parameter representing the freezing temperature at zero field and ΔJ is the width of distribution in exchange interaction. The exponent n is 3/2 for surface spin-glass and 1/2 for volume spin-glass. The AT equation fitting in our case showing a linear trend for n = 1/2. The $H^{1/2}$ dependence of T_f in Figure 7.4b indicates a volume spin glass behavior. The spin-glass freezing temperature obtained by the extrapolation of the AT line to $H = 0$ is 17.4 K.

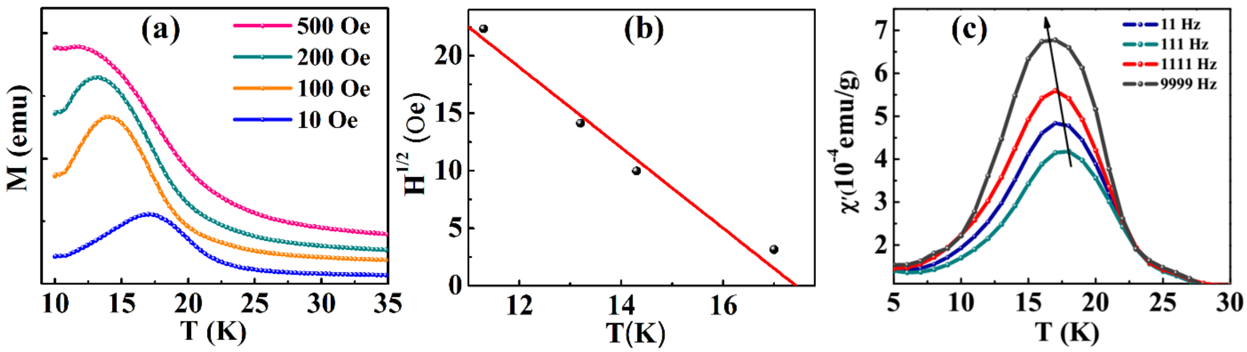

Figure 7.4 (a) Zero-field-cooling magnetization curves of $Ni_3C_{1.5}$ nanoparticles under various constant magnetic fields. (b) The $H^{1/2}$ dependence of T_f. (c) Temperature dependencies of the real part of the ac susceptibility measured with applied field 5 Oe at 11, 111, 1111 and 9999 Hz frequency.

To further clarify the low temperature magnetic state, the temperature dependence of the ac magnetic susceptibility was measured with keeping the ac amplitude constant (H_{ac} = 5 Oe) at 11, 111, 1111 and 9999 Hz frequency (Figure 7.4c). The $\chi'_{(T,f)}$ curve shows a sharp peak at the temperature T_f = 17 K and it is also clear from the figure that the peak position is frequency-dependent. With increase of frequency from 11 to 9999 Hz, the peak position shifts from 17 to 15.4 K (ΔT_f = 2.4 K). The frequency dependence of the T_f can be classified by analyzing the relative shift per decade of frequency, i.e. $\varphi = \frac{\Delta T_f}{T_f \Delta \log f}$, where ΔT_f is the difference between T_f measured in the $\Delta\log(f)$ frequency interval.[197] The value of φ represents the strength of exchange interaction and it falls within the range of 0.004 to 0.018 for spin-glass, whereas for a superparamagnetic phase $0.05 < \varphi < 0.13$.[187, 191, 194, 197] In our studies, the φ values calculated for $Ni_3C_{1.5}$ nanoparticles is ~0.015, which is in the range of spin-glass systems.

7.5 Observation of Magnetic Hardening

Figure 7.5a shows the field dependent magnetization M-H curves for $Ni_3C_{1.5}$ nanoparticles measured at 10 and 300 K. The magnetization does not reach saturation even at the maximum applied field of 50 kOe. This is a typical behavior for a spin-glass phase. The saturation magnetization (M_S) was determined by the extrapolation of the high field linear part of the M versus 1/H curve to H=0 shown in Figure 7.5b. It increases from about 0.5 emu/g at T= 300 K to roughly 9.2 emu/g at T= 10 K. The dramatic enhancement by one order of magnitude in the M_S at low temperature is arising from the spin-glass phase. The low temperature M_S enhancement is more interesting with the change of carbon content. The M_S values are 2.4, 1.4, 1.0 and 0.5 emu/g at 300 K for Ni, $Ni_3C_{0.7}$, $Ni_3C_{1.2}$ and $Ni_3C_{1.5}$ respectively. However, the M_S value trend at 10K is reverse and it increases to 6.6, 7.3, 8.3 and 9.2 emu/g at 10 K. It indicates that the uncompensated spin concentration, i.e. the unreacted Ni atom concentration is increasing with the increase of interstitial carbon occupation. While the room temperature ferromagnetic part is decreasing with the carbon content. The effect of spin-glass state on the coercivity is also noticed in all the carbide samples shown in Figure 7.5c. For example, the H_C for $Ni_3C_{1.5}$ at 300 K is 250 Oe, while it increases to 1.3 kOe at 10 K. The spin-glass phase can be irreversible to the sweeping applied field and results in high Hc at 10 K. Similar enhancement in the H_C attributed to the spin-glass phase has been reported with the iron oxide and Ni nanoparticles.[187, 199] Interestingly, the coercivity values are 0, 20, 190 and 250 Oe at 300 K for Ni, $Ni_3C_{0.7}$, $Ni_3C_{1.2}$ and $Ni_3C_{1.5}$ respectively. It has the same trend at 10 K with 350, 400, 700, to 1300 Oe for Ni, $Ni_3C_{0.7}$, $Ni_3C_{1.2}$, $Ni_3C_{1.5}$, respectively. The enhancement of H_C is due to the increase of the uncompensated Ni atoms with the interstitial substitution of carbon atom. Our experiment shows the weak ferromagnetic and volume spin-glass like behavior in Ni_3C_x nanoparticles. These behaviors can be manipulated by control of carbon content. However, a more detailed study on the structure characterization for the defect state of C vacancies still needs to be investigated.

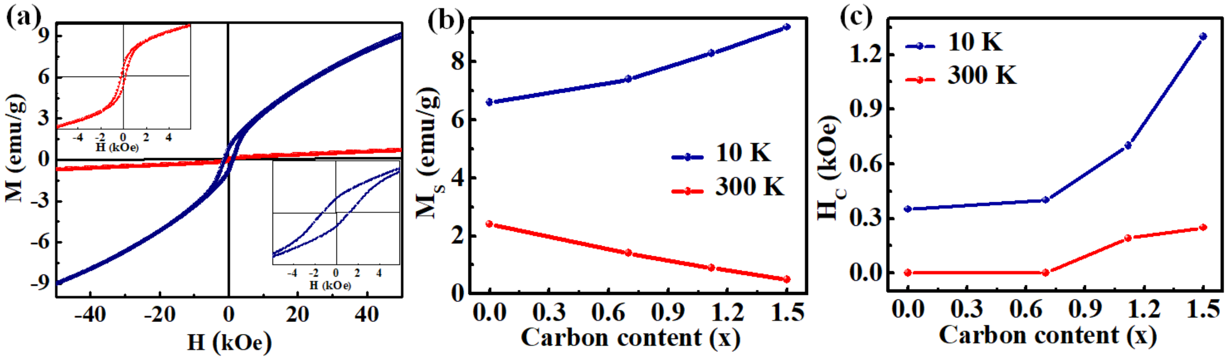

Figure 7.5 (a) The field dependent magnetization M-H curves for $Ni_3C_{1.5}$ nanoparticles measured at 10 and 300 K. The insets are expanded M-H plot in the low-field region. (b) M_S dependence of carbon content at 300 and 10 K for $Ni_3C_{1.5}$ nanoparticles. (c) H_C dependence of carbon content at 300 and 10 K for $Ni_3C_{1.5}$ nanoparticles.

7.6 Conclusion

In summary, we have demonstrated the existence of a low temperature volume spin-glass state and enhanced coercivity in rhombohedral nickel carbide nanoparticles. The spin-glass state exits below 17 K and is confirmed from the field dependence of T_f following the well-known AT line and ac susceptibility measurement. Spin-glass freezing leads to a gradual increase in saturation magnetization (6.6 to 9.2 emu/g) at 10 K and a systematic coercivity enhancement (350 Oe to 1.3kOe) at 10 K. This finding clearly points out the effect of carbon substitution on the structure and magnetic properties of nickel carbide nanoparticles.

Chapter 8 Summary

This dissertation is aimed at the synthesis and characterization of magnetic nanostructures of 3*d* transition metals. The main focus of this work is to investigate the magnetic hardening in the transition-metal nanoparticles, nanowires and their carbide nanostructures. Size effect and the shape anisotropy were utilized to develop high coercivity in the nanostructures. The corresponding AF/AFM core-shell anisotropic nanostructure was obtained via oxidation to explore the exchange bias effects.

The pure hcp-Co NPs and hcp-Co NWs with single domain and single crystalline structure were successfully synthesized via optimizing the reaction conditions such as the surfactant and the nucleation concentration. The diameter of the NPs was systematically controlled to study the size effect on coercivity. Co NPs, Co NWs and Fe_5C_2 NPs with the diameter approximate to the coherent rotation size were obtained via chemical reduction method. As a result, coercivity value of 2.7 kOe and 750 Oe were achieved in hcp-Co NPs and Fe_5C_2 NPs, respectively. Due to the synergistic contribution of magnetocrystalline anisotropy and shape anisotropy, a prominent coercivity of 0.9 kOe was obtained in Fe_5C_2 with rod shaped nanoparticles. Extraordinarily high magnetic coercive force (up to 13.0 kOe) has been achieved in ferromagnetic cobalt nanowires with ultrathin diameter. The coercivity substantially exceeds the magnetocrystalline anisotropy field of cobalt material (7.6 kOe). The angular dependence of coercivity demonstrated that the magnetization reversal in the single-crystal and single-domain Co NWs is proceeded via a coherent rotation mode.

The magnetic properties of single crystalline hcp-Co nanowire assemblies with different packing densities were investigated. For the compacted random Co NW assemblies, they exhibited an unusual increase in coercivity with the increased packing density. While H_C decreased with the further increase in packing density. The initial increase in H_C values was ascribed to magnetostatic interaction between the nanowires, which became stronger with the increased packing density. However, the decrease of H_C was due to the proximity effect as shown in the δM plot. Moreover, it has been found that the variation of H_C with the packing density was also related to diameter of Co NWs. A larger diameter of the nanowires gave a negative dependence of the H_C value with the density in the whole investigated region. For the consolidated aligned Co NW assemblies, they showed the texture and alignment of the nanowires had a strong correlation to the magnetic hardening, which was determined by the magnetization reversal process and the proximity effect. Although a high compaction density of the bulk assemblies leaded to a reduced coercivity value, a trade-off between the coercivity and the magnetization gave rise to a peak value of energy density of 20 MGOe in the consolidated aligned Co nanowire assemblies. The study of Co NWs provides a guideline for materials design of future high-performance and low-cost nanostructured permanent magnets that take advantage of shape anisotropy at nanoscale.

The exchange bias effects in Co/CoO core-shell NPs with hcp-Co core have been investigated. A noticeable exchange bias of 3.2 kOe was observed at 10 K. A dramatic difference of magnetic properties between Co/CoO core-shell NPs and NWs was observed. Compared to the monotonous increase of coercivity with respect to the decreased temperature in Co/CoO NPs, a large drop of coercivity was observed in Co/CoO NWs. The abnormal phenomenon was caused by the superparamagnetic fluctuations in the antiferromagnetic CoO shell which dominated in the flipping of the nanowire magnetization and resulted in the coercivity drop. The ultrathin shell of Fe_3O_4 displayed the Verwey transition at low temperatures. The change of the easy axis from <100> to <110> during the Verwey transition induced exchange bias. The rod-shaped nanoparticles of Fe_5C_2/Fe_3O_4 show more prominent H_{EB} compared to the sphere-shaped nanoparticles due to the effective interface layer between Fe_5C_2/Fe_3O_4 core-shell. Moreover, the unprecedented SAR value up to 196 W/g was obtained in Fe_5C_2/Fe_3O_4 NCs ascribed to the synergistic magnetic hyperthermia effect from the Fe_5C_2 core and photothermal effect from the Fe_3O_4 shell.

Rhombohedral nickel carbide nanoparticles with enhanced magnetic coercivity up to 1.3 kOe at temperature below the spin-glass freezing have been synthesized. The presence of spin-glass state was evident by the field dependence of the freezing temperature following the de Almeida–Thouless relationship. Moreover, the spin-glass state was irreversible to the sweeping applied field and resulted in high H_C.

Appendix A Magnetic Units and Dimensions

Table A.1 Units for magnetic properties

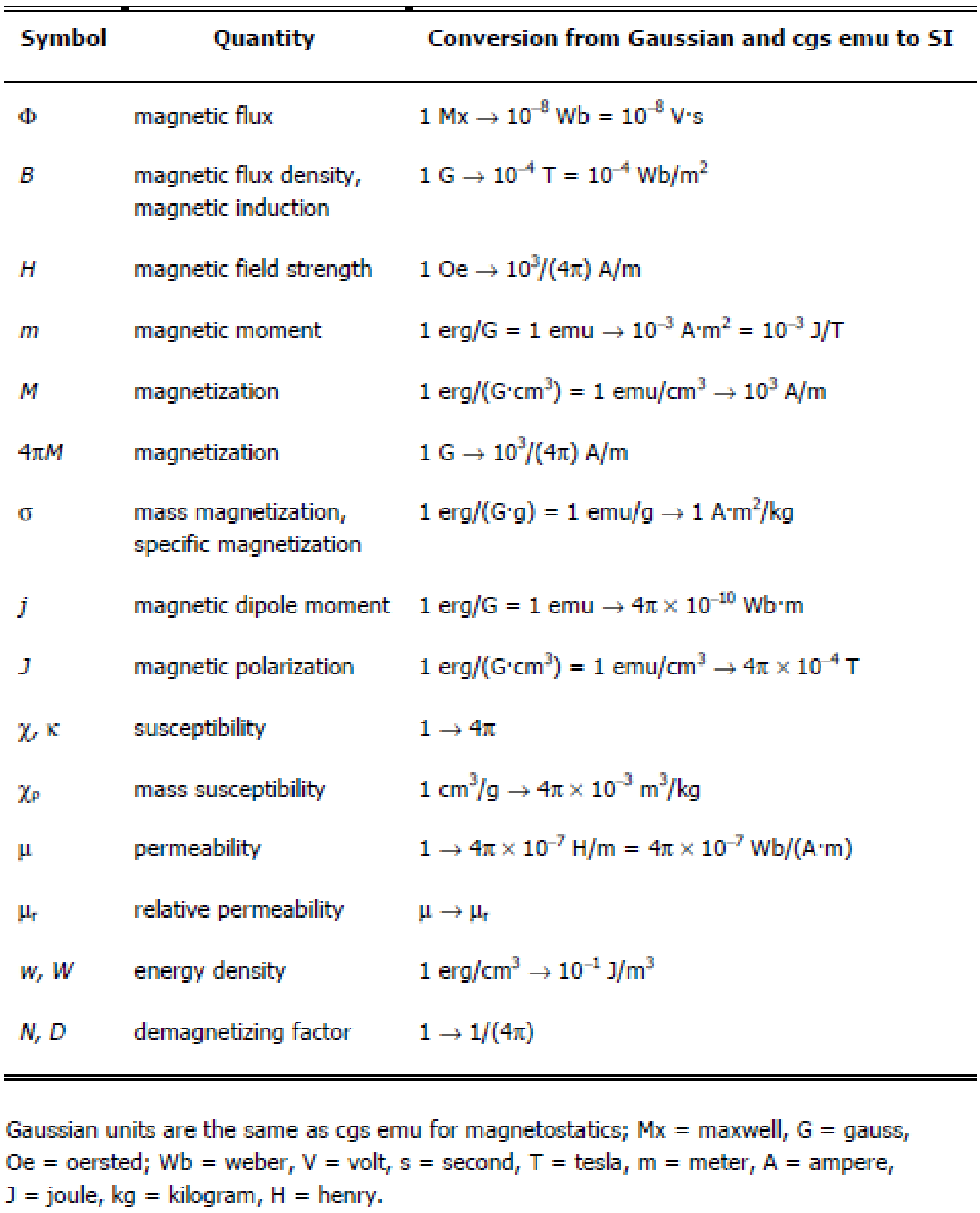

Symbol	Quantity	Conversion from Gaussian and cgs emu to SI
Φ	magnetic flux	$1\ \mathrm{Mx} \rightarrow 10^{-8}\ \mathrm{Wb} = 10^{-8}\ \mathrm{V{\cdot}s}$
B	magnetic flux density, magnetic induction	$1\ \mathrm{G} \rightarrow 10^{-4}\ \mathrm{T} = 10^{-4}\ \mathrm{Wb/m^2}$
H	magnetic field strength	$1\ \mathrm{Oe} \rightarrow 10^{3}/(4\pi)\ \mathrm{A/m}$
m	magnetic moment	$1\ \mathrm{erg/G} = 1\ \mathrm{emu} \rightarrow 10^{-3}\ \mathrm{A{\cdot}m^2} = 10^{-3}\ \mathrm{J/T}$
M	magnetization	$1\ \mathrm{erg/(G{\cdot}cm^3)} = 1\ \mathrm{emu/cm^3} \rightarrow 10^{3}\ \mathrm{A/m}$
$4\pi M$	magnetization	$1\ \mathrm{G} \rightarrow 10^{3}/(4\pi)\ \mathrm{A/m}$
σ	mass magnetization, specific magnetization	$1\ \mathrm{erg/(G{\cdot}g)} = 1\ \mathrm{emu/g} \rightarrow 1\ \mathrm{A{\cdot}m^2/kg}$
j	magnetic dipole moment	$1\ \mathrm{erg/G} = 1\ \mathrm{emu} \rightarrow 4\pi \times 10^{-10}\ \mathrm{Wb{\cdot}m}$
J	magnetic polarization	$1\ \mathrm{erg/(G{\cdot}cm^3)} = 1\ \mathrm{emu/cm^3} \rightarrow 4\pi \times 10^{-4}\ \mathrm{T}$
χ, κ	susceptibility	$1 \rightarrow 4\pi$
χ_ρ	mass susceptibility	$1\ \mathrm{cm^3/g} \rightarrow 4\pi \times 10^{-3}\ \mathrm{m^3/kg}$
μ	permeability	$1 \rightarrow 4\pi \times 10^{-7}\ \mathrm{H/m} = 4\pi \times 10^{-7}\ \mathrm{Wb/(A{\cdot}m)}$
μ_r	relative permeability	$\mu \rightarrow \mu_r$
w, W	energy density	$1\ \mathrm{erg/cm^3} \rightarrow 10^{-1}\ \mathrm{J/m^3}$
N, D	demagnetizing factor	$1 \rightarrow 1/(4\pi)$

Gaussian units are the same as cgs emu for magnetostatics; Mx = maxwell, G = gauss, Oe = oersted; Wb = weber, V = volt, s = second, T = tesla, m = meter, A = ampere, J = joule, kg = kilogram, H = henry.

Several magnetic properties calculation examples.

Energy product (Gaussian)

H: Oe, M: emu/g,

J: 1 erg/(G•cm^3) =1 emu/cm^3, $J = M\rho$

B: G, $B = H + \mu_0 J = H + 4\pi M\rho$, ($\mu_0 J = 4\pi J$, emu/cm^3→Oe)

(BH)max: MGOe, $(BH)_{\max} = B \bullet H$, 1 G•1 Oe=1×10^{-6} MGOe

Exchange length:

$l_{ex} = \sqrt{\frac{A}{4\pi M_S^2}}$ (Gaussian), $l_{ex} = \sqrt{\frac{A}{\mu_0 M_S^2}}$ (SI)

$Nd_2Fe_{14}B$[147, 200]:

$$l_{ex} = \sqrt{\frac{A}{\mu_0 M_S^2}} = \sqrt{\frac{6.6\times10^{-12} J/m}{1.26\times10^{-6} N/A^2 \times 16^2 \times 10^6 G^2}}$$
$$= \sqrt{\frac{6.6\times10^{-12} J/m}{1.26\times10^{-6} J/mA^2 \times 16^2 \times 10^6 \times \left(10^3 / 4\pi\right)^2 A^2/m^2}} = 1.8nm$$

Co (hcp)[68, 147]:

$$l_{ex} = \sqrt{\frac{A}{\mu_0 M_S^2}} = \sqrt{\frac{28\times10^{-12} J/m}{1.26\times10^{-6} N/A^2 \times 17.6^2 \times 10^6 G^2}}$$
$$= \sqrt{\frac{28\times10^{-12} J/m}{1.26\times10^{-6} J/mA^2 \times 17.6^2 \times 10^6 \times \left(10^3 / 4\pi\right)^2 A^2/m^2}} = 2.0nm$$

Anisotropy field (infinite Co NWs)

$$\begin{aligned}
H_A &= \frac{2K_{eff}}{\mu_0 M_S} = \frac{2(K_1 + K_{sh})}{\mu_0 M_S} = \frac{2K_1}{\mu_0 M_S} + \frac{M_S}{2} = \frac{2\times 0.53\times 10^6\, J/m^3}{1.26\times 10^{-6}\, N/A^2 \times 17.6kG} + \frac{17.6kG}{2} \\
&= \frac{2\times 0.53\times 10^6\, J/m^3}{1.26\times 10^{-6}\, J/mA^2 \times 17.6kG} + \frac{17.6kG}{2} = \frac{2\times 0.53\times 10^6\, A^2/m^2}{1.26\times 10^{-6} \times 17.6kG} + \frac{17.6kG}{2} \qquad , \\
&= \frac{2\times 0.53\times 10^6}{1.26\times 10^{-6} \times 17.6kG} \times \left(\frac{4\pi}{10^6}\right)^2 G^2 + \frac{17.6kG}{2} = (7.5 + 8.8)kOe = 16.3kOe
\end{aligned}$$

Magnetic hardness parameter:

$$\kappa = \left(\frac{K_{eff}}{4\pi M_S^2}\right)^{1/2} \text{ (Gaussian)}, \quad \kappa = \left(\frac{K_{eff}}{\mu_0 M_S^2}\right)^{1/2} \text{ (SI)}$$

$Nd_2Fe_{14}B$[147, 200]:

$$\begin{aligned}
\kappa &= \sqrt{\frac{K_{eff}}{\mu_0 M_S^2}} = \sqrt{\frac{5.0\times 10^6\, J/m^3}{1.26\times 10^{-6}\, N/A^2 \times 16^2 \times 10^6 G^2}} \\
&= \sqrt{\frac{5.0\times 10^6\, J/m^3}{1.26\times 10^{-6}\, J/mA^2 \times 16^2 \times 10^6 \times \left(10^3/4\pi\right)^2 A^2/m^2}} = 1.56
\end{aligned}$$

Co (hcp)[68, 147]:

$$\begin{aligned}
\kappa &= \sqrt{\frac{K_{eff}}{\mu_0 M_S^2}} = \sqrt{\frac{1.14\times 10^6\, J/m^3}{1.26\times 10^{-6}\, N/A^2 \times 17.6^2 \times 10^6 G^2}} \\
&= \sqrt{\frac{1.14\times 10^6\, J/m^3}{1.26\times 10^{-6}\, J/mA^2 \times 17.6^2 \times 10^6 \times \left(10^3/4\pi\right)^2 A^2/m^2}} = 0.68
\end{aligned}$$

Appendix B Research Accomplishments

Awards

- James L. Horwitz Scholarship, Department of Physics, UTA, 2020.
- Group on Magnetism (GMAG) Student Travel Award, American Physical Society (APS) March Meeting 2019.
- James L. Horwitz Scholarship, Department of Physics, UTA, 2019.
- Student Travel Award, Rare-Earth Permanent Magnet Conference (REPM) 2018.
- Truman D. Black Scholarship, Department of Physics, UTA, 2018.

Publications

1. **Meiying Xing**, Jeotikanta Mohapatra**,** Julian Beatty, Jacob Elkins and J. Ping Liu, *Exchange bias induced by verwey transition in the iron carbide/magnetite core-shell nanocrystals.* (in preparation)
2. Jeotikanta Mohapatra, **Meiying Xing**, Kinjal Gandha, Yuqing Li, Ming. Yue, Guoping Zhao and J. Ping Liu, *Magnetic hardening in Co nanowire assemblies: Coercivity limited by the geometric factors and proximity effect.* (in preparation)
3. Jeotikanta Mohapatra, **Meiying Xing**, Jacob Elkins, Julian Beatty and J. Ping Liu, *Size dependent magnetic hardening in* $CoFe_2O_4$ *nanoparticles: effects of surface spin canting.* (submitted)
4. Jeotikanta Mohapatra, Jacob Elkins, **Meiying Xing**, D. Guragain, Sanjay R Mishra, and J. Ping Liu. *Magnetic-field-induced self-assembly of exchange-coupled* $FeCo/CoFe_2O_4$ *core/shell nanoparticles with tunable coercivity.* (in preparation)

5. Jacob Elkins, Jeotikanta Mohapatra, **Meiying Xing**, Julian Beatty and J. Ping Liu. *Magnetic hardening in CoNi nanowires: role of composition and morphology*. (in preparation)
6. Jeotikanta Mohapatra**, Meiying Xing**, Julian Beatty, Jacob Elkins and J. Ping Liu, *Enhancing the Magnetic and Inductive Heating Properties of* Fe_3O_4 *Nanoparticles via Morphology Control, Nanotechnol.* **2020**, 31, 275706.
7. Jeotikanta Mohapatra, **Meiying Xing**, Jacob Elkins, J Ping Liu, *Hard and semi-hard magnetic materials based on cobalt and cobalt alloys, J. Alloys Compd.* **2020**, *824*, 153874.
8. Chudal, Lalit, Nil Kanatha Pandey, Jonathan Phan, Omar Johnson, LiangWu Lin, Hongmei Yu, Yang Shu, **Meiying Xing***, et al. Copper-Cysteamine Nanoparticles as a Heterogeneous Fenton-Like Catalyst for Highly Selective Cancer Treatment*. *ACS Appl. Bio Mater.* **2020**.
9. **Meiying Xing**, Jeotikanta Mohapatra, Jacob Elkins, Julian Beatty, and J Ping Liu. *Effects of Packing Density on the Magnetic Properties of Cobalt Nanowire Assemblies*. *AIP Adv.* **2019**, 9, no. 3, 035323.
10. Mohapatra, Jeotikanta, **Meiying Xing**, and J Ping Liu. *Inductive Thermal Effect of Ferrite Magnetic Nanoparticles. Mater.* 12, no. 19 (**2019**): 3208.
11. Pandey, Nil Kanatha, Lalit Chudal, Jonathan Phan, Liangwu Lin, Omar Johnson, **Meiying Xing**, J Ping Liu, *et al. A Facile Method for the Synthesis of Copper–Cysteamine Nanoparticles and Study of Ros Production for Cancer Treatment. J. Mater. Chem. B* 7, no. 42 (**2019**): 6630-42.
12. **Meiying Xing**, Jeotikanta Mohapatra, Fanhao Zeng and J. Ping Liu, *Magnetic Properties of Nickel Carbide Nanoparticles with Enhanced Coercivity, AIP Adv.* **2018,** 8 (5), 056308.

13. Narayan Poudyal, Jeotikanta Mohapatra, **Meiying Xing**, Choong-Un Kim and J. Ping Liu, *High-temperature m agnetic properties of exchange-coupled SmCo/NdFeB, hybrid nanocomposite magnets, IEEE Magn. Lett.* **2018**, 9, 5501604.
14. Jeotikanta Mohapatra, **Meiying Xing** and J. Ping Liu, *Magnetic and hyperthermia properties of* $Co_xFe_{3-x}O_4$ *nanoparticles synthesized via cation exchange, AIP Adv.* **2018**, 8 (5), 056308.
15. Mohapatra, Jeotikanta, Fanhao Zeng, Kevin Elkins, **Meiying Xing**, Madhav Ghimire, Sunghyun Yoon, Sanjay R Mishra, and J Ping Liu. *Size-Dependent Magnetic and Inductive Heating Properties of* Fe_3O_4 *Nanoparticles: Scaling Laws across the Superparamagnetic Size*. *Phys. Chem. Chem. Phys.* 20, no. 18 (**2018**): 12879-87.

Conference Presentations

1. **Meiying Xing**, Jeotikanta Mohapatra, Jacob Elkins, Julian Beatty and J. Ping Liu, *Tuning Exchange Bias and Training Effect by Controlling the Interface Coupling in Co/CoO Core/Shell Nanoparticles*, 64th Magnetism and Magnetic Materials (MMM) Conference 2019 (**Oral**).
2. Jacob Elkins, Jeotikanta Mohapatra, **Meiying Xing**, Julian Beatty and J. Ping Liu. *Magnetic hardening in CoNi nanowires: role of composition and morphology*. 64th Magnetism and Magnetic Materials (MMM) Conference 2019 (**Poster**).
3. **Meiying Xing**, Jeotikanta Mohapatra, Jacob Elkins, Julian Beatty and J. Ping Liu, *Ultrathin cobalt nanowires with high energy product,* APS March Meeting 2019 (**Oral**).
4. **Meiying Xing**, Jeotikanta Mohapatra, Jacob Elkins, Julian Beatty, and J Ping Liu, *Effects of Packing Density on the Magnetic Properties of Cobalt Nanowire Assemblies*. 63rd Magnetism and Magnetic Materials (MMM) Conference 2018 (**Poster**).

5. Julian Beatty, Jeotikanta Mohapatra, **Meying Xing**, Jacob Elkins, J. Ping Liu, *Shape anisotropy effects on stoichiometry, magnetic and hyperthermia properties of iron oxide nanoparticles.* 63rd Magnetism and Magnetic Materials (MMM) Conference 2018 (**Oral**).
6. **Meiying Xing**, Jeotikanta Mohapatra, and J. Ping Liu, Magnetic *Hardening in Co Nanowire Assembies*, REPM 2018, Peking University (**Oral**).
7. Jeotikanta Mohapatra, **Meiying Xing** and J. Ping Liu, *Training effect of exchange bias in Co/CoO core-shell nanowire films*, International Conference on Magnetism (ICM) 2018, San Francisco (**Poster**).
8. J. Ping Liu, Kinjal Gandha, Jeotikanta Mohapatra and **Meiying Xing**, *Hydrothermally synthesized Co nanowire assemblies with high coercivity*, Materials Research Society (MRS) Spring Meeting & Exhibit 2018 (**Oral**).
9. Jeotikanta Mohapatra, **Meiying Xing** and J. Ping Liu, *Magnetic and hyperthermia properties of* $Co_xFe_{3-x}O_4$ *nanoparticles synthesized via cation exchange*, MMM Conference 2017 (**Poster**).
10. **Meiying Xing**, Jeotikanta Mohapatra, Fanhao Zeng and J. Ping Liu, Magnetic Properties of Nickel Carbide Nanoparticles with Enhanced Coercivity, MMM Conference 2017 (**Poster**).

References

1. Coey, J. M., *Magnetism and magnetic materials*. Cambridge university press: 2010; p 62.

2. Yosida, K.; Mattis, D. C.; Yosida, K.; Yamada, K.; Shiba, H., *Theory of magnetism.: Edition en anglais*. Springer: 1996.

3. Coey, J. M. D., *Magnetism and magnetic materials*. Cambridge university press: 2010; p 168.

4. Coey, J. M., *Magnetism and magnetic materials*. Cambridge university press: 2010; p 169.

5. Lewis, L. H.; Jiménez-Villacorta, F. *Metall. Mater. Trans. A* **2013,** 44, (1), 2-20.

6. Sun, L.; Hao, Y.; Chien, C.; Searson, P. C. *IBM J. Res. Dev.* **2005,** 49, (1), 79-102.

7. Skomski, R.; Coey, J. *Scr. Mater.* **2016,** 112, 3-8.

8. Cullity, B. D.; Graham, C. D., *Introduction to magnetic materials*. John Wiley & Sons: 2011.

9. Mohapatra, J.; Liu J. P., Rare-Earth-Free Permanent Magnets: The Past and Future. In *Handbook of Magnetic Materials*, Elsevier: 2018; Vol. 27, pp 1-57.

10. Peng, L.-C.; Zhang, T.; Zuo, S.-L.; He, M.; Cai, J.-W.; Wang, S.-G.; Wei, H.-X.; Li, J.-q.; Zhao, T.-y.; Shen, B.-g. *Chin. Phys. B* **2018,** 27, (6), 066802.

11. Coey, J. M., *Magnetism and magnetic materials*. Cambridge university press: 2010; p 242.

12. Ott, F.; Piquemal, J.-Y.; Viau, G., High-Aspect-Ratio Nanoparticles: Growth, Assembly, and Magnetic Properties. In *Magnetic Structures of 2D and 3D Nanoparticles*, Jenny Stanford Publishing: 2018; pp 213-255.

13. Jimenez-Villacorta, F.; Lewis, L. H., Advanced permanent magnetic materials. One Central Press Manchester, UK: 2014; pp 161-189.

14. Lee, J. S.; Cha, J. M.; Yoon, H. Y.; Lee, J.-K.; Kim, Y. K. *Sci. Rep.* **2015,** 5, (1), 1-7.

15. Tannous, C.; Gieraltowski, J. *European journal of physics* **2008,** 29, (3), 475.

16. Sun, L.; Hao, Y.; Chien, C.-L.; Searson, P. C. *IBM J. Res. Dev.* **2005,** 49, (1), 79-102.

17. Stoner, E. C.; Wohlfarth, E. *Philosophical Transactions of the Royal Society of London. Series A, Mathematical and Physical Sciences* **1948,** 240, (826), 599-642.

18. Zhou, L.; Miller, M. K.; Lu, P.; Ke, L.; Skomski, R.; Dillon, H.; Xing, Q.; Palasyuk, A.; McCartney, M.; Smith, D. *Acta Mater.* **2014,** 74, 224-233.

19. Gandha, K.; Elkins, K.; Poudyal, N.; Liu, X.; Liu, J. P. *Scientific reports* **2014,** 4, 5345.

20. Mohaddes-Ardabili, L.; Zheng, H.; Ogale, S.; Hannoyer, B.; Tian, W.; Wang, J.; Lofland, S.; Shinde, S.; Zhao, T.; Jia, Y. *Nature materials* **2004,** 3, (8), 533-538.

21. Soares, J.; Galdino, V.; Conceição, O.; Morales, M.; De Araújo, J.; Machado, F. *J. Magn. Magn. Mater.* **2013,** 326, 81-84.

22. Liu, C.; Wu, X.; Klemmer, T.; Shukla, N.; Weller, D.; Roy, A. G.; Tanase, M.; Laughlin, D. *Chem. Mater.* **2005,** 17, (3), 620-625.

23. Nandwana, V.; Chaubey, G. S.; Yano, K.; Rong, C.-b.; Liu, J. P. *J. Appl. Phys.* **2009,** 105, (1), 014303.

24. Matsushita, T.; Iwamoto, T.; Inokuchi, M.; Toshima, N. *Nanotechnol.* **2010,** 21, (9), 095603.

25. Dong, Y.; Zhang, T.; Xia, Z.; Wang, H.; Ma, Z.; Liu, X.; Xia, W.; Coey, J. M. D.; Jiang, C. *Nanoscale* **2019,** 11, (36), 16962-16967.

26. Zhong, Y.; Chaudhary, V.; Tan, X.; Parmar, H.; Ramanujan, R. *Nanoscale* **2017,** 9, (47), 18651-18660.

27. Chaudhary, V.; Zhong, Y.; Parmar, H.; Tan, X.; Ramanujan, R. V. *ChemPhysChem* **2018,** 19, (18), 2370-2379.

28. Kim, J.; Wu, H.-L.; Hsu, S.; Matsumoto, K.; Sato, R.; Teranishi, T. *Chem. Lett.* **2019,** 48, (9), 1054-1057.

29. Okada, S.; Suzuki, K.; Node, E.; Takagi, K.; Ozaki, K.; Enokido, Y. *J. Alloys Compd.* **2017,** 695, 1617-1623.

30. Yoon, H.; Xu, A.; Sterbinsky, G. E.; Arena, D. A.; Wang, Z.; Stephens, P. W.; Meng, Y. S.; Carroll, K. J. *Phys. Chem. Chem. Phys.* **2015,** 17, (2), 1070-1076.

31. Carroll, K. J.; Huba, Z. J.; Spurgeon, S. R.; Qian, M.; Khanna, S. N.; Hudgins, D. M.; Taheri, M. L.; Carpenter, E. E. *Appl. Phys. Lett.* **2012,** 101, (1), 012409.

32. Harris, V.; Chen, Y.; Yang, A.; Yoon, S.; Chen, Z.; Geiler, A.; Gao, J.; Chinnasamy, C.; Lewis, L.; Vittoria, C. *J. Phys. D: Appl. Phys.* **2010,** 43, (16), 165003.

33. Burkert, T.; Nordström, L.; Eriksson, O.; Heinonen, O. *Phys. Rev. Lett.* **2004,** 93, (2), 027203.

34. Wu, D.; Zhang, Q.; Liu, J. P.; Yuan, D.; Wu, R. *Appl. Phys. Lett.* **2008,** 92, (5), 052503.

35. Hasegawa, T.; Kanatani, S.; Kazaana, M.; Takahashi, K.; Kumagai, K.; Hirao, M.; Ishio, S. *Sci. Rep.* **2017,** 7, (1), 13215.

36. Giannopoulos, G.; Salikhov, R.; Varvaro, G.; Psycharis, V.; Testa, A. M.; Farle, M.; Niarchos, D. *J. Phys. D: Appl. Phys.* **2018,** 51, (5), 055009.

37. Blizak, S.; Bihlmayer, G.; Blügel, S. *Phys. Rev. B* **2012,** 86, (9), 094436.

38. Yildiz, F.; Luo, F.; Tieg, C.; Abrudan, R. M.; Fu, X. L.; Winkelmann, A.; Przybylski, M.; Kirschner, J. *Phys. Rev. Lett.* **2008,** 100, (3), 037205.

39. Winkelmann, A.; Przybylski, M.; Luo, F.; Shi, Y.; Barthel, J. *Phys. Rev. Lett.* **2006,** 96, (25), 257205.

40. He, J.; Bian, B.; Zheng, Q.; Du, J.; Xia, W.; Zhang, J.; Yan, A.; Liu, J. P. *Green Chem.* **2016,** 18, (2), 417-422.

41. Kim, J.; Rong, C.; Liu, J. P.; Sun, S. *Adv. Mater.* **2009,** 21, (8), 906-909.

42. Khan, I.; Hong, J. *J. Phys. D* **2014,** 47, (41), 415002.

43. Gong, M.; Kirkeminde, A.; Wuttig, M.; Ren, S. *Nano Lett.* **2014,** 14, (11), 6493-6498.

44. Shen, J.; Gong, M.; Dai, Q.; Ren, S. *ACS Appl. Mater. Interfaces* **2016,** 8, (1), 31-36.

45. Li, Q.; Wu, L.; Wu, G.; Su, D.; Lv, H.; Zhang, S.; Zhu, W.; Casimir, A.; Zhu, H.; Mendoza-Garcia, A. *Nano Lett.* **2015,** 15, (4), 2468-2473.

46. Balamurugan, B.; Das, B.; Shah, V. R.; Skomski, R.; Li, X. Z.; Sellmyer, D. J. *Appl. Phys. Lett.* **2012,** 101, (12), 122407.

47. Balamurugan, B.; Das, B.; Zhang, W. Y.; Skomski, R.; Sellmyer, D. J. *J. Phys. Condens. Matter* **2014,** 26, (6), 064204.

48. Balasubramanian, B.; Mukherjee, P.; Skomski, R.; Manchanda, P.; Das, B.; Sellmyer, D. J. *Sci. Rep* **2014,** 4, 6265.

49. Das, B.; Balamurugan, B.; Kumar, P.; Skomski, R.; Shah, V. R.; Shield, J. E.; Kashyap, A.; Sellmyer, D. J. *IEEE Trans. Magn.* **2013,** 49, (7), 3330-3333.

50. McGuire, M. A.; Rios, O.; Ghimire, N. J.; Koehler, M. *Appl. Phys. Lett.* **2012,** 101, (20), 202401.

51. Zhang, W. Y.; Li, X. Z.; Valloppilly, S.; Skomski, R.; Shield, J. E.; Sellmyer, D. J. *J. Phys. D-Appl. Phys.* **2013,** 46, (13), 135004.

52. Balamurugan, B.; Das, B.; Zhang, W. Y.; Skomski, R.; Sellmyer, D. J. *Journal of Physics: Condensed Matter* **2014,** 26, (6), 064204.

53. Zhang, W. Y.; Li, X. Z.; Valloppilly, S.; Skomski, R.; Shield, J. E.; Sellmyer, D. J. *Journal of Physics D: Applied Physics* **2013,** 46, (13), 135004.

54. Balamurugan, B.; Bhaskar, D.; Ralph, S.; Y., Z. W.; J., S. D. *Adv. Mater.* **2013,** 25, (42), 6090-6093.

55. Cedeno-Mattei, Y.; Perales-Pérez, O.; Uwakweh, O.; Xin, Y. *J. Appl. Phys.* **2010,** 107, (9), 09A741.

56. Cedeño-Mattei, Y.; Perales-Pérez, O.; Uwakweh, O. *Mater. Chem. Phys.* **2012,** 132, (2-3), 999-1006.

57. Fischer, R.; Leineweber, T.; Kronmüller, H. *Phys. Rev. B* **1998,** 57, (17), 10723-10732.

58. Mishima, T. *Stahl und Eisen* **1931,** 53, 79.

59. Luborsky, F.; Mendelsohn, L.; Paine, T. *J. Appl. Phys.* **1957,** 28, (3), 344-351.

60. Heidenreich, R.; Nesbitt, E. *J. Appl. Phys.* **1952,** 23, (3), 352-365.

61. Sucksmith, W.; Tyndall, A. M. *P. ROY. SOC. A-MATH. PHY.* **1939,** 171, (947), 525-540.

62. Zhou, L.; Miller, M. K.; Lu, P.; Ke, L.; Skomski, R.; Dillon, H.; Xing, Q.; Palasyuk, A.; McCartney, M. R.; Smith, D. J.; Constantinides, S.; McCallum, R. W.; Anderson, I. E.; Antropov, V.; Kramer, M. J. *Acta Materialia* **2014,** 74, 224-233.

63. Zhou, L.; Tang, W.; Ke, L.; Guo, W.; Poplawsky, J. D.; Anderson, I. E.; Kramer, M. J. *Acta Materialia* **2017,** 133, 73-80.

64. Mishima, T. *Ohm* **1932,** 19, 353.

65. Ke, L.; Skomski, R.; Hoffmann, T. D.; Zhou, L.; Tang, W.; Johnson, D. D.; Kramer, M. J.; Anderson, I. E.; Wang, C.-Z. *Appl. Phys. Lett.* **2017,** 111, (2), 022403.

66. Skomski, R.; Liu, Y.; Shield, J. E.; Hadjipanayis, G. C.; Sellmyer, D. J. *J. Appl. Phys.* **2010,** 107, (9), 09A739.

67. Gandha, K.; Elkins, K.; Poudyal, N.; Liu, X.; Liu, J. P. *Sci. Rep.* **2014,** 4.

68. Pousthomis, M.; Anagnostopoulou, E.; Panagiotopoulos, I.; Boubekri, R.; Fang, W.; Ott, F.; Atmane, K. A.; Piquemal, J.-Y.; Lacroix, L.-M.; Viau, G. *Nano Res.* **2015,** 8, (7), 2231-2241.

69. Ener, S.; Anagnostopoulou, E.; Dirba, I.; Lacroix, L.-M.; Ott, F.; Blon, T.; Piquemal, J.-Y.; Skokov, K. P.; Gutfleisch, O.; Viau, G. *Acta Mater.* **2018,** 145, 290-297.

70. Anagnostopoulou, E.; Grindi, B.; Lacroix, L.-M.; Ott, F.; Panagiotopoulos, I.; Viau, G. *Nanoscale* **2016,** 8, (7), 4020-4029.

71. Soumare, Y.; Garcia, C.; Maurer, T.; Chaboussant, G.; Ott, F.; Fiévet, F.; Piquemal, J. Y.; Viau, G. *Adv. Funct. Mater.* **2009,** 19, (12), 1971-1977.

72. Hartmann, U. *Phys. Rev. B* **1987,** 36, (4), 2331-2332.

73. Vila, L.; Vincent, P.; Dauginet-De Pra, L.; Pirio, G.; Minoux, E.; Gangloff, L.; Demoustier-Champagne, S.; Sarazin, N.; Ferain, E.; Legras, R. *Nano Lett.* **2004,** 4, (3), 521-524.

74. Han, X.; Liu, Q.; Wang, J.; Li, S.; Ren, Y.; Liu, R.; Li, F. *J. Phys. D: Appl. Phys.* **2009,** 42, (9), 095005.

75. Pan, H.; Liu, B.; Yi, J.; Poh, C.; Lim, S.; Ding, J.; Feng, Y.; Huan, C.; Lin, J. *J. Phys. Chem. B* **2005,** 109, (8), 3094-3098.

76. Qin, D.; Lu, M.; Li, H. *Chem. Phys. Lett.* **2001,** 350, (1-2), 51-56.

77. Atmane, K. A.; Michel, C.; Piquemal, J.-Y.; Sautet, P.; Beaunier, P.; Giraud, M.; Sicard, M.; Nowak, S.; Losno, R.; Viau, G. *Nanoscale* **2014,** 6, (5), 2682-2692.

78. Gandha, K.; Mohapatra, J.; Liu, J. P. *J. Magn. Magn. Mater.* **2017,** 438, 41-45.

79. Poudyal, N.; Rong, C.-b.; Liu, J. P. *J. Appl. Phys.* **2011,** 109, (7), 07B526.

80. Barbillon, G.; Bijeon, J.-L.; Plain, J.; De La Chapelle, M. L.; Adam, P.-M.; Royer, P. *Surf. Sci.* **2007,** 601, (21), 5057-5061.

81. Gandha, K.; Elkins, K.; Poudyal, N.; Liu, X.; Liu, J. P. *Sci. Rep.* **2014,** 4, 5345.

82. Stoica, T.; Meijers, R. J.; Calarco, R.; Richter, T.; Sutter, E.; Lüth, H. *Nano Lett.* **2006,** 6, (7), 1541-1547.

83. Coughlan, C.; Ibanez, M.; Dobrozhan, O.; Singh, A.; Cabot, A.; Ryan, K. M. *Chem. Rev.* **2017,** 117, (9), 5865-6109.

84. Skrdla, P. J. *J. Phys. Chem. C* **2012,** 116, (1), 214-225.

85. Barmparis, G. D.; Lodziana, Z.; Lopez, N.; Remediakis, I. N. *Beilstein journal of nanotechnology* **2015,** 6, (1), 361-368.

86. Carter, C. B.; Norton, M. G., *Ceramic materials: science and engineering*. Springer: 2007; Vol. 716.

87. Yuan, P.; Li, D.; Wu, L.; Shi, L. *Ceramics International* **2020,** Ceram. Int., (1), 1243-1247.

88. Zhao, Z.; Zhang, L.; Dai, H.; Du, Y.; Meng, X.; Zhang, R.; Liu, Y.; Deng, J. *Microporous Mesoporous Mater.* **2011,** 138, (1-3), 191-199.

89. Abate, Y.; Schwartzberg, A.; Strasser, D.; Leone, S. R. *Chem. Phys. Lett.* **2009,** 474, (1-3), 146-152.

90. Puntes, V. F.; Zanchet, D.; Erdonmez, C. K.; Alivisatos, A. P. *J. Am. Chem. Soc.* **2002,** 124, (43), 12874-12880.

91. Suryanarayana, C.; Norton, M. G., *X-Ray Diffraction: A Practical Approach*. Springer US: 2013.

92. Cumming, G.; Fidler, F.; Vaux, D. L. *J. Cell Biol.* **2007,** 177, (1), 7-11.

93. Dinega, D. P.; Bawendi, M. *Angew. Chem. Int. Ed.* **1999,** 38, (12), 1788-1791.

94. Sun, S.; Murray, C. *J. Appl. Phys.* **1999,** 85, (8), 4325-4330.

95. Nie, X.; Jiang, J.; Meletis, E.; Tung, L.; Spinu, L. *J. Appl. Phys.* **2003,** 93, (8), 4750-4755.

96. McHenry, M.; Laughlin, D. *Acta Mater.* **2000,** 48, (1), 223-238.

97. Frey, N.; Sun, S., Inorganic Nanoparticles: Synthesis, Applications, and Perspectives. CRC Press-Taylor and Francis Group, LLC: 2010.

98. Meziane, L.; Salzemann, C.; Aubert, C.; Gérard, H.; Petit, C.; Petit, M. *Nanoscale* **2016,** 8, (44), 18640-18645.

99. Kim, C. W.; Cha, H. G.; Kim, Y. H.; Jadhav, A. P.; Ji, E. S.; Kang, D. I.; Kang, Y. S. *J. Phys. Chem. C* **2009,** 113, (13), 5081-5086.

100. Meiklejohn, W. H.; Bean, C. P. *Phys. Rev.* **1956,** 102, (5), 1413-1414.

101. Skumryev, V.; Stoyanov, S.; Zhang, Y.; Hadjipanayis, G.; Givord, D.; Nogués, J. *nature* **2003,** 423, (6942), 850-853.

102. Peng, D. L.; Sumiyama, K.; Hihara, T.; Yamamuro, S.; Konno, T. J. *Phys. Rev. B* **2000,** 61, (4), 3103-3109.

103. Nogués, J.; Schuller, I. K. *J. Magn. Magn. Mater.* **1999,** 192, (2), 203-232.

104. Kiwi, M. *J. Magn. Magn. Mater.* **2001,** 234, (3), 584-595.

105. Wu, R.; Yun, C.; Ding, S.; Wen, X.; Liu, S.; Wang, C.; Han, J.; Du, H.; Yang, J. *J. Appl. Phys.* **2016,** 120, (5), 053902.

106. Hoffmann, A. *Phys. Rev. Lett.* **2004,** 93, (9), 097203.

107. Dor, O. B.; Yochelis, S.; Mathew, S. P.; Naaman, R.; Paltiel, Y. *Nat. Commun.* **2013,** 4, (1), 1-6.

108. De Toro, J.; de la Torre, M. L.; Riveiro, J.; Puche, R. S.; Gomez-Herrero, A.; Otero-Diaz, L. *Phys. Rev. B* **1999,** 60, (18), 12918.

109. Tiwari, S.; Rajeev, K. *Phys. Rev. B* **2005,** 72, (10), 104433.

110. Panagiotopoulos, I.; Fang, W.; Ott, F.; Boué, F.; Aït-Atmane, K.; Piquemal, J.-Y.; Viau, G. *J. Appl. Phys.* **2013,** 114, (14), 143902.

111. Kim, S.-i.; Yoon, H.; Lee, H.; Lee, S.; Jo, Y.; Lee, S.; Choo, J.; Kim, B. *J. Mater. Chem. C* **2015,** 3, (1), 100-106.

112. Liakakos, N.; Blon, T.; Achkar, C.; Vilar, V.; Cormary, B.; Tan, R. P.; Benamara, O.; Chaboussant, G.; Ott, F.; Warot-Fonrose, B. *Nano Lett.* **2014,** 14, (6), 3481-3486.

113. Vivas, L.; Yanes, R.; Chubykalo-Fesenko, O.; Vazquez, M. *Appl. Phys. Lett.* **2011,** 98, (23), 232507.

114. Maaz, K.; Karim, S.; Usman, M.; Mumtaz, A.; Liu, J.; Duan, J.; Maqbool, M. *Nanoscale Res. Lett.* **2010,** 5, (7), 1111-1117.

115. Sánchez-Barriga, J.; Lucas, M.; Radu, F.; Martin, E.; Multigner, M.; Marin, P.; Hernando, A.; Rivero, G. *Phys. Rev. B* **2009,** 80, (18), 184424.

116. Darques, M.; Encinas, A.; Vila, L.; Piraux, L. *J. Phys.: Condens. Matter* **2004,** 16, (22), S2279.

117. Feygenson, M.; Yiu, Y.; Kou, A.; Kim, K.-S.; Aronson, M. C. *Phys. Rev. B* **2010,** 81, (19), 195445.

118. Chandra, S.; Khurshid, H.; Phan, M.-H.; Srikanth, H. *Appl. Phys. Lett.* **2012,** 101, (23), 232405.

119. Wu, R.; Xue, M.; Maity, T.; Peng, Y.; Giri, S. K.; Tian, G.; MacManus-Driscoll, J. L.; Yang, J. *Phys. Rev. B* **2020,** 101, (1), 014425.

120. Maat, S.; Takano, K.; Parkin, S.; Fullerton, E. E. *Phys. Rev. Lett.* **2001,** 87, (8), 087202.

121. Maurer, T.; Zighem, F.; Ott, F.; Chaboussant, G.; André, G.; Soumare, Y.; Piquemal, J.-Y.; Viau, G.; Gatel, C. *Physical Review B* **2009,** 80, (6), 064427.

122. Wen, X.; Gandha, K.; Liu, J.; Yang, W.; Wang, C.; Liu, S.; Yang, J. *IEEE Trans. Magn.* **2018,** 54, (11), 1-6.

123. Gandha, K.; Chaudhary, R. P.; Mohapatra, J.; Koymen, A. R.; Liu, J. P. *Phys. Lett. A* **2017,** 381, (25-26), 2092-2096.

124. Cormary, B.; Li, T.; Liakakos, N.; Peres, L.; Fazzini, P.-F.; Blon, T.; Respaud, M.; Kropf, A. J.; Chaudret, B.; Miller, J. T. *J. Am. Chem. Soc.* **2016,** 138, (27), 8422-8431.

125. Xu, H.; Wu, Q.; Yue, M.; Li, C.; Li, H.; Palaka, S. *AIP Adv.* **2018,** 8, (5), 056422.

126. Li, C.; Wu, Q.; Yue, M.; Xu, H.; Palaka, S.; Elkins, K.; Ping Liu, J. *AIP Adv.* **2017,** 7, (5), 056229.

127. Gandha, K.; Chaudhary, R. P.; Mohapatra, J.; Koymen, A. R.; Liu, J. P. *Phys. Lett. A* **2017,** 381, (25), 2092-2096.

128. Che, R.; Takeguchi, M.; Shimojo, M.; Zhang, W.; Furuya, K. *Appl. Phys. Lett.* **2005,** 87, (22), 223109.

129. Lavín, R.; Denardin, J. C.; Escrig, J.; Altbir, D.; Cortés, A.; Gómez, H. *J. Appl. Phys.* **2009,** 106, (10), 103903.

130. Levy, J.-C. S., *Magnetic structures of 2d and 3d nanoparticles: properties and applications*. CRC Press: 2018.

131. Aharoni, A. *Phys. Status Solidi B* **1966,** 16, (1), 3-42.

132. Ishii, Y.; Sato, M. *J. Appl. Phys.* **1989,** 65, (8), 3146-3150.

133. Stoner, E. C.; Wohlfarth, E. *Philos. Trans. R. Soc. London, Ser. A* **1948,** 240, (826), 599-642.

134. Suszka, A.; Idigoras, O.; Nikulina, E.; Chuvilin, A.; Berger, A. *Phys. Rev. Lett.* **2012,** 109, (17), 177205.

135. Takano, K.; Kodama, R.; Berkowitz, A.; Cao, W.; Thomas, G. *Phys. Rev. Lett.* **1997,** 79, (6), 1130.

136. Parkin, S. S.; Hayashi, M.; Thomas, L. *Sci.* **2008,** 320, (5873), 190-194.

137. Gapin, A.; Ye, X.; Aubuchon, J.; Chen, L.; Tang, Y.; Jin, S. *J. Appl. Phys.* **2006,** 99, (8), 08G902.

138. McGary, P. D.; Tan, L.; Zou, J.; Stadler, B. J.; Downey, P. R.; Flatau, A. B. *J. Appl. Phys.* **2006,** 99, (8), 08B310.

139. Ye, B.; Li, F.; Cimpoesu, D.; Wiley, J.; Jung, J.-S.; Stancu, A.; Spinu, L. *J. Magn. Magn. Mater.* **2007,** 316, (2), e56-e58.

140. Qin, J.; Nogués, J.; Mikhaylova, M.; Roig, A.; Munoz, J. S.; Muhammed, M. *Chem. Mater.* **2005,** 17, (7), 1829-1834.

141. Poudyal, N.; Chaubey, G. S.; Nandwana, V.; Rong, C.-b.; Yano, K.; Liu, J. P. *Nanotechnology* **2008,** 19, (35), 355601.

142. Gandha, K.; Tsai, P.; Chaubey, G.; Poudyal, N.; Elkins, K.; Cui, J.; Liu, J. P. *Nanotechnology* **2015,** 26, (7), 075601.

143. Xing, M.; Mohapatra, J.; Elkins, J.; Beatty, J.; Liu, J. P. *AIP Adv.* **2019,** 9, (3), 035323.

144. Maurer, T.; Zighem, F.; Fang, W.; Ott, F.; Chaboussant, G.; Soumare, Y.; Atmane, K. A.; Piquemal, J.-Y.; Viau, G. *J. Appl. Phys.* **2011,** 110, (12), 123924.

145. Chang, C. R.; Shyu, J. P. *J. Appl. Phys.* **1993,** 73, (10), 6659-6661.

146. Morrish, A. H.; Yu, S. P. *J. Appl. Phys.* **1955,** 26, (8), 1049-1055.

147. Mohapatra, J.; Xing, M.; Elkins, J.; Liu, J. P. *J. Alloys Compd.* **2020,** 824, 153874.

148. Cao, D.-B.; Zhang, F.-Q.; Li, Y.-W.; Wang, J.; Jiao, H. *J. Phys. Chem. B* **2005,** 109, (21), 10922-10935.

149. Chang, Q.; Zhang, C.; Liu, C.; Wei, Y.; Cheruvathur, A. V.; Dugulan, A. I.; Niemantsverdriet, J.; Liu, X.; He, Y.; Qing, M. *ACS Catal.* **2018,** 8, (4), 3304-3316.

150. Yu, J.; Chen, F.; Gao, W.; Ju, Y.; Chu, X.; Che, S.; Sheng, F.; Hou, Y. *Nanoscale Horiz.* **2017,** 2, (2), 81-88.

151. Meffre, A.; Mehdaoui, B.; Kelsen, V.; Fazzini, P. F.; Carrey, J.; Lachaize, S.; Respaud, M.; Chaudret, B. *Nano Lett.* **2012,** 12, (9), 4722-4728.

152. Xiao, M.; Zhu, J.; Feng, L.; Liu, C.; Xing, W. *Adv. Mater.* **2015,** 27, (15), 2521-2527.

153. Nikitenko, S. I.; Koltypin, Y.; Palchik, O.; Felner, I.; Xu, X. N.; Gedanken, A. *Angew. Chem. Int. Ed.* **2001,** 40, (23), 4447-4449.

154. Schinteie, G.; Kuncser, V.; Palade, P.; Dumitrache, F.; Alexandrescu, R.; Morjan, I.; Filoti, G. *J. Alloys Compd.* **2013,** 564, 27-34.

155. Baskakov, A. O.; Lyubutin, I. S.; Starchikov, S. S.; Davydov, V. A.; Kulikova, L. F.; Egorova, T. B.; Agafonov, V. N. *Inorg. Chem.* **2018,** 57, (23), 14895-14903.

156. Amsarajan, S.; Jagirdar, B. R. *Eur. J. Inorg. Chem.* **2019,** 2019, (10), 1374-1383.

157. Ge, W.; Gao, W.; Zhu, J.; Li, Y. *J. Alloys Compd.* **2019,** 781, 1069-1073.

158. Jin, Y.; Deng, J.; Yu, J.; Yang, C.; Tong, M.; Hou, Y. *J. Mater. Chem. B* **2015,** 3, (19), 3993-4000.

159. Li, S.; Yang, J.; Song, C.; Zhu, Q.; Xiao, D.; Ma, D. *Adv. Mater.* **2019,** 31, (50), 1901796.

160. An, B.; Cheng, K.; Wang, C.; Wang, Y.; Lin, W. *ACS Catal.* **2016,** 6, (6), 3610-3618.

161. Yu, J.; Zhao, F.; Gao, W.; Yang, X.; Ju, Y.; Zhao, L.; Guo, W.; Xie, J.; Liang, X.-j.; Tao, X. *ACS nano* **2019,** 13, (9), 10002-10014.

162. Lou, Z.; Yuan, C.; Zhang, Y.; Li, Y.; Cai, J.; Yang, L.; Wang, W.; Han, H.; Zou, J. *J. Alloys Compd.* **2019,** 775, 800-809.

163. Guo, C.; He, J.; Wu, X.; Huang, Q.; Wang, Q.; Zhao, X.; Wang, Q. *ACS Appl. Mater. Interfaces* **2018,** 10, (42), 35994-36001.

164. Ju, J.; Kim, M.; Jang, S.; Kim, Y.; Choi, Y.; Baeck, S.-H.; Shim, S. E. *Electrochim. Acta* **2017,** 252, 215-225.

165. Yao, L.; Yang, J.; Zhang, P.; Deng, L. *Bioresour. Technol.* **2018,** 256, 208-215.

166. Yang, Y.; Fan, X.; Casillas, G.; Peng, Z.; Ruan, G.; Wang, G.; Yacaman, M. J.; Tour, J. M. *ACS nano* **2014,** 8, (4), 3939-3946.

167. Zhang, J.; Wang, K.; Xu, Q.; Zhou, Y.; Cheng, F.; Guo, S. *Acs Nano* **2015,** 9, (3), 3369-3376.

168. Bohra, M.; Agarwal, N.; Singh, V. *J. Nanomater.* **2019,** 2019.

169. Leszczyński, B.; Hadjipanayis, G. C.; El-Gendy, A. A.; Załęski, K.; Śniadecki, Z.; Musiał, A.; Jarek, M.; Jurga, S.; Skumiel, A. *J. Magn. Magn. Mater.* **2016,** 416, 269-274.

170. Khurshid, H.; Li, W.; Chandra, S.; Phan, M.-H.; Hadjipanayis, G. C.; Mukherjee, P.; Srikanth, H. *Nanoscale* **2013,** 5, (17), 7942-7952.

171. Phan, M.-H.; Alonso, J.; Khurshid, H.; Lampen-Kelley, P.; Chandra, S.; Stojak Repa, K.; Nemati, Z.; Das, R.; Iglesias, Ó.; Srikanth, H. *Nanomaterials* **2016,** 6, (11), 221.

172. Lottini, E.; López-Ortega, A.; Bertoni, G.; Turner, S.; Meledina, M.; Van Tendeloo, G.; de Julián Fernández, C.; Sangregorio, C. *Chem. Mater.* **2016,** 28, (12), 4214-4222.

173. Fabris, F.; Lima, E.; De Biasi, E.; Troiani, H. E.; Mansilla, M. V.; Torres, T. E.; Pacheco, R. F.; Ibarra, M. R.; Goya, G. F.; Zysler, R. D. *Nanoscale* **2019,** 11, (7), 3164-3172.

174. Yang, C.; Zhao, H.; Hou, Y.; Ma, D. *J. Am. Chem. Soc.* **2012,** 134, (38), 15814-15821.

175. Espinosa, A.; Di Corato, R.; Kolosnjaj-Tabi, J.; Flaud, P.; Pellegrino, T.; Wilhelm, C. *ACS nano* **2016,** 10, (2), 2436-2446.

176. Yang, C.; Zhao, H.; Hou, Y.; Ma, D. *J. Am. Chem. Soc.* **2012,** 134, (38), 15814-15821.

177. Lu, Y.; Zhang, R.; Cao, B.; Ge, B.; Tao, F. F.; Shan, J.; Nguyen, L.; Bao, Z.; Wu, T.; Pote, J. W. *ACS Catal.* **2017,** 7, (8), 5500-5512.

178. Herranz, T.; Rojas, S.; Pérez-Alonso, F. J.; Ojeda, M.; Terreros, P.; Fierro, J. L. G. *J. Catal.* **2006,** 243, (1), 199-211.

179. Mohapatra, J.; Zeng, F.; Elkins, K.; Xing, M.; Ghimire, M.; Yoon, S.; Mishra, S. R.; Liu, J. P. *Phys. Chem. Chem. Phys.* **2018,** 20, (18), 12879-12887.

180. Mohapatra, J.; Xing, M.; Beatty, J.; Elkins, J.; Seda, T.; Mishra, S. R.; Liu, J. P. *Nanotechnol.* **2020,** 31, (27), 275706.

181. Jamet, M.; Wernsdorfer, W.; Thirion, C.; Dupuis, V.; Mélinon, P.; Pérez, A.; Mailly, D. *Phys. Rev. B* **2004,** 69, (2), 024401.

182. Zheng, W.; Zheng, D.; Wang, Y.; Jin, C.; Bai, H. *Appl. Phys. Lett.* **2018,** 113, (14), 142403.

183. Cuñado, J. L. F.; Camarero, J.; Pedrosa, F. J.; Nemes, N. M.; Sanz, M.; Oujja, M.; Rebollar, E.; Marco, J. F.; De La Figuera, J.; Monti, M. *Nanoscale* **2019,** 11, (42), 19870-19876.

184. De La Venta, J.; Erekhinsky, M.; Wang, S.; West, K.; Morales, R.; Schuller, I. K. *Phys. Rev. B* **2012,** 85, (13), 134447.

185. Nayek, C.; Manna, K.; Bhattacharjee, G.; Murugavel, P.; Obaidat, I. *Magnetochemistry* **2017,** 3, (2), 19.

186. Metin, O. n.; Mazumder, V.; Ozkar, S.; Sun, S. *J. Am. Chem. Soc.* **2010,** 132, (5), 1468-1469.

187. Fujieda, S.; Kuboniwa, T.; Shinoda, K.; Suzuki, S.; Echigoya, J. *AIP Adv.* **2016,** 6, (5), 056116.

188. Nunes, W.; De Biasi, E.; Meneses, C.; Knobel, M.; Winnischofer, H.; Rocha, T.; Zanchet, D. *Appl. Phys. Lett.* **2008,** 92, (18), 183113.

189. Schaefer, Z. L.; Weeber, K. M.; Misra, R.; Schiffer, P.; Schaak, R. E. *Chem. Mater.* **2011,** 23, (9), 2475-2480.

190. Yue, L.; Sabiryanov, R.; Kirkpatrick, E. M.; Leslie-Pelecky, D. L. *Phys. Rev. B: Condens. Matter* **2000,** 62, (13), 8969-8975.

191. Chen, C.; He, L.; Leng, Y.; Li, X. *J. Appl. Phys.* **2009,** 105, (12), 123923.

192. He, L.; Zheng, W.; Zhou, W.; Du, H.; Chen, C.; Guo, L. *J. Phys.: Condens. Matter* **2007,** 19, (3), 036216.

193. Zhou, W.; Zheng, K.; He, L.; Wang, R.; Guo, L.; Chen, C.; Han, X.; Zhang, Z. *Nano Lett.* **2008,** 8, (4), 1147-1152.

194. Khurshid, H.; Lampen-Kelley, P.; Iglesias, Ò.; Alonso, J.; Phan, M.-H.; Sun, C.-J.; Saboungi, M.-L.; Srikanth, H. *Sci. Rep.* **2015,** 5, 15054.

195. Mohapatra, J.; Mitra, A.; Bahadur, D.; Aslam, M. *CrystEngComm* **2013,** 15, (3), 524-532.

196. Uhlig, S.; Struis, R.; Schmid-Engel, H.; Bock, J.; Probst, A.-C.; Freitag-Weber, O.; Zizak, I.; Chernikov, R.; Schultes, G. *Diamond Relat. Mater.* **2013,** 34, 25-35.

197. Mohapatra, J.; Mitra, A.; Bahadur, D.; Aslam, M. *J. Alloys Compd.* **2015,** 628, 416-423.

198. De Almeida, J.; Thouless, D. J. *J. Phys. A: Math. Gen.* **1978,** 11, (5), 983.

199. Martinez, B.; Obradors, X.; Balcells, L.; Rouanet, A.; Monty, C. *Phys. Rev. Lett.* **1998,** 80, (1), 181.

200. Hirosawa, S.; Nishino, M.; Miyashita, S. *Adv. Nat. Sci.: Nanosci. Nanotechnol.* **2017,** 8, (1), 013002.